High-resolution $^{87}Sr/^{86}Sr$ record from the Triassic-Jurassic boundary section at Csővár and its implications

MSc THESIS

GEOLOGY MSc
GEOLOGY-PALEONTOLOGY SPECIALIZATION

By Bernát Heszler
Thesis supervisor: Dr. József Pálfy

Eötvös Loránd University
Institute of Geography and Earth Sciences
Department of Geology

2023

Table of contents

1 Introduction

The Triassic-Jurassic boundary (TJB; 201.3 Ma (Hillebrandt et al. 2013)) is associated with one of the most severe crises in the evolution of life, known as the end-Triassic extinction (ETE), which is regarded as one of the „big five" extinction events (Sepkoski et al. 1982). The event has been tied to the magmatism of the Central Atlantic Magmatic Province (CAMP) flood basalts as the primary cause of the extinction. Despite advancements in understanding the effects of the CAMP's emplacement and associated perturbations, the intensity and timing of continental weathering in response to elevated atmospheric CO_2 levels with the eruption of CAMP remain unclear. The links between volcanic activity, carbon isotope excursions, and continental weathering remain largely inferential and require further validation. Strontium isotope stratigraphy is a well-established and powerful tool for studying the TJB, as it provides insight into the timing and intensity of continental weathering, which can help to elucidate the causes of the extinction event. Until now, there has not been a detailed $^{87}Sr/^{86}Sr$ study that stretched through the TJB into the earliest Hettangian. Here, new bulk high-resolution $^{87}Sr/^{86}Sr$ data from the Csővár section in Hungary is presented, which is an important continuous marine section spanning 3 million years.

McArthur (2008) argued: "A better, and complete rather than patched, profile of $^{87}Sr/^{86}Sr$ across the Tr–J boundary is needed, from somewhere other than Dorset, UK, or the Kössen Basin, Austria, before robust inferences are drawn from the profile of $^{87}Sr/^{86}Sr$ through this interval." With this thesis, I attempt to provide the most detailed $^{87}Sr/^{86}Sr$ dataset through the boundary interval, with the motivation of drawing conclusions regarding the global environment- and climate changes and presenting additional empirical constraints to make the reference curve more reliable for stratigraphic correlation purposes.

1.1 The end-Triassic extinction event

The end-Triassic extinction (ETE; 201.56 Ma (Blackburn et al. 2013)) is a major crisis in biodiversity. The ETE is one of the most significant mass extinction events in terms of diversity loss in the history of the Phanerozoic era. This time interval is also characterized by a severe perturbation of the ocean-atmosphere and biological systems, such as global warming, ocean acidification, changes in sea level, and ecosystem collapse. The extinction is marked by more than 50% loss of genera in both marine and terrestrial environments (Sepkoski 1996), It had an impact on various marine groups, such as bivalves, brachiopods, ostracods, calcareous algae,

radiolarians, tetrapods, and had a significant effect on palynological groups (Kuerschner et al. 2007, Wignall & Atkinson 2020). These changes also coincided with significant alterations in palynological assemblages and led to the final extinction of conodonts. It is characterized by the disappearance of Triassic ammonites and the notable damage to scleractinian corals. The mass extinction event is believed to have coincided with one of the largest reef crises in Earth's history (Kiessling & Simpson 2011). The continental record of ETE is marked by an important change in sporomorphs and early Mesozoic vertebrates, as well as a replacement of over 95% of megaflora (Benton 1995, Hallam 2002). The event marks a transition in the palynological assemblages that manifests in a fern pollen spike at the boundary (Van de Schootbrugge et al. 2009). The spike is accompanied by the extinction of palynoflora groups and shows a close correlation with the extinctions observed in terrestrial vertebrates, occurring nearly simultaneously (Fowell & Olsen 1993). The significant faunal changes of terrestrial vertebrates are also prominent. Global analyses suggest that the Triassic-Jurassic boundary was a turning point in the evolution of primitive reptiles. The dominance on land was taken over by dinosaurs for the rest of the Mesozoic (Olsen et al. 2002). The duration of the extinction event as well as whether it was gradual or catastrophic remain a topic of debate. Some suggest a potential meteorite impact based on an iridium anomaly, although other corroborating evidence, such as impact structures and shocked quartz grains is missing (Tanner et al. 2004). An increasing consensus points towards the magmatism of the Central Atlantic magmatic province (CAMP) flood basalt volcanism as the primary cause of the extinction, while CAMP also initiated the fragmentation of the Pangea supercontinent and the opening of the Atlantic (Pálfy et al. 2000) (Fig. 1). The CAMP is one of the largest known Large Igneous Provinces (LIP) on Earth, presently it stretches across four continents on both hemispheres (Marzoli et al. 1999). The volume of erupted basalts reaches 3×10^6 km^3 within 500–1 500 kyr, while releasing more than 8 000 Gt of CO_2 (Marzoli et al. 1999, Beerling & Berner 2002). Degassing likely triggered global warming that in turn resulted in shallow marine anoxia, and caused perturbations in the carbon cycle, as evidenced by anomalies in the stable isotope composition of carbonates and organic matter.

All significant turnovers in Earth's history are associated with excursions in carbon isotope records that are thought to have been caused by disturbances in the global carbon cycle. The CAMP eruptive phases are linked to significant $\delta^{13}C$ perturbations (Pálfy et al. 2001, Ward et al. 2001, Hesselbo et al. 2002). It has been suggested that CO_2 and sulfur gas emissions from the Central Atlantic magmatic province, resulting from volcanic and contact metamorphic

activity, were responsible for the climate change that caused the end-Triassic extinction (Heimdal et al. 2020). However, carbon cycle models for the boundary interval suggest that the release of mantle-derived carbon from CAMP cannot alone account for the excessive carbon perturbations associated with the ETE. Alternative suggestions include marine methane clathrate dissociation induced by CAMP volcanism or volcanic degassing of carbon with an anomalous $\delta^{13}C$ value of −20‰ (Paris et al. 2012).

Although our understanding of the timing, cause, and effects of the emplacement of the Central Atlantic magmatic province and its associated perturbations has increased, many questions remain unanswered. In particular, the intensity and timing of continental weathering in response to the CAMP, and elevated atmospheric CO_2 levels, remains unclear, as well as the potential feedbacks between weathering and climate. Additionally, our comprehension of the marine geologic record of the Triassic-Jurassic boundary is limited by the lack of continuous sedimentary successions across this boundary. The goal of this thesis is to shed light on these questions by the analysis of $^{87}Sr/^{86}Sr$ ratio in bulk carbonates from the continuous Csővár section, and therefore improve our knowledge of the complex interplay between magmatic activity, weathering, and climate during the Triassic-Jurassic boundary.

1.2 Timing of events

The base of the Jurassic System and Hettangian Stage has been defined by the first occurrence of the ammonite *Psiloceras spelae tirolicum* (Hillebrandt et al. 2013). The Global Stratotype Section and Point (GSSP) for the Hettangian is located at Kuhjoch section in the western Tethys Eiberg Basin. At Kuhjoch, the Triassic–Jurassic boundary is fixed at 5.8 m stratigraphically above the end-Triassic marine extinction interval (~100 kyr) (Deenen et al. 2010, Hillebrandt et al. 2013). For understanding the end-Triassic mass extinction, the accurate timing of events is necessary. Here I summarize the events based on the carbon isotope stratigraphy of the TJB.

Initially, a negative carbon isotope excursion was associated with the end-Triassic extinction (Pálfy et al. 2001, Ward et al. 2001, Hesselbo et al. 2002), and its connection to the Central Atlantic magmatic province. Increased atmospheric pCO_2 is linked to all possible mechanisms that generate significant light carbon isotopic anomalies in exchangeable surface reservoirs (Kump & Arthur 1999). The timing of the CAMP activity and the global occurrence of the 5-6‰ negative carbon isotopic anomalies have been debated. However, in recent years, mounting evidence has established a clear temporal correlation between the CAMP, the end-Triassic

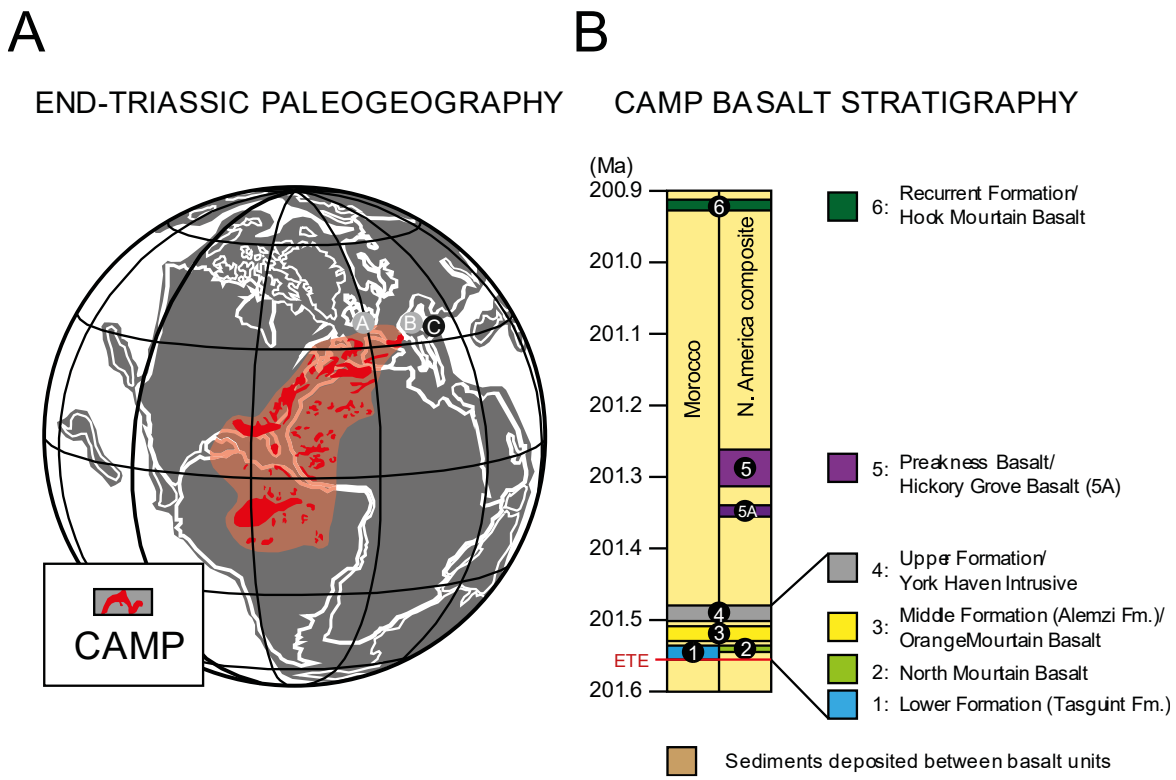

Fig. 1. (A) The paleogeographic distribution of the Central Atlantic Magmatic Province (CAMP) and the relevant and studied sections for the end-Triassic. A, St Audries Bay, United Kingdom; B, Northern Calcareous Alps, Austria; C, Csővár, Hungary. B) The composite stratigraphy of Moroccan and North American CAMP basalts based on their stratigraphic relationships and ages. Modified after Percival et al. (2017), ages and correlation from Deenen et al. (2010), Whiteside et al. (2010) and Blackburn et al. (2013).

extinction, and the negative carbon isotope excursions. This has led to the hypothesis that the CAMP's intense volcanic activity was the primary cause of the extinction. Ruhl et al. (2011) identified three phases of disturbances in global biogeochemical cycles related to the formation of the CAMP. The ETE is typically characterized by a sequence of three negative carbon isotope excursions (NCIEs), namely the “precursor” (P-NCIE), the “initial” (I-NCIE), and the “main” (M-NCIE) NCIEs (Ruhl & Kürschner 2011, Du et al. 2020).

The primary CAMP pulse coincides with significant turnovers in the palynological and vertebrate record in the continental realm. It also coincides with the final appearance of the last Triassic ammonoids *Choristoceras crickmayi* in North America and *Choristoceras marshi* in the Northern Calcareous Alps (Zaffani et al. 2018). This event is also marked by high levels of extinction in bivalves and a shift in foraminifera- and palynomorph assemblages, also marks the significant turnover in radiolarians. The initial negative CIE (I-NCIE) is associated with the primary pulse of CAMP volcanism, and it is recorded in both marine and continental records (Deenen et al. 2010).

The second pulse of CAMP volcanism, which is more extensive, can be linked to successive transitions in foraminifera and palynomorph assemblages, the final appearance of conodonts, marine anoxia, and a crisis in calcification in calcareous nannofossils (Deenen et al. 2010). The main CIE occurs approximately across the TJB into the Hettangian.

The complexity of the carbon cycle narrative at the end of the Triassic period is challenged by the presence of a precursor negative carbon isotope excursion (P-NCIE) that has been observed in some shallow marine sections in the Tethys Ocean, Mid- and Eastern Panthalassa (Ruhl & Kürschner 2011, Fujisaki et al. 2018, Larina et al. 2021). Although it is of a smaller magnitude (~1–3‰) and shorter duration compared to the I-NCIE, the P-NCIE suggests that the ocean-atmosphere carbon system was disturbed prior to the ETE (Korte et al. 2018). However, the source of the precursor $\delta^{13}C$-depleted carbon is still under debate.

Evidence for earlier lava flows and the sub-volcanic phase of intrusive rocks preceding the first eruptive basalts that were contemporaneous with the negative carbon isotope excursions provided support that the CAMP was a primary cause of the environmental and biotic changes leading to the extinction (Corso et al. 2014). This is explained by the intrusion of dike and sill systems into previous basin deposits that caused the thermal alteration of subsurface organic-rich layers, which could have led to the release of thermogenic methane (Heimdal et al. 2020).

In summary, the major initial negative C isotope excursion (up to -7‰) is followed by a ~3.5‰ positive excursion before the long-term main negative shift. A precursor negative CIE (~2-3‰) predates the uppermost Rhaetian initial negative CIE and the mass extinction event, which is explained by the intrusion of dike and sill systems into subsurface organic-rich layers that led to the release of light carbon. The $\delta^{13}C$ negative shifts in global carbon reservoirs are believed to have occurred due to the discharge of isotopically light carbon, such as CO_2 from volcanic degassing, thermal metamorphism of organic-rich sediments, and biogenic methane. Recently, a detailed discussion of some alternative correlation was also outlined (Lindström et al. 2017, Lindström et al. 2021).

1.3 Geochemical paleoproxy investigations of the ETE

Significant disruptions in the global carbon cycle, evidenced by carbon isotope ($\delta^{13}C$) excursions (CIEs) observed in organic carbon and carbonate records, have been attributed to volcanic activity associated with the emplacement of Large Igneous Provinces (LIPs). Carbon isotope stratigraphy is just one of the several possibilities of paleoproxy investigations that have

shed light on the causes and dynamics of global climate change that caused extinction events. Other investigations have also been important to better understand these processes.

The concentration of mercury (Hg) in sedimentary rocks has been utilized as an indicator of large-scale volcanic activity on a regional to global scale. It serves as a useful proxy for LIP volcanism, and it is based on the observation that during the activity of a LIP, a large amount of Hg is released into the atmosphere. The primary form of released Hg is elemental gas, which has an atmospheric residence time of 0.5-1 year, but can be transported through air to distances of over 10^4 kilometers from the source, because of high-velocity stratospheric winds (Grasby et al. 2019). The emitted Hg ends up in marine sediments by sequestration, which is believed to occur mainly through the adsorption of Hg onto organic matter that settles from the water column. Therefore, Hg peaks in samples show pulses of volcanic activity. LIPs are reflected as sharp, individual peaks in Hg concentration, whereas continuous eruptions lead to long-lasting elevated Hg concentration values (Percival et al. 2021). During the intrusive phase of a volcanic province, additional Hg is released as volatile, either directly degassing from the magma or due to the contact metamorphism of organic-rich sediments.

Mercury concentration studies of the ETE that have shown that the extinction event is linked to the emplacement of the CAMP (Thibodeau et al. 2016, Percival et al. 2017, Lindström et al. 2019, Kovács et al. 2020a, Ruhl et al. 2020, Yager et al. 2021, Kaiho et al. 2022, Shen et al. 2022a). The successful use of the Hg proxy improves our knowledge of the ETE and TJB transition, provided that Hg can be used as a marker for CAMP volcanic activity that can be linked directly to the marine extinction record across various stratigraphic sections. The ETE extinction interval is characterized by increased Hg concentrations and Hg/TOC ratios in both marine and terrestrial sections, which have been linked to volcanic origins. While Hg shows great potential as a tracer of LIP volcanism, there are still many important questions that need to be answered before it can be considered a definitive tool. It is unclear why some sedimentary records exhibit clear Hg enrichment signals while others do not. Further research is needed to assess the impact of different volcanic styles on the global Hg cycle, and to better understand how depositional processes can record perturbations in the global Hg cycle.

The isotope ratio of uranium in marine sediments gives us information about the redox state of the ancient seawater. It is expressed as $\delta^{238}U$ representing the ratio of ^{238}U and ^{235}U. Uranium exists in two primary oxidation states: U(VI), which is soluble in oxygenated water, and U(IV), which is insoluble. Consequently, the quantity of uranium present in the water column is determined by the amount of dissolved oxygen in the oceans. As the dissolved oxygen level in

seawater decreases, U(VI) is reduced to U(IV). Because of its insolubility, the reduced uranium precipitates out of the water column, resulting in a depletion of uranium in the water. The reduced U(IV) that precipitates from seawater is enriched in the heavier isotope ^{238}U, while the U(VI) that remains soluble in the water column contains relatively more of the lighter isotope ^{235}U. The residence time of uranium in modern seawater is significantly longer than its mixing time, as a result, the uranium isotopic composition is a global indicator of the degree of bottom-water anoxia (Andersen et al. 2014, Zhang et al. 2020).

The $\delta^{238}U$ isotope ratio of carbonates has been used in several mass extinction studies. The developement of marine anoxia is tied to several extinctions and is expressed as a negative $\delta^{238}U$ anomaly in the sedimentary record. For the ETE interval, two studies have reported a major $\delta^{238}U$ negative anomaly, indicating widespread marine anoxia during the mass extinction (Jost et al. 2017, Somlyay et al. 2023).

The isotopic composition of seawater sulfate during significant redox perturbations of the Earth's surface system can be reconstructed by studying carbonate-associated sulfate (CAS) in bulk marine carbonate and biogenic calcite. The variations in the fluxes and isotopic compositions of different sulfate sources and marine pyrite burial dynamically control the seawater sulfate $\delta^{34}S$ (Bottrell & Newton 2006). Therefore, the marine sulfur cycle is primarily controlled by the production and burial of pyrite, which is redox-sensitive and leads to a significant coupling in the sulfur isotopic composition between seawater sulfate and the sedimentary pyrite depositions. S isotope perturbations are common characteristics of major Phanerozoic deoxygenation events. Positive CAS $\delta^{34}S$ anomalies for the Permo-Triassic extinction have been reported, as well for the ETE, indicating increased oceanic anoxia and pyrite burial for these intervals (Newton et al. 2004, He et al. 2020).

1.4 A missing piece

While more and more paleontological, sedimentological, and geochemical evidence are complementing our knowledge on the ETE and its connection to the volcanism of CAMP, not all feedback mechanisms are yet fully resolved. A key aspect in understanding the global phenomena associated with the extinction event is the response of the weathering regime to the CO_2 outgassing from volcanism at the time. Enhanced continental weathering is a potential mechanism linking volcanic activity and marine environmental disturbances. Local weathering proxies have been widely used for the ETE, such as clay mineralogy, paleosols and Os isotope

systems (Cohen & Coe 2007, Van de Schootbrugge et al. 2020, Onoue et al. 2022, Shen et al. 2022a). These studies show an abrupt change in the weathering intensity in the response to emplacement of CAMP. However, highly resolved, and accurate constraints on the weathering regime are still lacking for this time interval. Here, I present the first detailed study of Sr isotopes across the TJB interval from a continuous section based on new bulk high resolution $^{87}Sr/^{86}Sr$ data from Csővár in Hungary.

2 Strontium Isotope Stratigraphy

2.1 Strontium as a paleoenvironmental proxy

Strontium has been a much-studied element in the field of geochemistry for a considerable period of time (Elderfield 1986). Strontium has four stable isotopes, their natural concentrations on Earth are as follows: ^{84}Sr 0.56%; ^{86}Sr 9.86%; ^{87}Sr 7.0% and ^{88}Sr 82.58% (De Laeter et al. 2003). Due to strontium's moderate incompatibility during mantle melting, it is enriched up to tenfold in the continental crust and sixfold in mid-ocean ridge basalts compared to the primitive mantle. Rubidium is even more enriched in the continental crust compared to the primitive mantle due to its highly incompatible behaviour during mantle melting, while it is less enriched in mid-ocean ridge basalts (Chen et al. 2022). Biogenically precipitated calcium carbonate is the main mechanism by which strontium is removed from the oceans. During this process, strontium partially replaces calcium in the crystal lattice of calcite or aragonite. Additionally, strontium is also removed from the oceans through inorganic precipitation that occurs in chemical sediments like evaporites, ferromanganese nodules, and crusts. The ^{87}Sr/^{86}Sr isotopic ratio in marine calcite reflects the composition of the ocean water at the time of calcite's precipitation. The strontium concentration in present-day marine carbonates varies between 200 and 10 000 ppm (Wierzbowski 2015). The strontium isotope composition of seawater has changed throughout the Earth's geological history due to varying inputs from its two key sources (Fig. 2). Low ^{87}Sr/^{86}Sr ratio (around 0.703) strontium from hydrothermal influx from oceanic ridges and hotspots is non-radiogenic, high ^{87}Sr/^{86}Sr ratio (around 0.7136) strontium from continental weathering input transported by rivers and groundwater is radiogenic (Pearce et al. 2015) (Fig. 3). Additionally, there's an intermediate ^{87}Sr/^{86}Sr ratio (around 0.709) flux from submarine dissolution and sediment re-crystallization (Palmer & Edmond 1989, Allègre et al. 2010). Therefore, the ^{87}Sr/^{86}Sr ratio in seawater at any given time is a reflection of the balance between the contributions of continental and mantle reservoirs to ocean chemistry and can provide insights into global tectonic activity, weathering rates, and biogeochemical cycling throughout Earth's history (Chen et al. 2022) (Fig. 3). In detail, the exact distribution of contributions from each source is still a topic of debate, as well as the issue of whether the sources and sinks are balanced in present-day oceans (Peucker-Ehrenbrink & Fiske 2019) (Fig.

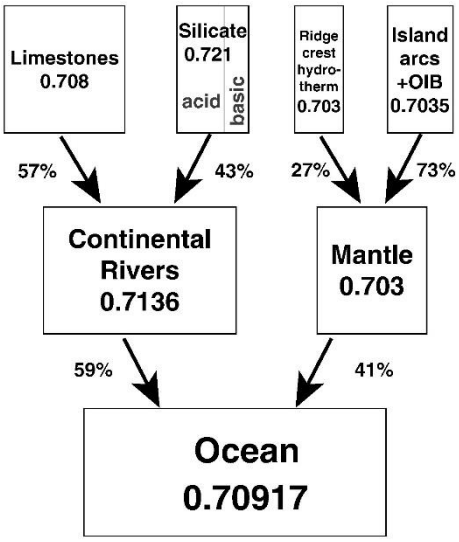

Fig. 2. The oceanic budget and the global distribution of strontium (Allègre et al. 2010).

2). The relative dominance of the inputs determines the isotopic composition of the ocean, which is directly reflected in the isotopic composition of marine carbonates. Overall, the rate of Sr removal from the oceans is close to the rate of Sr input, resulting in even gradual shifts in the average Sr concentration in seawater over millions of years (Steuber & Veizer 2002). The strontium isotopic composition of the ocean is homogenous due to its long residence time (~ 2.5 million years) in comparison with the three magnitudes faster mixing time of the ocean (~ 1000 years) (Hodell et al. 1990). This ratio changes over time, reflecting the secular trend of the isotope ratio. The seawater Sr reservoir reacts to changes in its mass balance with a response time of ~1 million years (Richter & Turekian 1993). Because of the long residence time of the Sr in the ocean, it is possible to date and to correlate biogenic calcite worldwide, through the use of a global $^{87}Sr/^{86}Sr$ reference curve (McArthur et al. 2020).

Unlike oxygen and carbon, biological processes and evaporation do not fractionate strontium isotopes, or at least not in a way that alters the $^{87}Sr/^{86}Sr$ ratio. Therefore, the $^{87}Sr/^{86}Sr$ ratio in seawater is constant regardless of depth or location in the oceans. The $^{87}Sr/^{86}Sr$ in marine precipitates reflects the seawater ratio at the time the organism lived, as the ratio in biogenic precipitates undergoes only a minor mass-dependent fractionation during the precipitation process. This fractionation affects the $^{88}Sr/^{86}Sr$ ratio by approximately 0.01-0.03 percent, but it does not affect the measured $^{87}Sr/^{86}Sr$ ratio as the measurement involves normalization to a constant $^{88}Sr/^{86}Sr$ ratio to account for any natural or instrumental isotopic fractionation (Ingram & DePaolo 2022).

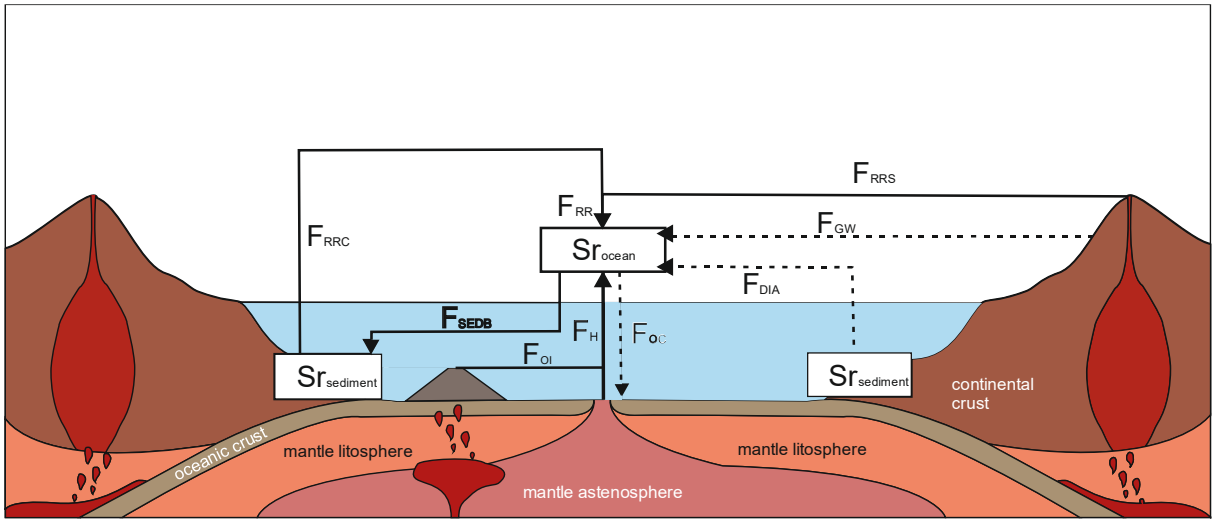

Fig. 3. The Sr cycle and its fluxes. The primary sources contributing to the seawater Sr budget are radiogenic river runoff (FRR) and unradiogenic hydrothermal input (FH). FRR can be further divided into chemical weathering of silicate minerals (FRRS) and dissolution of marine sediments (FRRC). FH consists of the hydrothermal influx and weathering of mid-oceanic ridges, oceanic islands, and island arcs (FOI). Other minor sources of Sr in seawater include ground water runoff (FGW), diagenetic reflux of Sr from recrystallization of sediments and buried pore water (FDIA). At a stable state, the sources of seawater Sr are balanced by the removal of Sr through marine sediment burial (FSEDB) and oceanic crust -seawater interaction (FOC). Major Sr fluxes are indicated by solid lines, while minor fluxes are represented by dashed lines. Reservoirs are displayed in boxes, and arrows depict fluxes. Figure modified after Chen et al. (2022).

2.2 $^{87}Sr/^{86}Sr$ changes in deep time

Peterman et al. (1970) were the first to show that based on fossils from the Phanerozoic, the $^{87}Sr/^{86}Sr$ ratio varied in time, with several highs and lows detectable throughout the Earth's history. In addition, they demonstrated that the composition of the water of present-day seas is uniform with respect to strontium. The modern seawater $^{87}Sr/^{86}Sr$ ratio is 0.709175 (Jones & Jenkyns 2001) (Fig. 2). Since the discovery of the $^{87}Sr/^{86}Sr$ isotope proxy, data has been collected throughout the years from all around the world, with the aim of building a database of stratigraphically constrained strontium isotope data, to generate an accurate record of the change of $^{87}Sr/^{86}Sr$ in time (Burke et al. 1982, Elderfield 1986, McArthur 1994, McArthur et al. 2001, McArthur & Howarth 2004, McArthur 2010, McArthur et al. 2020). The first stratigraphic use of the change of the isotopic values of the Sr was done by Burke et al. (1982), which laid down the basis of the Strontium Isotope Stratigraphy (SIS).

Burke et al. (1982) created the first, albeit still crude reference curve of SIS, by gathering and analyzing samples from the Cambrian till the Quaternary. This method allows the dating and correlation of geographically distant sedimentary sequences without biostratigraphic and geochronological data. By comparing the measured $^{87}Sr/^{86}Sr$ ratio to previously established

calibration curves, stratigraphic and numerical ages can be obtained. The accuracy of strontium isotope dating is dependent both on the analytical precision of the isotope measurement, and the slope of the reference curve. The most precise results can be acquired for well-constrained parts of the strontium isotope curve with a sufficient slope, including intervals in the Late Permian, Late Cretaceous, and Late Paleogene to Recent. However, the accuracy of strontium isotope dating is typically within a range of ±0.1 million years. Comprehensive strontium isotope curves for the entire Phanerozoic Eon have been presented throughout the years (Veizer et al. 1999, McArthur et al. 2001, McArthur & Howarth 2004, McArthur et al. 2020). The accuracy of these curves can be improved through the use of statistical methods (Smalley et al. 1994). To produce reliable curves, the samples used must be well-dated stratigraphically and carefully evaluated for preservation quality. The seawater curves created by McArthur et al. (2020) are widely used in chemostratigraphic dating. The curve uses the LOWESS (Locally Weighted Scatterplot Smoother) statistical method, which is a type of non-parametric regression methods used in statistics and data analysis. LOWESS is a curve-fitting method that is used to smooth out the fluctuations in the scatterplot data and identify underlying trends. The method works by fitting a simple regression model to a small portion of the data, weighted by proximity to the target point, and then repeating the process for each point in the dataset. The result is a smoothed curve that captures the overall trend in the data while reducing the impact of outliers or measurement errors. This way, each time datum has an individual estimated $^{87}Sr/^{86}Sr$ value, with 95% confidence intervals (McArthur 1994). The curve is converted into a look-up table that gives numerical ages, and their 95% confidence limits, for any given $^{87}Sr/^{86}Sr$ value (Howarth & McArthur 1997). On the other hand, for a sample with a known age, its $^{87}Sr/^{86}Sr$ ratio can be used to distinguish between samples that have undergone alteration due to diagenesis and those that have not, as well as between samples from marine and non-marine settings (Wierzbowski 2015, Chen et al. 2022). Lastly, variations in the $^{87}Sr/^{86}Sr$ composition of seawater are likely the result of long-term paleoweathering conditions, and as such, they can be utilized to examine events regarding tectonic activity, biological changes, and climatic feedbacks that have taken place throughout Earth's history (Chen et al. 2022).

The $^{87}Sr/^{86}Sr$ ratio of continentally-derived strontium may have varied due to changes in the types of rocks exposed to weathering (such as granites, basalts, or marine carbonates). However, shifts in the extent of weathered rocks did not seem to have a significant impact on the seawater $^{87}Sr/^{86}Sr$ ratio during the Mesozoic era (Wierzbowski 2015).

2.3 Materials used for measuring $^{87}Sr/^{86}Sr$

To reliably reconstruct the $^{87}Sr/^{86}Sr$ ratio of ancient seawater, the studied material must be well preserved. Even slight alteration of the measured sample can have a substantial impact on the strontium isotopes due to the highly precise measurement of $^{87}Sr/^{86}Sr$ ratios, while secular changes of the marine $^{87}Sr/^{86}Sr$ curve are comparatively slow, averaging 0.000026 per Myr for the last 500 Myr (McArthur et al. 2012, Korte & Ullmann 2018). McArthur et al. (1994) emphasized the importance of the unaltered preservation of samples in order to achieve high resolution Sr isotope stratigraphy. As a result, studies of different periods of the Phanerozoic have increasingly utilized the skeletal material of organisms that secrete low-magnesium calcite (LMC), such as brachiopods, belemnites, and oysters, or bioapatite, such as conodonts, while ensuring the preservation of their samples. Calcite with low magnesium content is known to have high potential for preserving original isotope ratios, this is due to its relatively insoluble nature. Belemnite rostra, oyster, and brachiopod shells made of LMC have been effectively used in measuring the strontium isotope ratios of ancient waters and produced reliable results. Belemnite rostra and brachiopod shells have been found to be the most useful samples for the reconstruction of Paleozoic and Mesozoic seawater due to their resistance to diagenesis (Veizer et al. 1999). The effectiveness of conodonts has proven to be inconsistent, particularly for Sr isotopes. Conodonts are composed of apatite, specifically modern biogenic apatite known as hydroxyapatite. However, in fossil apatite, the hydroxyl (OH) group undergoes partial or significant replacement by secondary fluorine (F), indicating considerable alteration during the burial process (Martin & Scher 2004, McArthur et al. 2020). Studies have found that strontium in conodont elements is more radiogenic than the background (Armstrong et al. 2001). The most optimal samples are found in impermeable host rocks, such as pure limestones, where the pore space is filled with early diagenetic cement, blocking further diagenesis (Ebneth et al. 1997). The crown of conodonts reveals the least altered part of the specimen, aiding in the avoidance of altered areas (Song et al. 2015). The sample quality should improve as the colour alteration index (CAI) decreases, however, the CAI does not indicate diagenesis reliably for $^{87}Sr/^{86}Sr$ (Edwards et al. 2015). Instead, assessing the fluorine (F) content of the conodont may serve as a more reliable indicator of sample quality (McArthur et al. 2020). Based on Ordovician conodonts and bulk carbonates, where conodonts represent the best estimate of $^{87}Sr/^{86}Sr$ ratios, bulk carbonate faithfully records the $^{87}Sr/^{86}Sr$ of seawater as well and provides a high-resolution record (Edwards et al. 2015). While the results from bulk carbonates or foraminifers may be less certain, they still fall within the range of $^{87}Sr/^{86}Sr$ ratios predicted for marine rocks. The

dissolution of bulk carbonate may cause contamination of strontium from detrital aluminosilicate and diagenetic secondary phases, potentially resulting in inaccurate results, therefore proper diagenetic screening is needed (McArthur et al. 2020). Nevertheless, in stratigraphic sequences where well-preserved fossils are scarce or non-existent, such as in the Precambrian or during mass extinction events like the Permo-Triassic or Triassic-Jurassic transitions, the sampling of bulk carbonate rock remains the only practical method for continuous sampling seawater $^{87}Sr/^{86}Sr$ studies (Halverson et al. 2007, Saltzman & Sedlacek 2013, Kovács et al. 2020b, Chen et al. 2022, Onoue et al. 2022). Due to these uncertainties, evaluations of diagenetic alteration are performed on every sample, with the presumption that trends of $^{87}Sr/^{86}Sr$ can be extrapolated from the samples that are determined to be the least altered. While there are established practices for screening samples selected based on petrographic and geochemical criteria, studies have also enhanced the reliability of bulk carbonate in approximating primary $^{87}Sr/^{86}Sr$ trends by refining the techniques used to extract and measure the seawater-derived Sr in bulk rocks (Bailey et al. 2000, Chen et al. 2022).

It is generally observed that diagenesis causes decreased Sr concentration in the samples, and it is accepted that alteration results in more radiogenic, higher $^{87}Sr/^{86}Sr$ ratios (Veizer & Compston 1974). Although these patterns are generally applicable, there are exceptions. Ullmann & Korte (2015) reported that calcite cements can contain substantial amounts of Sr, and altered calcite may also experience ^{87}Sr depletions (lower $^{87}Sr/^{86}Sr$ ratios) due to diagenesis.

2.4 Previous SIS studies of the TJB

Despite several studies investigating the long-term change of the $^{87}Sr/^{86}Sr$ ratio in Late Triassic-Early Jurassic records (Jones et al. 1994, Korte et al. 2003, Callegaro et al. 2012, Tackett et al. 2014, Kovács et al. 2020b, Onoue et al. 2022), a reliable continuous dataset with well-established stratigraphy is still lacking across the TJB. This scarcity of credible and comprehensive $^{87}Sr/^{86}Sr$ datasets hampers our understanding of the factors governing the major environmental changes that occurred during this time, highlighting the need for further data from this time interval.

Nevertheless, based on earlier $^{87}Sr/^{86}Sr$ datasets, a general trend can be outlined. After an increase starting in the Middle Triassic, a decline in the marine $^{87}Sr/^{86}Sr$ ratio began in the latest Norian and spanned the interval of major flood basalt volcanism of the CAMP along the future central Atlantic Ocean. There is a long-running debate, about whether the emplacement of the

CAMP, could have led to a significant change (or any change) in the long-term decrease of the $^{87}Sr/^{86}Sr$ ratio (Jones et al. 1994, Korte et al. 2003, Cohen & Coe 2007, McArthur 2008, Callegaro et al. 2012, Kovács et al. 2020b). The continuing long-term decrease changed to increase in the latest Pliensbachian. Our assesement of the effect of the CAMP eruptions and significant environmental shifts on the rate of change in oceanic strontium isotope ratios depends both on estimates for the duration of the Rhaetian and Hettangian stages, and the efficient filtering of Sr isotope ratios obtained from various sample types (Hesselbo et al. 2002, McArthur 2008).

Korte et al. (2003) presented the most comprehensive $^{87}Sr/^{86}Sr$ isotope dataset from the Late Permian to the Late Triassic, based on brachiopods and conodonts. For the Late Triassic, the study shows a radiogenic trend in $^{87}Sr/^{86}Sr$ values in the middle Carnian-Norian followed by a shift towards more unradiogenic values from the Rhaetian. In the middle Carnian to middle Norian interval, an increase in $^{87}Sr/^{86}Sr$ from 0.70760 to 0.70777 was observed, which was followed by relatively stable but scattered $^{87}Sr/^{86}Sr$ data in the upper Norian with an average of around 0.70805. In their study, from the beginning of the Rhaetian, the samples had $^{87}Sr/^{86}Sr$ values of approximately 0.70784, and a continuous trend towards unradiogenic values close to the end of the Rhaetian. Kovács et al. (2020b) pointed out that there's an uncertainty regarding the inflection point in the $^{87}Sr/^{86}Sr$ curve, where the trend turns towards unradiogenic values, which is due to gaps in the dataset and issues of biostratigraphy.

Callegaro et al. (2012) investigated the Late Triassic $^{87}Sr/^{86}Sr$ based on conodonts from Italy and Cyprus. However, numerous conodont species exhibited a high conodont alteration index, and some samples also yielded highly radiogenic values, therefore making their interpretation questionable. For this reason, the data of Callegaro et al. (2012) is not included in our compilation following the opinion of McArthur et al. (2020).

The narrow interval around the TJB was also studied in more detail by Jones et al. (1994), Kovács et al. (2020b) and Onoue et al. (2022). Jones et al. (1994), based mainly on oysters and belemnites, focused on the Early Jurassic $^{87}Sr/^{86}Sr$ record with some Late Rhaetian data, which revealed a trend towards radiogenic values in the latest Rhaetian that continues into the earliest Hettangian. The highest $^{87}Sr/^{86}Sr$ value recorded at the end of the Triassic was 0.70772 (Jones et al. 1994). With the inability to confidently assign the samples from the White Lias Formation in England to a biozone, the beginning of the trend towards radiogenic values at the Triassic-Jurassic boundary was not well-defined. However, the Rhaetian data aligns well with other data from this time interval (Jones et al. 1994).

From sections in Austria and Turkey, Kovács et al. (2020b) established a high-resolution and continuous $^{87}Sr/^{86}Sr$ record for the Late Triassic based on bulk rock samples. Their data have appropriate biostratigraphic age control and provide relevant information for environmental reconstructions at a regional and global scale, also contributing to global stratigraphic correlation of the Upper Triassic sedimentary records. Their $^{87}Sr/^{86}Sr$ dataset reveals, after a low, more unradiogenic signatures in the Early Rhaetian, the onset of the shift back towards more radiogenic values in the latest Rhaetian (Kovács et al. 2020b) (Fig. 4). The increase in $^{87}Sr/^{86}Sr$ values during the Late Rhaetian up to 0.70771-0.70779 is consistent with the findings of Jones et al. (1994). For the decreasing $^{87}Sr/^{86}Sr$ trend in the Early Rhaetian, Kovács et al. (2020b) proposed three possible explanations: (1) the dissolution of pre-Norian carbonates with low $^{87}Sr/^{86}Sr$ ratios, (2) partial dissolution of marine and continental evaporites with low $^{87}Sr/^{86}Sr$ ratios that were prevalent during the Late Triassic, or (3) the development of

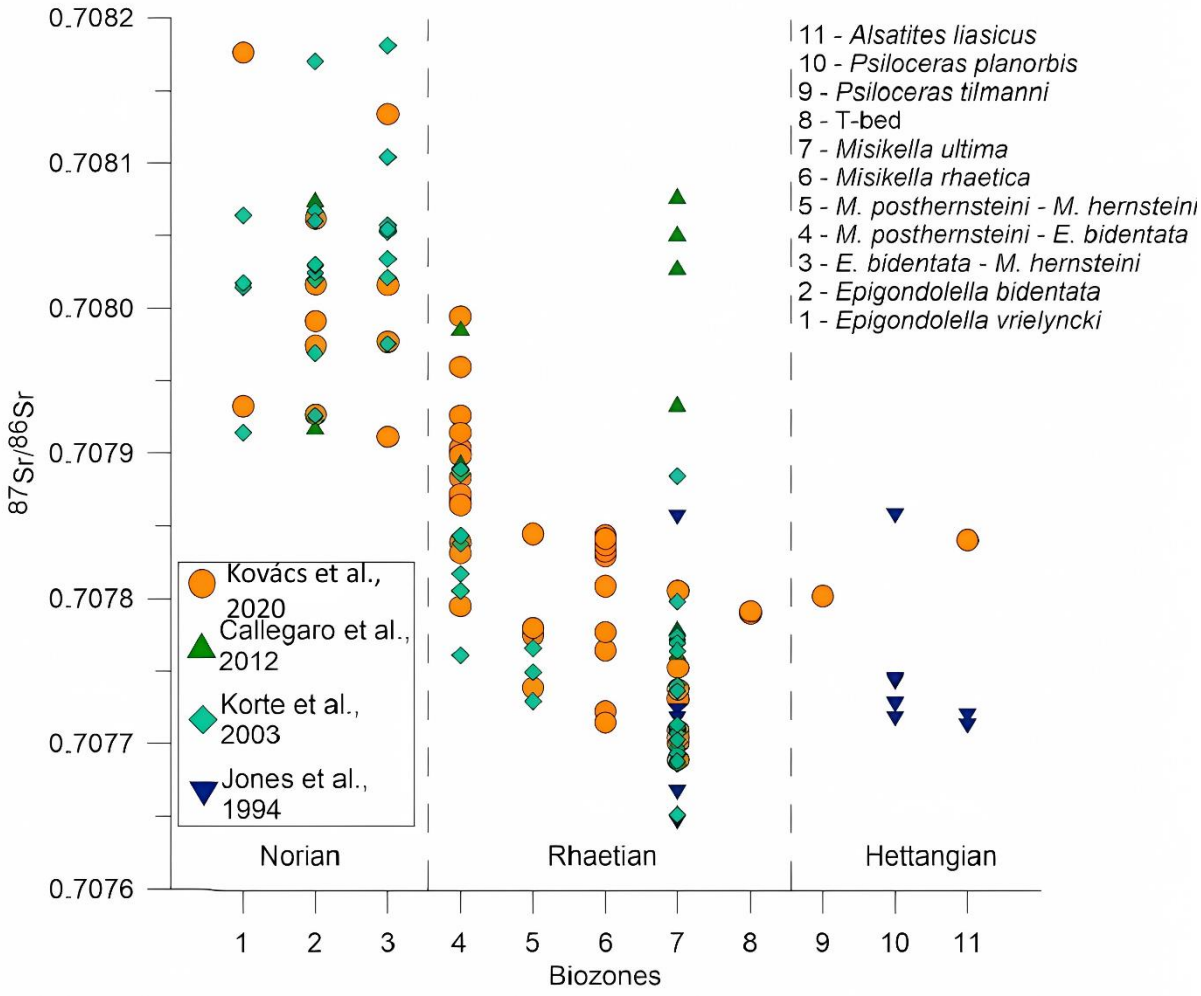

Fig. 4. Strontium isotope data from previous studies for each biozone (Kovács et al. 2020b).

continental rift basins during the breakup of Pangea, which could have led to the influx of isotopically light Sr from the mantle, resulting in lower Sr isotope ratios.

The dataset of Kovács et al. (2020b) also includes two samples from the Hettangian of the GSSP section at Kuhjoch. However, the resolution of sampling at Kuhjoch does not provide a clear contiguous record from the ETE through the boundary interval into the Early Jurassic. There is a ~22 m gap between the latest Rhaetian sample and the first Hettangian. Moreover, the sampling of MS variations for cyclostratigraphy of the Kuhjoch section stops before the first Hettangian Sr isotope sample, hindering accurate correlation and interpretation (Galbrun et al. 2020).

Onoue et al. (2022) studied the Kardolína section in Slovakia to develop a continental weathering record in the NW Tethys during the ETE. The top of the section is in the uppermost Rhaetian, thereby recording the precursor and initial NCIEs. The Sr isotope data supports the declining trend of $^{87}Sr/^{86}Sr$ from the Early Rhaetian. The analysis of strontium isotopes in bulk limestone samples showed a sudden rise in $^{87}Sr/^{86}Sr$ ratios between the P-NCIE and the I-NCIE.

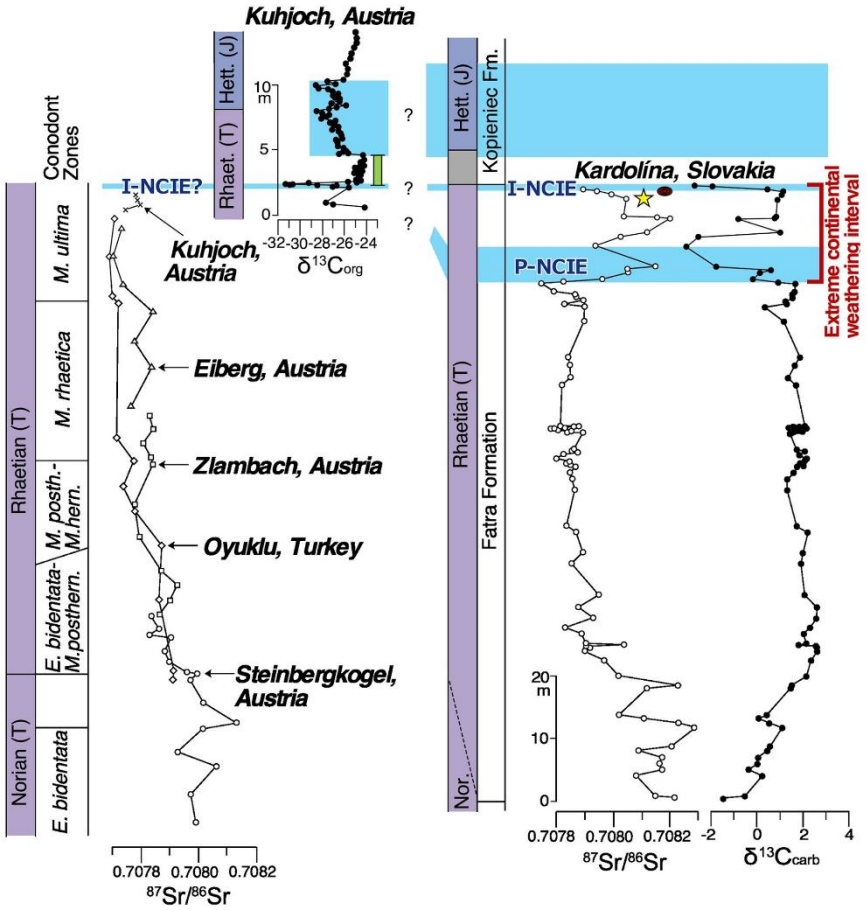

Fig. 5. A comparison of $\delta^{13}C$ and $^{87}Sr/^{86}Sr$ from the studies of Kovács et al. (2020b) and Onoue et al. (2022).

The uppermost Rhaetian displayed an extremely rapid increase in the Sr ratios, indicating a local signal of enhanced input of radiogenic Sr from the Bohemian Massif through continental riverine flux into a confined pull-apart basin of the Fatric Zone (Onoue et al. 2022). As the Sr isotope measurements are limited to a restricted basin in the NW Tethys, they do not reflect the global changes in seawater Sr isotope ratios. Hence, the rise in Sr isotope ratios can not be directly accounted for by changing global continental weathering rates. The duration of the increase in Sr isotope ratios, occurring between the P-NCIE and I-NCIE, is estimated to be around 100-200 kyr, which is shorter than the present-day residence time of Sr in the oceans (about 10^6 years). Therefore, the recorded abrupt shift in the Kardolína section was probably not a global phenomenon. In TJB sections of the Western Carpathians, the Kopieniec Formation that represents the boundary interval, reveals a sudden cessation of carbonate deposition of the Fatra Formation, accompanied by a presumed rise in riverine influence. This abrupt change has been interpreted as a signal of sudden climatic change at the erosional TJB, which could have been caused by a more intense hydrological cycle due to increasing temperatures (Michalík et al. 2007). Also, recent study of the cathodoluminescence of quartz grains in the Kardolína section is in accordance with the changing weathering regime towards the boundary (Vďačný & Michalík 2023). This supports the view of Onoue et al. (2022), that the local weathering regime changed during the TJB.

Possible explanations for these differences between the studies include variations in the carbonate and fossil samples analysed for Sr isotopes or differences between records from epicontinental, shallow, and deep marine environments.

2.5 Insights from $^{187}Os/^{188}Os$ ratios during the TJB interval

Similarly, to the Sr isotope system, the Os isotope system is able to track the changes of chemical weathering. The residence time of Os (10^3-10^4 yr) is much shorter than for the Sr, the Os residence time does not greatly exceed the mixing time of seawater. Hence, it allows perturbations over 10^4 to 10^5 years to be captured by marine $^{187}Os/^{188}Os$ records (Peucker-Ehrenbrink & Ravizza 2020). The $^{187}Os/^{188}Os$ ratio in seawater reflects a balance between the average riverine input and the mantle and extraterrestrial inputs to the world ocean (Ravizza & Peucker-Ehrenbrink 2003). Due to the relatively short residence time of the Os, shifts in the $^{187}Os/^{188}Os$ ratio have been used as chemostratigraphic markers to indicate the onset of major flood basalt volcanisms.

For the Triassic-Jurassic boundary, abrupt shifts have been reported in the $^{187}Os/^{188}Os$ composition of seawater (Cohen & Coe 2002, 2007, Kuroda et al. 2010). The shift is explained by the weathering of young mantle-derived basalts, which resulted in the release of significant amounts of unradiogenic Os (low $^{187}Os/^{188}Os$ ratios) into the global ocean. This signal is similar to the occurrence of local minima and inflections in the marine $^{87}Sr/^{86}Sr$ record, which can be linked to the deposition and weathering of flood basalt provinces.

The Late Triassic-Early Jurassic Sr and Os systems share some similarities. Os isotope analyses for the TJB have identified two stages: (1) decreasing $^{187}Os/^{188}Os$ during the Rhaetian due to mantle-derived unradiogenic Os, and (2) increasing $^{187}Os/^{188}Os$ during the Hettangian due to more radiogenic Os associated with increased continental weathering (Cohen & Coe 2007). It is unlikely that the Rhaetian shift towards unradiogenic values occurred as a result of early CAMP magmatism, as such magmatism is believed to have started no earlier than the latest Rhaetian (Davies et al. 2017). Instead, this shift is likely connected to alterations in global

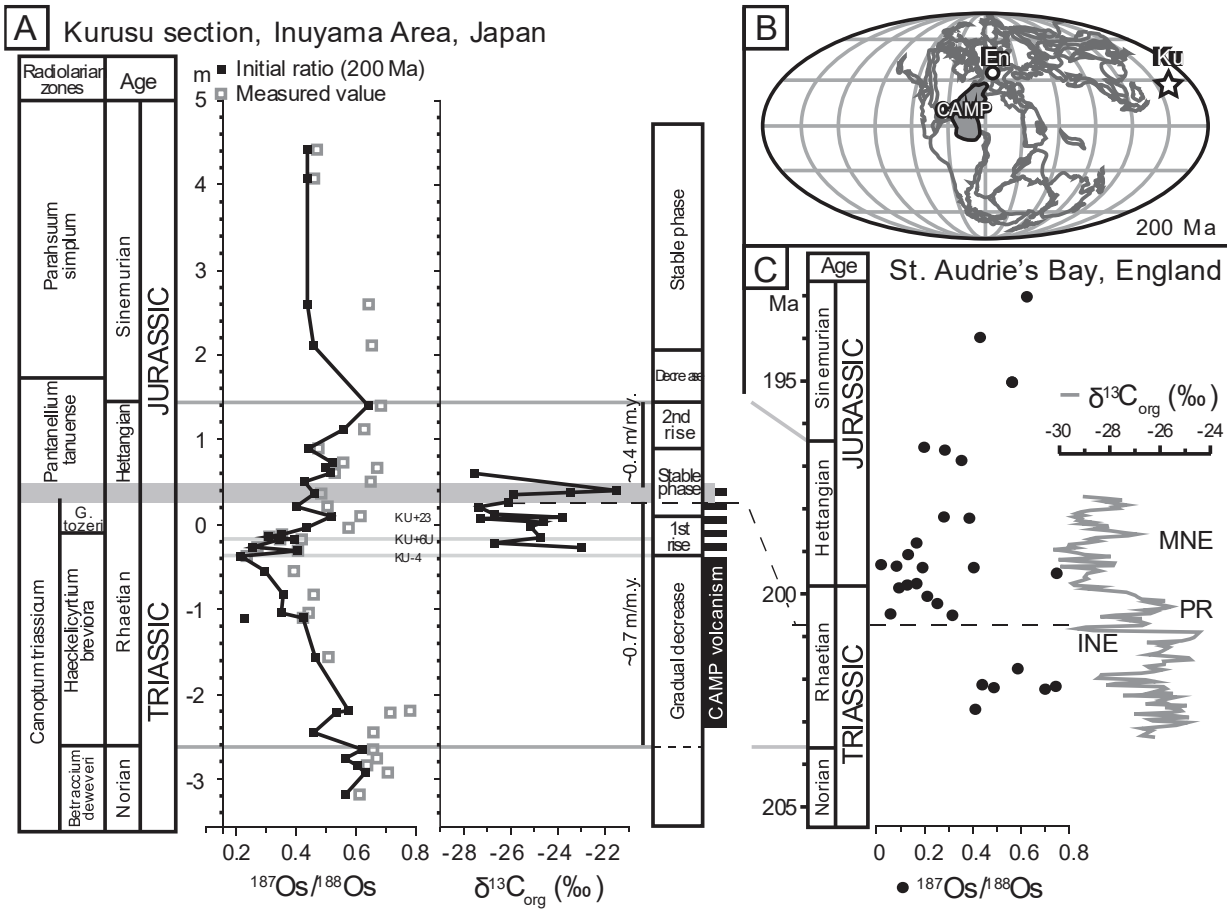

Fig. 6. Isotopic compositions of $^{187}Os/^{188}Os$ and total organic carbon ($\delta^{13}C_{org}$) in Triassic-Jurassic succession from Kurusu, Japan (Kuroda et al. 2010), and from St. Audrie's Bay, UK (Cohen & Coe 2007). Modified after Kuroda et al. (2010)

environmental conditions or plate reorganization. At the end of the Rhaetian close to the TJB, at the time of the CAMP's emplacement, there is an observed shift toward higher $^{187}Os/^{188}Os$ ratios. It is proposed that they are due to enhanced weathering of continental rocks, which are caused by elevated atmospheric CO_2 triggered by the CAMP (Cohen & Coe 2007, Kuroda et al. 2010). The $^{187}Os/^{188}Os$ ratio remained mostly constant throughout the Hettangian.

2.6 The $^{87}Sr/^{86}Sr$ reference curve for the Geologic Time Scale

The Geologic Time Scale (GTS) is a system used by earth scientists to divide Earth's history into distinct intervals of time based on major geological and biological events. The GTS provides a framework for understanding the history of the Earth and the evolution of life on our planet. The GTS is continually refined and updated as new data are available. Ongoing advancements in data collection, improved dating techniques, and a more precise relative scale with well-defined units have stimulated the requirement for a thorough revision of the GTS every in four years. The most recent version of the GTS was updated in 2020 (Gradstein et al. 2020).

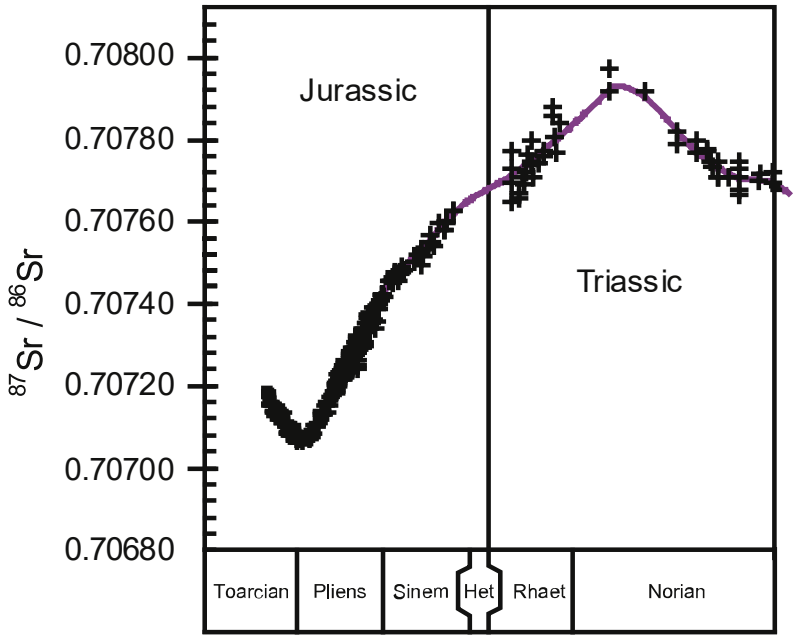

Fig. 7. The reference curve through the Late Triassic-Early Jurassic (McArthur et al. 2012).

Chapter 7 in the subsequent editions of the GTS2004, GTS2012 and GTS2020 summarises Strontium Isotope Stratigraphy (McArthur & Howarth 2004, McArthur et al. 2012, McArthur et al. 2020). These studies contain the most complete compilation of the available Phanerozoic

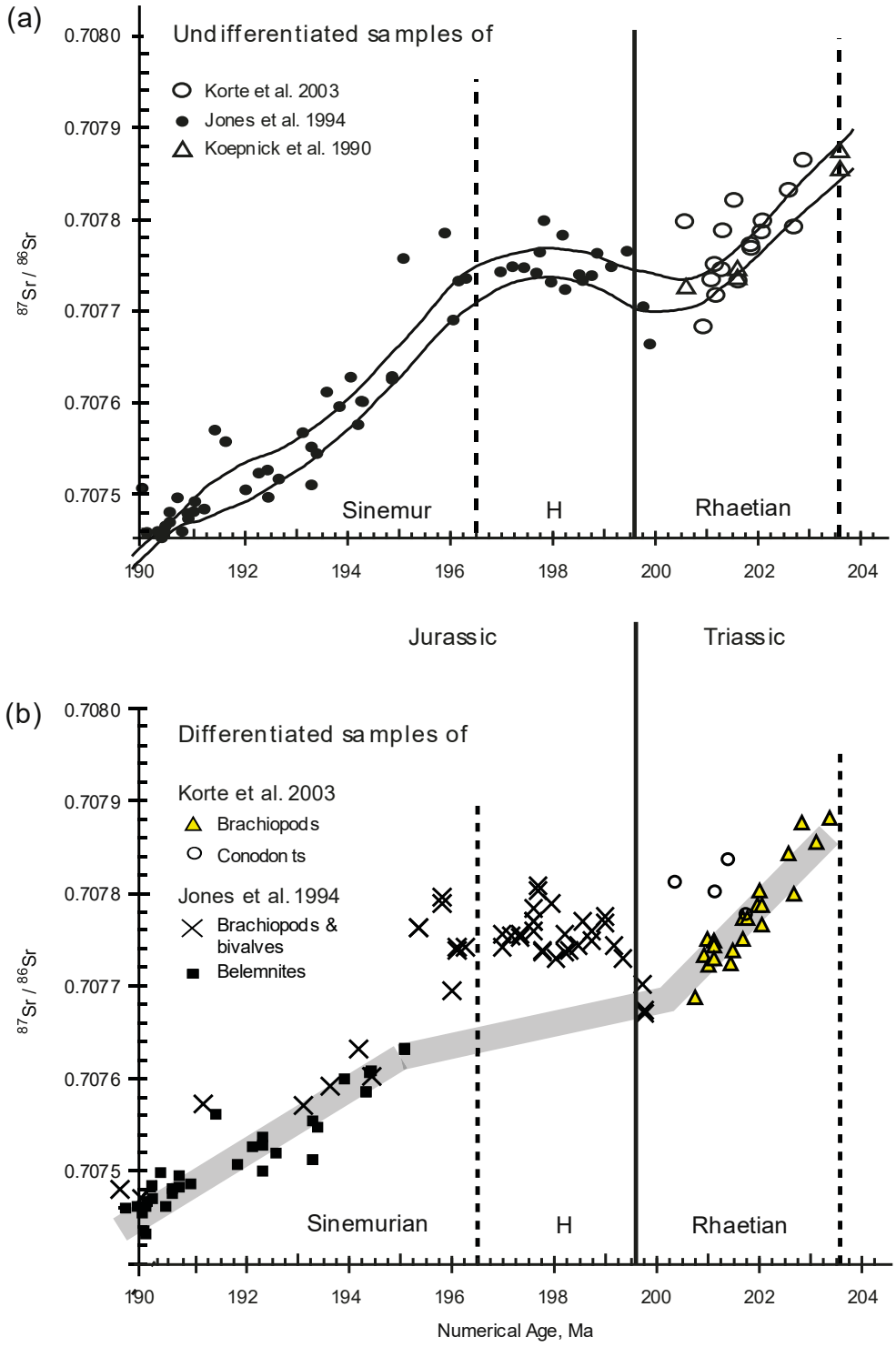

Fig. 8. Different interpretations in the ratio of $^{87}Sr/^{86}Sr$ during the interval spanning the latest Triassic and earliest Jurassic. Model A (a) is used in the GTS2004, Model B (b) rejects conodont and oyster samples and is used in the GTS2012 after McArthur (2008).

$^{87}Sr/^{86}Sr$ data. The variations observed in the $^{87}Sr/^{86}Sr$ ratio are believed to be a characteristic of seawater globally, thus it may serve as stratigraphic indicators for determining the age of the Sr-containing minerals.

The $^{87}Sr/^{86}Sr$ curve across the Triassic-Jurassic boundary has been refined over the years. The data going into these GTS editions are carefully picked based on material, degree of preservation and accurate age constrains. The GTS2004 edition utilizes data for the Rhaetian from various sources, including two data points from Jones et al. (1994), whereas the other data are from Koepnick et al. (1990) and Korte et al. (2003). McArthur et al. (2004) pointed out the potential issues with the data from this time interval: based on these datasets there is a peak towards radiogenic values observed in the latest Triassic, which is based on conodonts that may not accurately preserve their isotope ratios and could result in artifacts. Jones et al. (1994) calibrated their trend using ammonites, whereas Korte et al. (2003) and Koepnick et al. (1990) calibrated theirs using conodonts, leading to a possible mismatch when integrating these different biostratigraphy methods. However, the Rhaetian samples from Jones (1994) align with the Triassic trend observed by the other authors, suggesting that it may be reliable.

In GTS2012, an alternative fit was used for the TJB that excludes the conodont and oyster samples due to their sensitivity for alteration after burial (Fig. 8). In this edition, McArthur et al. (2012) discards the age model and Sr-isotope curve presented in McArthur et al. (2004) for the Triassic-Jurassic boundary, as it includes the oyster and bulk carbonate data of Jones (1994), which they believe to be altered. Instead, the interpretation of McArthur (2008) is preferred, which eliminates the oyster data and minimizes the inflection in $^{87}Sr/^{86}Sr$ across the boundary. The Rhaetian data includes samples from Korte et al. (2003), with the highest values in the latest Triassic omitted because of the higher conodont values of $^{87}Sr/^{86}Sr$ that may reflect alteration.

In McArthur (2008) two models are proposed for the $^{87}Sr/^{86}Sr$ trend through the TJB (Fig. 8). Model A uses the dataset used in GTS2004, which did not differentiate on the basis of sample type. The Model B uses the dataset used later in GTS2012 that rejects conodont and oyster samples. The latest edition, GTS2020 also prefers the use of Model B (McArthur et al. 2020).

3 Geological and stratigraphic setting

3.1 The Csővár section

The studied Vár-hegy section is located near the village of Csővár in north-central Hungary, ~ 40 km northeast of Budapest. The outcrops of the area are situated within the Nézsa-Csővár block, which is bounded by faults and uplifted. This block is a part of the Transdanubian Range Unit and belongs to the Alcapa Unit within the larger Alpine-Carpathian orogenic system (Haas & Tardy-Filácz 2004). It represents the distal margin of the Dachstein Carbonate Platform in the western part of the Neotethys shelf during the Late Triassic - Early Jurassic (Haas et al. 2010). At this time, the shelf was divided by intraplatform basins, such as the Csővár Basin, where the Csővár Formation was deposited. The Pokol-völgy quarry and the Vár-hegy section, both containing exposures of the Triassic-Jurassic boundary, are located west-northwest of the village. These surface outcrops, together with the Csv-1 well that was drilled in the lower yard

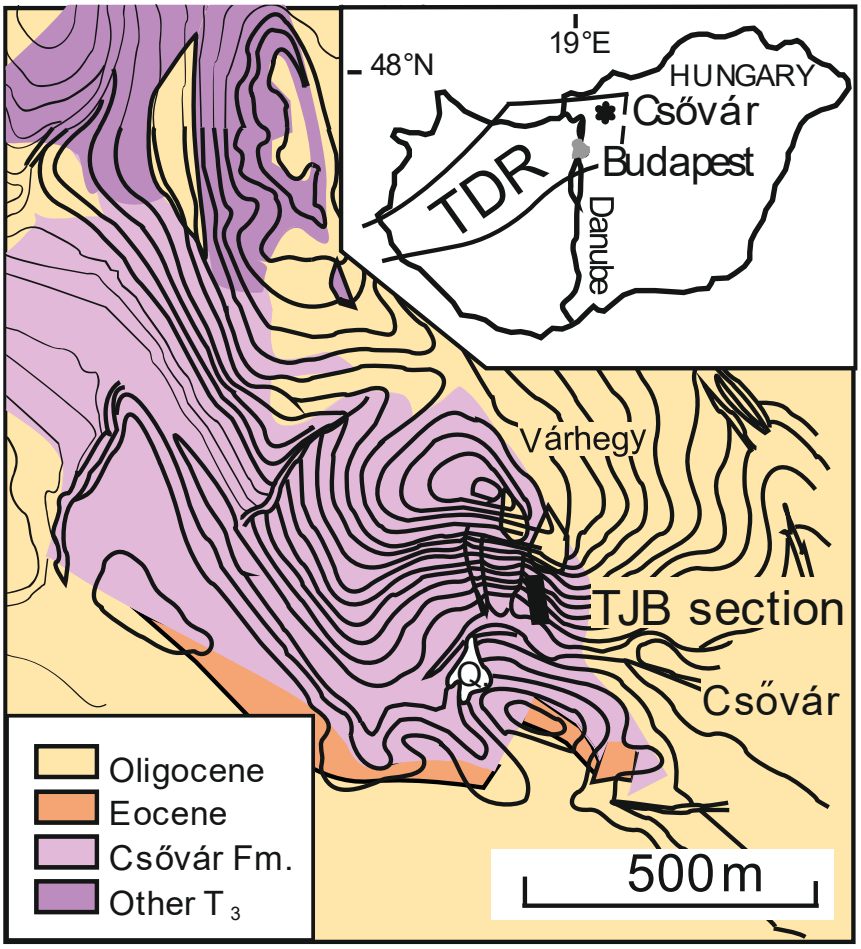

Fig. 9. Location of the Csővár section. TDR – Transdanubian Range, Q. – Pokol-völgy quarry, Fm. – Formation, T3 – Upper Triassic. After Pálfy et al. (2007).

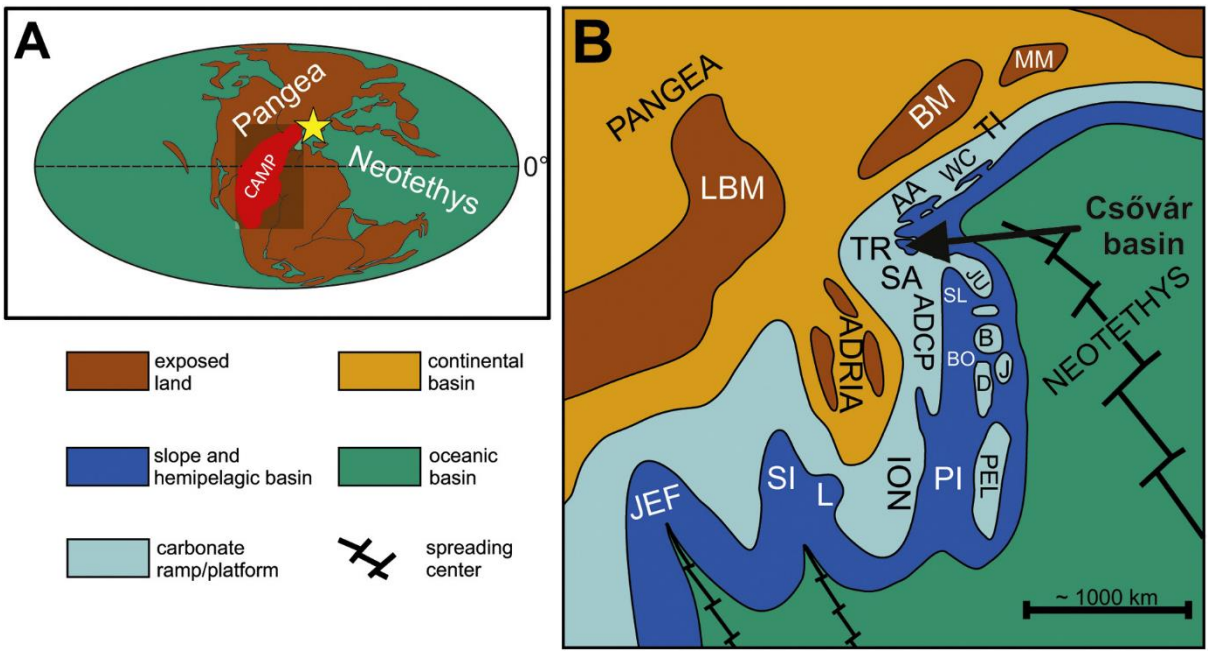

*Fig. 10. Position of the Csővár section in a wider paleogeographical context. After Haas et al. (*2019*) and Kovács et al. (2020a).*

of the Pokol-völgy quarry, provide stratigraphic insights into the Csővár Formation. The formation consists of carbonates deposited in slope and basin environments. The Csv-1 penetrated the lower part of the Csővár Formation, which comprises Upper Carnian to Lower Rhaetian strata (Haas et al. 1997). The basal part of the formation is composed of Carnian cherty dolomite. Overlain by 500 m of thin-bedded, laminated limestone with local chert deposits, representing slope, toe-of-slope and basinal facies (Haas et al. 1997). The upper part of the Csővár Formation is exposed both in the Pokol-völgy quarry and on the steep southwestern slope of the Vár-hegy section in surface exposures and extends from the Upper Rhaetian to the Sinemurian, including the Triassic-Jurassic boundary.

3.2 Lithostratigraphy and basin evolution

The developement of the Csővár basin was strongly influenced by extensional tectonics related to the opening of Neotethys from the early Carnian. The tectonic activity led to the opening of intraplatform basins and also caused significant fluctuations in relative sea-levels (Haas 2002). The Upper Triassic Csővár Formation was deposited on the foreslope of a carbonate platform and in an intraplatform basin. Changes in sedimentation reflect changes in water depth that were primarily controlled by the quantity and composition of sediment transported to the slope and basin. As a result, variations in the amount and composition of bioclasts present in gravity flow deposits can be considered as an indicator of changes in relative sea-levels.

The Csővár Formation ranges from the Carnian to the Sinemurian. The lowermost 100 m of the formation is composed of cherty dolomite. This is followed by a 300-meter-thick interval of cherty limestone, which alternates with crinoidal grainstone, bioturbated beds, and laminated beds. The upper part of the formation, around 200 meters in thickness, is primarily composed of laminated limestone, interrupted by dark grey crinoidal and intraclastic limestone beds. At the Triassic-Jurassic transition, the formation is characterized by brownish-grey micritic limestone, thin-bedded limestone, marl, laminated limestone, and occasional bioclastic and oncoid limestone beds. The uppermost part of the section is dominated by homogeneous, thin-bedded limestone beds (Haas & Tardy-Filácz 2004). From the base, representing Late Carnian – Norian, the Formation is characterized by basin facies dominance. Upwards in the formation, gravity flow deposits such as calciturbidites with fragments of crinoids become more prevalent, suggesting a toe-of-slope depositional environment, towards a trend of platform progradation in the Late Norian (Haas et al. 1997). Based on the abundance of continental sporomorphs, a sea-level fall is inferred for the early Rhaetian, which could have led to subaerial exposure of the adjacent platform. This is followed by a long-term deepening trend till the early Hettangian, revealed by strata exposed at the Vár-hegy section. Occasional slumps in the formation suggest slope instability due to sea-level change. The uppermost part of the quarry and the lowermost part of the Vár-hegy section, display the rise in relative sea level from the Late Rhaetian through the Early Jurassic, which led to in a continuing transition from primarily proximal calcareous turbidites to distal ones and lastly to basinal deposits. Lower Hettangian beds found at 32 m above the base of the Vár-hegy section contain reworked sediments such as oncoids and grapestones that could have come from nearby submarine highs (Haas & Tardy-Filácz 2004). Cherty limestone dominates the area above the top of the Vár-hegy section that reaches into the Sinemurian (Kozur 1993).

This study focuses on the Rhaetian to Hettangian Vár-hegy section, as it represents one of the most important, continuous marine sections through the Triassic-Jurassic Boundary (Pálfy & Dosztály 2000). Despite the tectonic activity in the area during the Late Cretaceous-Early Paleogene interval (Benkő & Fodor 2002), the Vár-hegy section remains stratigraphically intact and complete. Microfacies changes across the Vár-hegy section were studied in detail (Haas & Tardy-Filácz 2004). The section consists of several beds with alternating lithologies, including limestone, calciturbidite, radiolarian wackestone, calcisiltite-calcilutite laminite, and platform-derived sediments. The deposition across the Rhaetian-Hettangian boundary was uninterrupted.

3.3 Biostratigraphy

The fossil record of Csővár, including ammonoids, conodonts, radiolarians, foraminifera, and palynomorphs is generally sparse. However, the available fossils have been used to construct a detailed biostratigraphic framework that allows for the appointment of the Triassic-Jurassic boundary within a limited stratigraphic interval. The section lacks the base defining ammonite of the Jurassic, the first occurrence of *Psiloceras spelae tirolicum* (Hillebrandt et al. 2013). Throughout the section only a few poorly preserved ammonites were found. Pálfy et al. (2000) illustrated important findings, with their ranges and zonal assignments, which allowed the identification of the uppermost Rhaetian Marshi Zone based on *Choristoceras* and *Cladiscites* from the lowest 10 m. The TJB interval had only *ex situ* phylloceratids, but the first Jurassic psiloceratid ammonoid found *in situ* was discovered at 29.5 m, and *Waehneroceras* sp. collected at the highest part of the section (~54 m) indicated the middle Hettangian. Kovács et al. (2020a) reported *Schlotheimia* sp. and Juraphyllitidae gen. et sp. indet. near the same level at around 52 meters, which suggest the base of the upper Hettangian *Marmorea* Zone.

Radiolarians in the section point out the uppermost Rhaetian *Globolaxtorum tozeri* Zone, which is found at approximately at 1.5 meters (Bed 4), while the lower Hettangian *Relanus hettangicus* Zone is identified at around 26.5 meters (Bed 62) (Pálfy et al. 2001, Pálfy et al. 2007).

The presence of conodonts also provides biostratigraphic correlation (Kozur 1991, Karádi et al. 2019). Initially, the lower part of the section was classified into the *Misikella posthernsteini* conodont zone, but according to recent studies, the whole lower 10.5 meters (up to Bed 29) can be attributed to the *Misikella ultima* Zone (Karádi et al. 2019). One specimen of Misikella ultima was found at 20.9 m (Bed 54), however reworking cannot be excluded. The highest conodont occurrence of *Neohindeodella detrei*, was found at 31.7 m (Bed 74) and is believed to be the only survivor of the end-Triassic extinction (Kozur 1993, Pálfy et al. 2007, Du et al. 2020).

The foraminifera fauna in the first 12.5 m of the section is rich and diverse, especially between 11 and 12 m, while the assemblages above lack diversity and distinctive Triassic forms. The last occurrence of Triassic foraminifera is at 14.5 m, and the first Jurassic species (*Involutina liassica*) occur at 52 m (Pálfy et al. 2007).

Palynomorph assemblages throughout the Csővár section are characteristic for the boundary interval for the Triassic-Jurassic (Götz et al. 2009). Palynomorphs from the Rhaetian can be found up to approximately 20 meters (Bed 49). There is a marked and abrupt rise in the

abundance of prasinophytes recorded at 18.5 m (Bed 47), which suggests an algal bloom and corresponds with a spore spike associated with terrestrial vegetation changes. This interval represents the highest occurrence of Triassic fossils, with the TJB restricted within a boundary interval of approximately 6 meters, specifically betweem Beds 49 and 62. The lowest Jurassic fossils, radiolarians, originate from Bed 62 (~26.5 m), the palynomorphs show an increasing terrestrial input in the remaining paert of the section (Pálfy et al. 2007, Vallner et al. 2023).

3.4 Chemostratigraphy

Pálfy et al. (2001) recorded first the distinctive negative isotope anomaly associated with the end-Triassic mass extinction from the Csővár section, which was one of the first NCIEs reported globally for the TJB. Initially, 53 bulk carbonate samples were collected from the

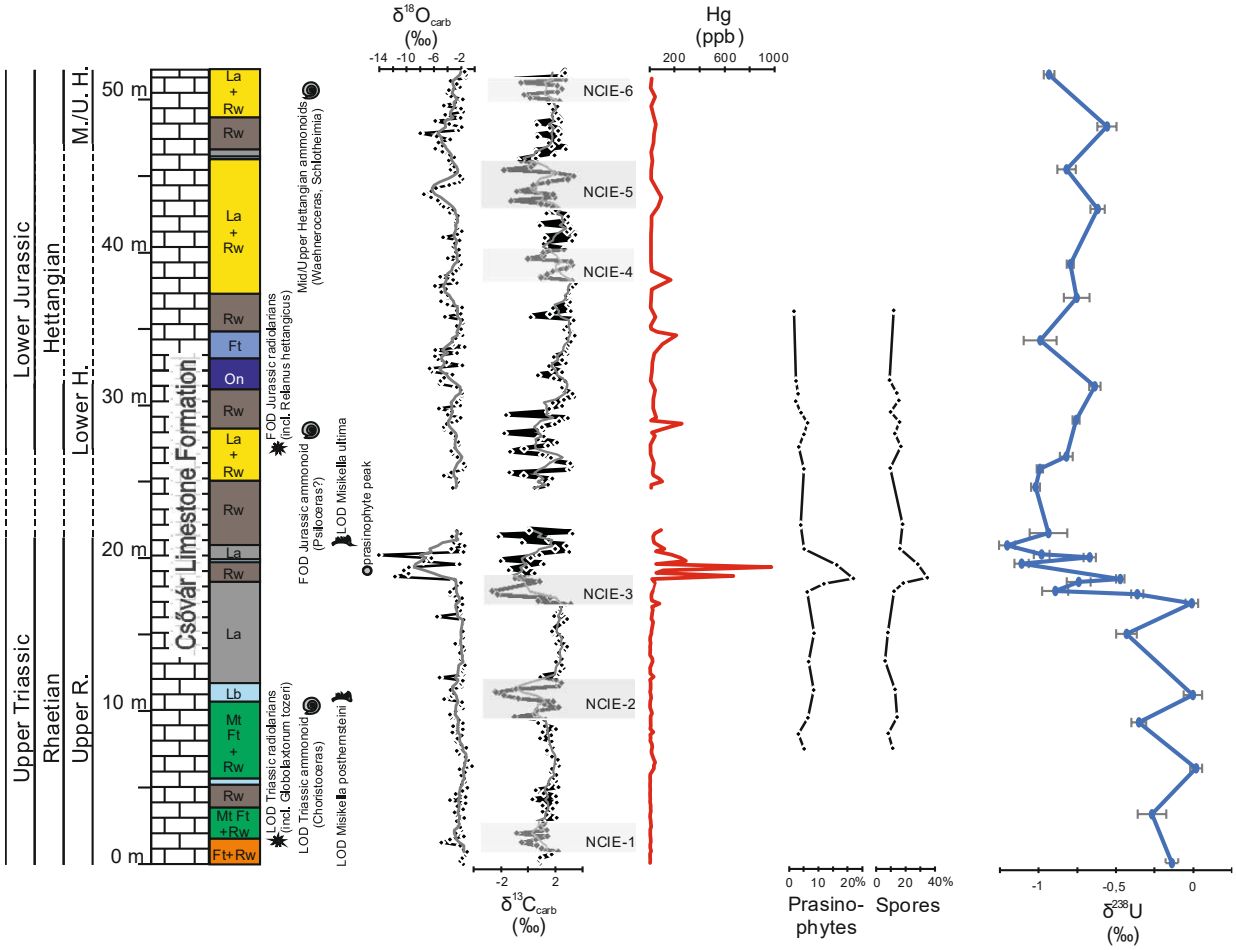

Fig. 11. Recent $\delta^{18}O$, $\delta^{13}C_{carb}$, Hg concentration, and $\delta^{238}U$ data from the Csővár, Vár-hegy section. Lithostratigraphic and microfacies log is from Haas & Tardy-Filácz (2004) and Kovács et al. (2020a). Rw: radiolarian wackestone, La: calcisiltite-calcilutite laminate, Ft: fine-grained turbidite, Mt: medium-grained turbidite, Lb: lithoclastic-bioclastic grainstone/packstone, On: oncoid, grapestone/packstone/wackestone. Biostratigraphy is from Pálfy et al. (2000), Pálfy et al. (2001), Götz et al. (2009) and Karádi et al. (2013). The palynological data is from Götz et al. (2009), the high-resolution $\delta^{18}O$, $\delta^{13}C_{carb}$ and Hg from Kovács et al. (2020a), $\delta^{238}U$ from Somlyay et al. (2023).

section of 35 meters covering the biostratigraphically identified uppermost Triassic to lowermost Jurassic strata in the Vár-hegy section. A major negative peak in the $\delta^{13}C_{carb}$ data was observed at ~18 m and a slightly delayed negative peak in the $\delta^{13}C_{org}$ at ~19 m, which are interpreted as the I-NCIE (Pálfy et al. 2001).

Kovács et al. (2020a) carried out additional, high-resolution geochemical measurements on the Vár-hegy section by resampling it with a 20 cm spacing. The resulting new $\delta^{13}C_{carb}$ data shows a similar pattern to the findings of Pálfy et al. (2001), but with six notable negative carbon isotope excursions, providing an even more precise correlation with other sections across the TJB. The most significant negative peak of approximately 6‰ (NCIE-3) observed between 17-18.4 meters was identified as the I-NCIE. The NCIE-2 at 11 meters could represent the P-NCIE (Kovács et al. 2020a). Notably, the extensive M-NCIE is not clearly evident in the Vár-hegy section.

Kovács et al. (2020a) also studied mercury concentrations throughout the section. At the ETE interval, a significant mercury anomaly was identified, coinciding with the I-NCIE (NCIE-3), and it is suggested to represent the start of the extrusive phase of CAMP volcanism. The highest levels of Hg concentrations were recorded at 18.8 meters (668 ppb) and 19.4 meters (972 ppb). Additionally, in the Hettangian layers of the Vár-hegy section, some less distinctive Hg peaks were detected, which can be linked to additional CAMP volcanic activity.

Recently, Somlyay et al. (2023) analyzed uranium isotopes from the section to assess the global redox conditions during and following the end-Triassic extinction event. The most notable negative $\delta^{238}U$ anomaly was observed between 17.6-21.6 meters, aligning with the I-NCIE and Hg anomalies, suggesting that seafloor anoxia was prevalent towards the end of the Triassic and during the Triassic-Jurassic transition. An unpublished Li proxy study by colleagues from Yale University on the Csővár section is in progress.

3.5 Cyclostratigraphy

The Vár-hegy section section was also subjected to cyclostratigraphic analysis (Vallner et al. 2023). Elemental geochemical data for cyclostratigraphy was obtained through handheld XRF analysis of 243 evenly spaced samples collected at 20 cm intervals. The analysis successfully demonstrated the presence of Milankovitch cyclicity in the section. By analyzing ten elemental time series and stable isotope data series, Vallner et al. (2023) identified cyclic patterns with periodicities comparable to the orbital cycles of the ~405 kyr long and ~124 kyr short

eccentricity, the ~34 kyr obliquity, and the ~17–21 kyr precession. Based on the astrochronologic age model, the measured approx. 52 meter thick section was formed during the span of 2.9-3 Myr, with an average sedimentation rate of 1.73-1.79 cm/kyr. Based on the results, it was possible to estimate the duration of the I-NCIE at Csővár, which is thought to be in the range of 40-80 kyr. Utilizing the Milankovitch cycles and previously published bio- and chemostratigraphic data, it was suggested that the Triassic-Jurassic boundary falls between 21.8-22.2 (Bed 58-59) meters (Vallner et al. 2023).

The geological and stratigraphical framework of the Csővár section is highly relevant for the Sr study since it establishes the foundation for the Sr proxy, given that it is one of the most significant continuous marine sections across the Triassic-Jurassic boundary. This framework provides a contextual understanding of associated events and enables a broader understanding of the processes that contributed to variations in the $^{87}Sr/^{86}Sr$ ratio.

4 Materials and methods

Carbonate samples from the Vár-hegy section at Csővár were collected in the field in Spring 2018 by Joachim Katchinoff and colleagues, helped by Emma Blanka Kovács and József Pálfy. In total, seventy samples were chosen for elemental characterization and for $^{87}Sr/^{86}Sr$ isotope measurements. Samples were collected with varying intervals, but usually around 0.4-1m. Notably, the sampled levels are broadly identical to some of those used for generating a high-resolution stable isotope curve (Kovács et al. 2020a), and for cyclostratigraphic analysis (Vallner et al. 2023). However, the sample resolution around the TJB is higher, each sample was taken every 20 cm. To ensure accuracy, samples were chosen from outcrops avoiding any veins, stylolites, faults, and slumps.

4.1 Sample preparations

When utilizing SIS, it is essential to isolate Sr from the target mineral phase and avoid any contamination from external phases. This is particularly important when conducting whole rock analysis. There are several processes that can overprint the primary isotopic signal of carbonates, e.g. diagenesis, detrital components etc. Therefore, a detailed screening, dissolution and diagenesis study is required to ensure that the data are valid and acceptable. Fine-grained carbonates (micrite) were used for strontium isotope measurements of the TJB, therefore consistent dissolution-, and screening methods were applied to acquire the best preservation values. Overall, to analyse isotopes in carbonate rocks, petrographic and mineralogical screening must be done.

The workflow includes the following steps:

1) examining rocks under a microscope for signs of diagenesis,

2) collecting sample by micro-drilling and pulverizing pristine calcite,

3) removing impurities by selective leaching of calcite,

4) analysing major and minor elements in the leach solution,

5) isolating Sr by column chromatography,

6) measuring Sr isotopes.

Steps 1 – 4 were done by Joachim Katchinoff and colleagues at Yale University. Step 5, column chemistry and step 6, the measurement of the Sr isotopes were carried out at the Isotope Climatology and Environmental Research Center at Institute for Nuclear Research (ATOMKI) in Debrecen, with the help of László Palcsu and Anikó Horváth, with my participation.

At Yale University, samples were cut and micro-drilled while avoiding any visible veins and surface weathering. Petrographic analysis was done by preparing thin sections from the cut samples. After examination of the thin sections, samples were selected for micro-drilling, based on petrographic observations such as the presence of veins and dolomite. Only well-preserved parts of the polished samples were micro-drilled using a tungsten-carbide bit to obtain powder for leaching.

Strontium concentrations in carbonate samples are generally low, making them sensitive to contamination from other phases during dissolution. This is particularly a concern for detrital silicate minerals, as they can introduce significant amounts of strontium into the sample, skewing the analysis results. Consequently, it is important to use proper sample preparation techniques and to take precautions to minimize contamination when analysing strontium in carbonate samples.

Therefore, samples were subjected to the following procedures:

Pre-leach:

Samples were treated with 1 M ammonium acetate for a period of 30 minutes to remove loosely bound Rb and Sr cations. After that, they were centrifuged, with the supernatant being discarded and the solid powder being washed with ultrapure water (UPW; Merck, 18 MΩ·cm). This step was used to remove any sorption, exchangeable ions from the samples.

Leaching:

To target the calcite phase, while avoiding any dissolution of detrital phases in the samples, leaching is required. After the pre-leach, the samples were digested in dilute, 0.02N HCl for 4 hours, then centrifuged and the supernatant collected. This was repeated for 2 hours, then for 10 minutes of digestion.

Measuring major and minor elements:

The ratios of elements such as Li, Mg, Sr, Al, Mn, and Fe relative to Ca were determined using a Thermo Scientific Element XR ICP-MS (Inductively Coupled Plasma Mass Spectrometer) at

the Yale Metal Geochemistry Center. The analysis was performed on a portion of the sample solutions that were first diluted with 5% HNO_3 and spiked with 1 ppb of indium. Based on the measured Sr concentrations in the solutions, a specific amount of the aliquot was pipetted to achieve a target Sr concentration of 300 ppb. The solutions were then evaporated to dryness and placed in Teflon vials. These Teflon vials were shipped to Debrecen, Hungary, for the subsequent column chromatography and the measurement of Sr isotopes.

Column chromatography:

Column chromatography is a method of separating and purifying chemical compounds based on their different physical and chemical properties. It involves passing a mixture of compounds through a column packed with a solid adsorbent material. The different components of the samples will interact differently with the adsorbent, resulting in the separation of the components, in this case, the Sr. The column chromatography for the measurement of $^{87}Sr/^{86}Sr$ was done in a Class 1000 cleanroom at the Isotope Climatology and Environmental Research Center at Institute for Nuclear Research (ATOMKI) in Debrecen.

The samples were treated with 67% HNO_3, then dried, this was repeated once. Then 4x1 ml of 8M HNO_3 was added to the samples. This aliquot went on the cleaned column. The cleaning process of the column is the following:

Column cleaning:

Washing: 5 x 4 ml UPW (Ultra Pure Water)

Filling: 2 x 4 ml HNO3

Washing: 5 x 4 ml UPW

This is repeated once.

Conditioning:

Applying 2 x 4 ml of 8 M HNO_3 and setting up the rasin. Crown ether-based Sr-Spec Resin (100–150 μm particle size) from Triskem International, France was used. Then the sample goes through the column (1 x 4 ml), which takes approximately 2 hours.

Elution:

When the sample has gone through the column, we close the column, wait 10 minutes, to make sure the Sr is sorbed, followed by the matrix elution with 4 x 4 ml 8M HNO_3. Then the Sr

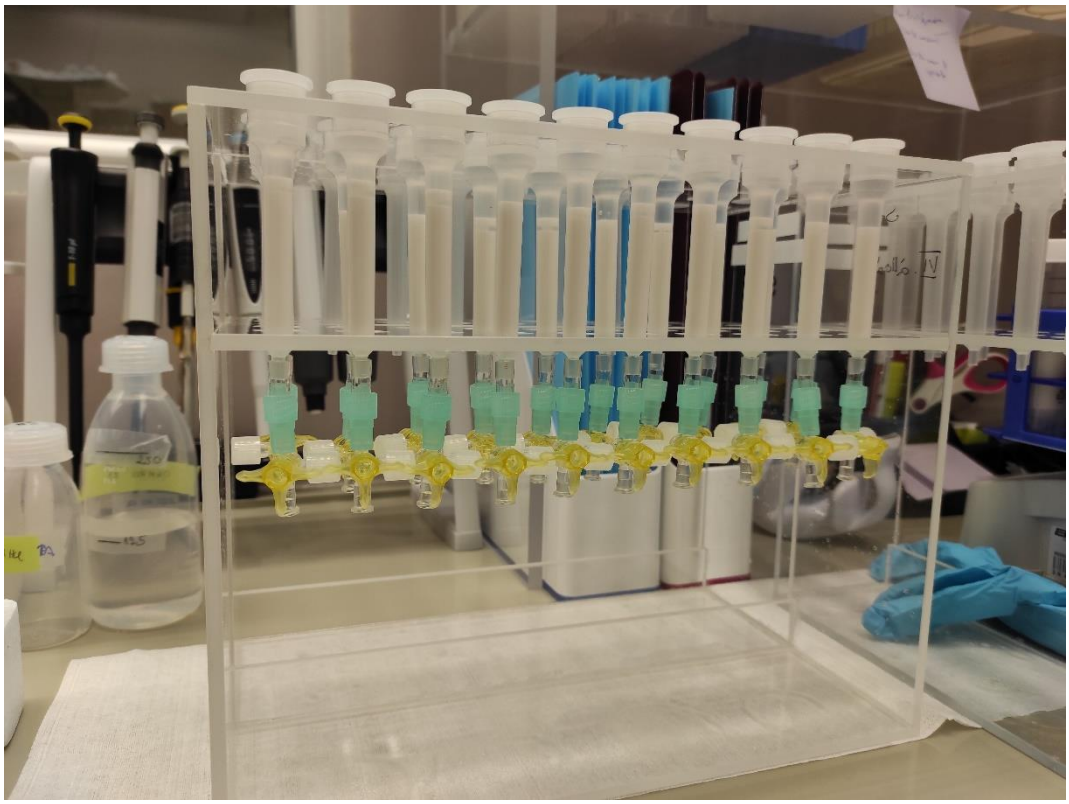

Fig. 12. The column chemistry setup.

sample is eluted with 5 x 4 ml UPW, this way the resin lets go of the sorbed Sr. The sample is then collected and evaporated. Then treated with 2 x 1 ml 67% HNO_3, dried, and lastly the sample is dissolved in 1 ml 3% HNO_3 and ready for measurement.

4.2 Measurements

Strontium isotope ratios ($^{87}Sr/^{86}Sr$) were measured on a Thermo Scientific™ NEPTUNE Plus™ multi-collector inductively coupled plasma mass spectrometer (MC-ICP-MS) equipped with an Aridus-3 (CETAC) desolvation system at the Isotope Climatology and Environmental Research Center at Institute for Nuclear Research (ATOMKI) in Debrecen. The measured ratios were calibrated against the standard NBS987 (NIST® SRM® 987) to the reported value of 0.710248 for NIST SRM 987 (McArthur et al. 2020). The samples were measured in alternation with the standards, following a standard-sample bracketing method, the isotopic value of each sample was calculated by normalizing it with the average of the two standards. Before each sample and standard measurement, the measuring device went through two washing cycles containing 3% HNO_3. The uncertainties of the samples range between 0.000015 (0.0021%) and 0.000033 (0.0045%), with an average of 0.000017 (0.0025%) (±1σ). The NIST® SRM® 987 solution was analysed 9 times and yielded a mean $^{87}Sr/^{86}Sr$ value of 0.710246 ± 0.000005 (±1σ), in good

agreement with previous studies (McArthur et al. 2020). The standards went through the same preparation method as the samples. Based on the results, the reproducibility was 0.000020 (±1σ), 28 ppm. Duplicate carbonate samples that went through the same leach process were within 0.005‰.

Measured isotopic ratios for $^{87}Sr/^{86}Sr$ are corrected for instrumental mass discrimination using $^{88}Sr/^{86}Sr = 8.375209$, as well as by applying an interference correction for $^{87}Rb^{+}$ and $^{86}Kr^{+}$ with $^{85}Rb^{+}$ and $^{83}Kr^{+}$, respectively. to a standard value of 0.1194 for $^{86}Sr/^{88}Sr$ before reporting. This correction compensates for significant isotopic fractionations that arise between ^{84}Sr, ^{86}Sr, ^{87}Sr, and ^{88}Sr during mass spectrometric measurement, and coincidentally removes any natural fractionation (McArthur et al. 2020).

Thirty-one selected samples were run for carbon and oxygen isotopes at the Yale Analytical and Stable Isotope Center, using a KIEL IV Carbonate Device connected to a Thermo MAT 253 Isotope Ratio Mass Spectrometer. Carbon and oxygen isotopes aided in identifying the C isotope excursions associated with the TJB.

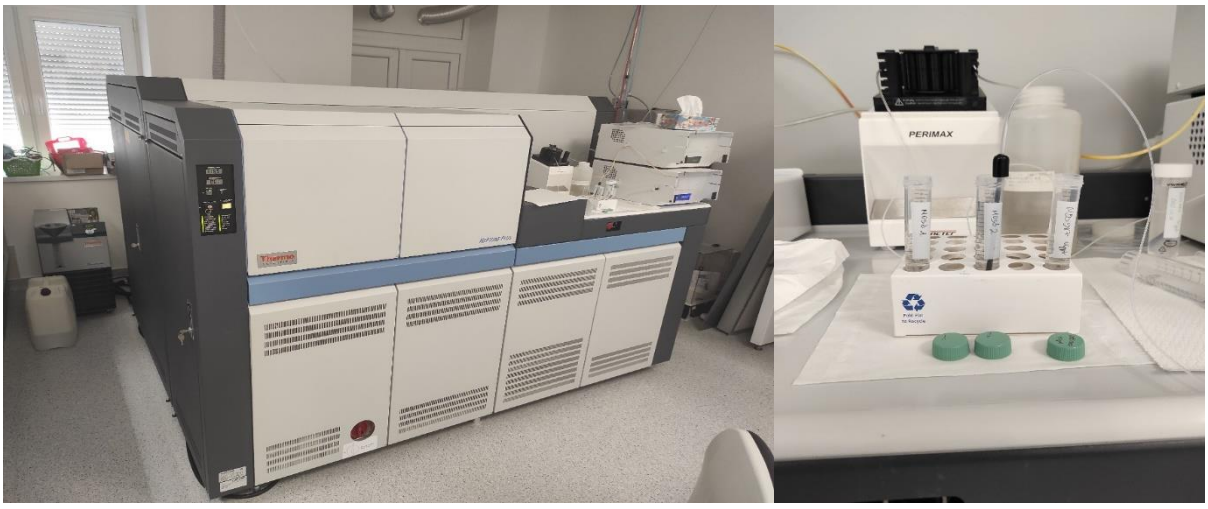

Fig. 13.: The Neptune Plus MC-ICP-MS instrument used for the measurements at ATOMKI in Debrecen

5 Results

5.1 Major and minor elements

The total of 70 samples were measured for major and minor elemental compositions. To accurately determine the most reliable $^{87}Sr/^{86}Sr$ ratios of pristine calcite, I used geochemical indicators, Mn/Sr, Mn/Ca, Mg/Ca, Sr/Ca, and Rb/Sr ratios, to assess the detrital contribution and diagenetic alteration of carbonates. For the Mn/Sr ratio, the samples show an average of 0.17003, a minimum of 0.01287 and a maximum of 3.41425 (ppm/ppm). The Mn/Ca ratio has an average of 0.23928, with a minimum of 0.05 and a maximum of 1.4 (mmol/mol). The Mg/Ca ratio has an average of 0.00602, with a minimum of 0.00238 and a maximum of 0.01147 (ppm/ppm). The Sr/Ca ratio yields an average of 2.12101, with a minimum of 0.24 and a maximum of 3.54 (mmol/mol). The detrital Rb/Sr ratio has an average of 0.00025, with a minimum of 0 and a maximum of 0.00296 (ppm/ppm).

5.2 Stable isotopes

To identify carbon isotope anomalies for correlation, 31 samples were selected and measured for stable isotopes. Carbon isotope values range from -3.6‰ to +3.32‰, with an average of -0.91‰. Oxygen isotope data vary from -5.43‰ to -0.62‰, with an average of -2.23‰. The carbon isotope record is used to identify the major anomalies that are used for global correlation, namely, the P-NCIE, the I-NCIE. The carbon isotope trend correlates well with the previous stable isotope studies of the Csővár section (Pálfy et al. 2001, Pálfy et al. 2007, Kovács et al. 2020a). From the base of the section, the first 10 meters yield values around 1.6‰ on average. At 11 m there is an abrupt negative shift, reaching -0.15‰, after the peak, there is a gap, about 6 m, the trend then returns to more positive values. At 18 m, the record reaches its most negative value of -3.51‰, which is followed by another negative peak, -3.17‰ at 21.65 m. After the major anomalies, there is a gradual return to more positive values, with a longer and more subtle negative shift reaching -0.1‰ at 25.7m. The oxygen isotope values show a similar trend, with an average of -1.4‰ for the first 10 m. A peak of -3.25‰ at 18 m and the most negative value of -3.59‰ at 21.65m. After the peak, the remaining of the section has an average of -2.34‰.

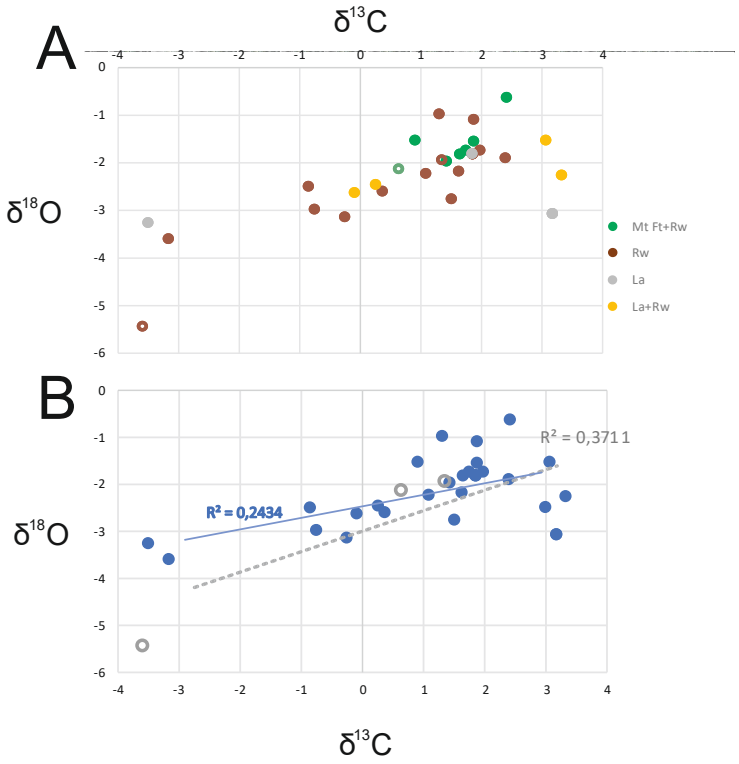

Fig. 14. Stable isotope crossplots. A) Crossplot distinguishing between different microfacies. B) Crossplot with diegenetically overprinted samples in grey circles.

5.3 Strontium isotopes

The $^{87}Sr/^{86}Sr$ ratios range from 0.707625 to 0.708952, with an average of 0.7077, in broad agreement with previous Late Triassic – Early Jurassic SIS studies (Korte et al. 2003, Kovács et al. 2020b, Onoue et al. 2022). The errors associated with each measurement range from 0.000015 to 0.000033, with an average of 0.000017 (±1σ).

The general trend of the profile from the base of the section is a continuous decrease in $^{87}Sr/^{86}Sr$ from 0.70773 to 0.70765 at 13 m, followed by a segment of no change up to 21.5 m, after which there is an increase in the $^{87}Sr/^{86}Sr$ to 0.70771 at 26.2 m and the values remain around 0.707691 up to the end of the section. These long-term subtle trends are interrupted by short-term positive $^{87}Sr/^{86}Sr$ anomalies. Four positive anomalies are distinguished, the first one between 8.8 m to 12.4 m, reaching its peak at 10.2 m, 0.70773, the second one is between 16.9 m and 18.55 m, reaching 0.70769. The third one is between 21 m and 22 m, reaching 0.70771 at 21.2 m, whereas the fourth one is, at 26.2 m, reaching 0.70771.

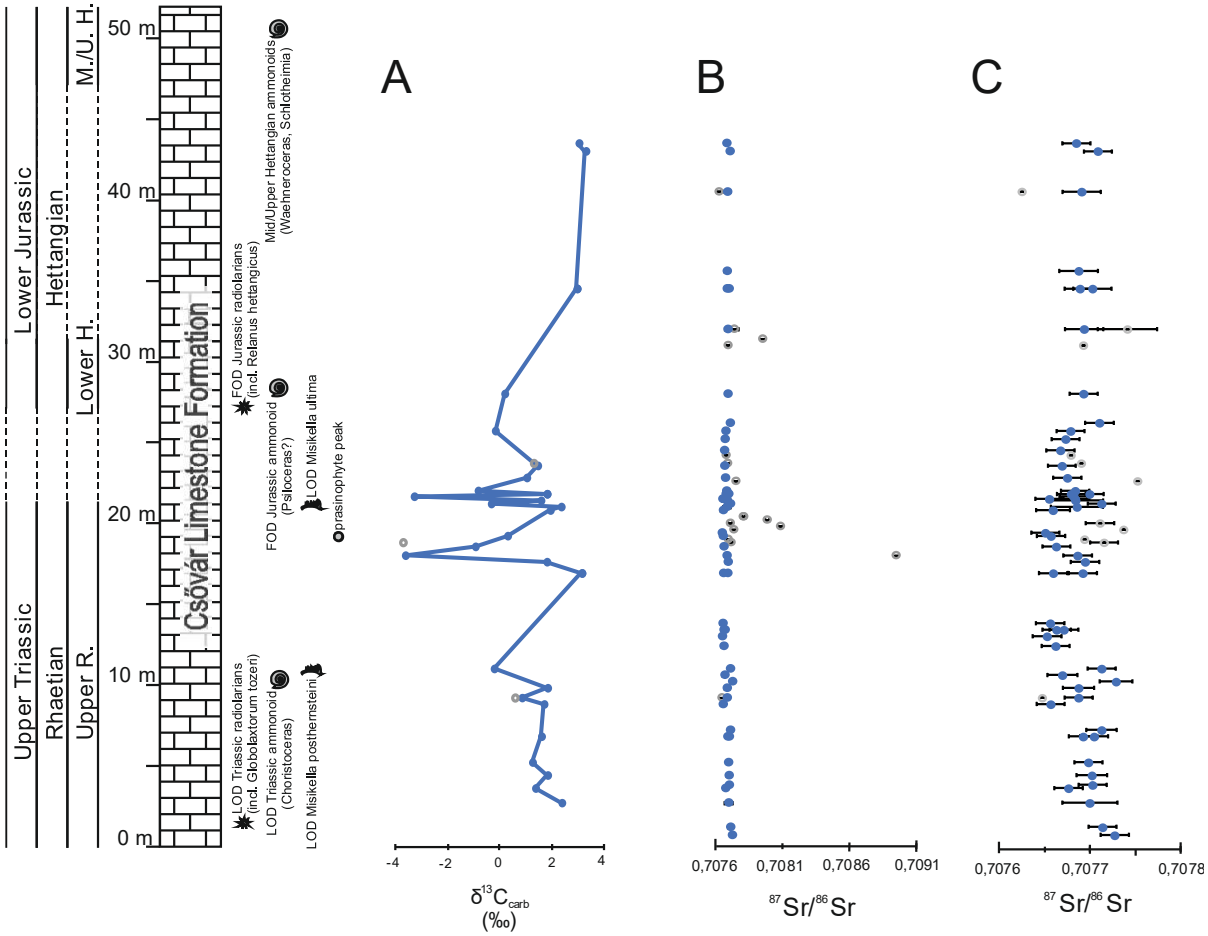

Fig. 15. New geochemical data in litho-, bio-, and chronostratigraphic context from the Csővár section. A) Carbon isotope record across the Csővár section. B) The Strontium isotope ratio changes in full scale. C) The Strontium isotope ratio changes in selected scale. Grey circles show the values deemed to be altered, see discussion in text.

6 Discussion

6.1 Assessment of possible diagenetic overprint

In generating a reliable marine $^{87}Sr/^{86}Sr$ record, the main concern is that the primary signal can be overprinted by diagenetically induced alterations of the $^{87}Sr/^{86}Sr$ ratio in carbonates.

As a case in point, Chen et al. (2022) presented a revised Precambrian seawater $^{87}Sr/^{86}Sr$ curve based on measurements and re-evaluation of bulk carbonates. The study revisited the different dissolution and diagenetic screening methods used in Sr isotopic studies of Precambrian carbonate rocks. In stratigraphic successions where well-preserved fossil material is lacking or absent, as in the Precambrian but also at the Triassic-Jurassic boundary, bulk carbonate rocks represent the only viable option for continuous sampling in seawater $^{87}Sr/^{86}Sr$ studies. Because no skeletal material is available for the TJB, bulk carbonates are commonly used (Kovács et al. 2020b, Onoue et al. 2022). Therefore, screening mainly based on the recommendations of Chen et al. (2022) was applied for the Triassic-Jurassic bulk carbonates from the Csővár section. Here, geochemical element ratios and cross-plot diagrams are used for assessing the past environmental conditions and possible diagenetic processes that impacted the depositional setting and influenced the geochemical signal of the sedimentary sequence (Fig. 16). Geochemical screening was carried out by using four elemental ratios, Mn/Sr, Mg/Ca, Sr/Ca, and Rb/Sr, combined with stable isotope data ($\delta^{13}C$, $\delta^{18}O$).

The Mn/Sr and Sr/Ca ratios are useful geochemical proxies to assess the preservation state of the samples, as enrichment of Mn and depletion of Sr in a sample indicate a change in the post-depositional state and suggest alteration of the primary carbonate. A clear trend in Sr/Ca ratios is observed in samples overprinted by diagenesis. With lower Sr/Ca ratios gradually shifting $\delta^{18}O$ values in the negative-, or $^{87}Sr/^{86}Sr$ values in the radiogenic direction, indicate the effect of diagenesis. Similarly, elevated Mn/Sr ratio is indicative of overprinting.

The reason for the increase in Mn/Sr and usually Fe/Sr ratios during recrystallization is the higher distribution coefficient of Mn and Fe in stable carbonate minerals, such as dolomite and calcite, compared to Sr (Brand & Veizer 1981, Chen et al. 2022). However, this relationship can be affected by various factors, including redox conditions, mineralogy, and diagenetic fluids. High Mn/Sr or Fe/Sr ratios may not necessarily indicate diagenetic alteration, as they could also be a result of carbonate precipitation from anoxic waters. This is because, under

suboxic-anoxic conditions, Fe and Mn have a tendency to revert to their more soluble reduced forms. (Chen et al. 2022).

Secondary calcite has lower Sr/Ca values, therefore as the primary calcite dissolves and secondary calcite precipitates, lower Sr/Ca replaces the primary calcite. Samples shifting towards more radiogenic $^{87}Sr/^{86}Sr$ values while getting more depleted in Sr/Ca represent a clear diagenetic shift, caused by either mixing with freshwater or diagenesis in radiogenic matrix (Korte & Ullmann 2018). This shift, which is attributed to diagenesis in radiogenic matrix is also present in some of our data (Fig. 16). Ullmann & Korte (2015) presented Sr/Ca limits for LMC macrofossils, however, argued that due to Sr/Ca rartio variations within fossil groups, application of strict cut-off values is challenging. Here, based on clear seclusion of samples with low Sr/Ca ratios (Fig. 16), samples with Sr/Ca<1 are deemed to be diagenetically altered and are excluded from the interpretation.

Using the Mg/Ca ratio together with Mn/Sr and Sr/Ca ratios can help to identify modification of the primary carbonate during dolomitization. Mg/Ca ratios are commonly used to assess the relative contribution of dolomite in samples. For instance, dolomite is typically characterized by Mg/Ca ratios greater than 0.6 (Chen et al. 2022).

The alteration of carbonate minerals commonly affects their Sr isotope composition, making $^{87}Sr/^{86}Sr$ ratio itself useful indicators of diagenesis. Usually, post-depositional processes lead to an increase in $^{87}Sr/^{86}Sr$ values, as silicates with high amount of K that are enriched in ^{87}Rb release ^{87}Sr into interstitial fluids that can be incorporated into the carbonate phases during diagenetic recrystallization. Typically, the most reliable estimates for the $^{87}Sr/^{86}Sr$ ratio of ancient seawater are based on the interpretation of the least radiogenic samples. However, carbonate $^{87}Sr/^{86}Sr$ ratios may be shifted to lower values by fluids that are less radiogenic than contemporaneous seawater, which can be influenced by mafic components, juvenile silicates, hydrothermal fluids, or pressure solution of older, underlying carbonate rocks (Brand et al. 2010, Chen et al. 2022).

The Rb/Sr ratio is commonly used to evaluate the influence of terrigenous input on limestone samples.

I specifically applied the following criteria to ensure that the samples are well-preserved and represent the primary Sr signal.

Mn/Sr < 0.1 Li et al. (2011), Zhou et al. (2020), Chen et al. (2022)

Mg/Ca < 0.05 Li et al. (2011), Chen et al. (2022)

Sr/Ca > 1

Rb/Sr < 0.04 Onoue et al. (2018, 2022)

Samples that do not meet the criteria were excluded from further analysis and interpretation. Overall, 14 samples were considered diagenetically altered based on elemental ratios, and another 3 samples are excluded for their duplicate measurements with significant offsets. I excluded a sample measured at 82.4 m, as it lacks well-defined stratigraphy. In summary, out of the measured 70 samples for Sr isotope stratigraphy, 52 samples were used in the interpretation.

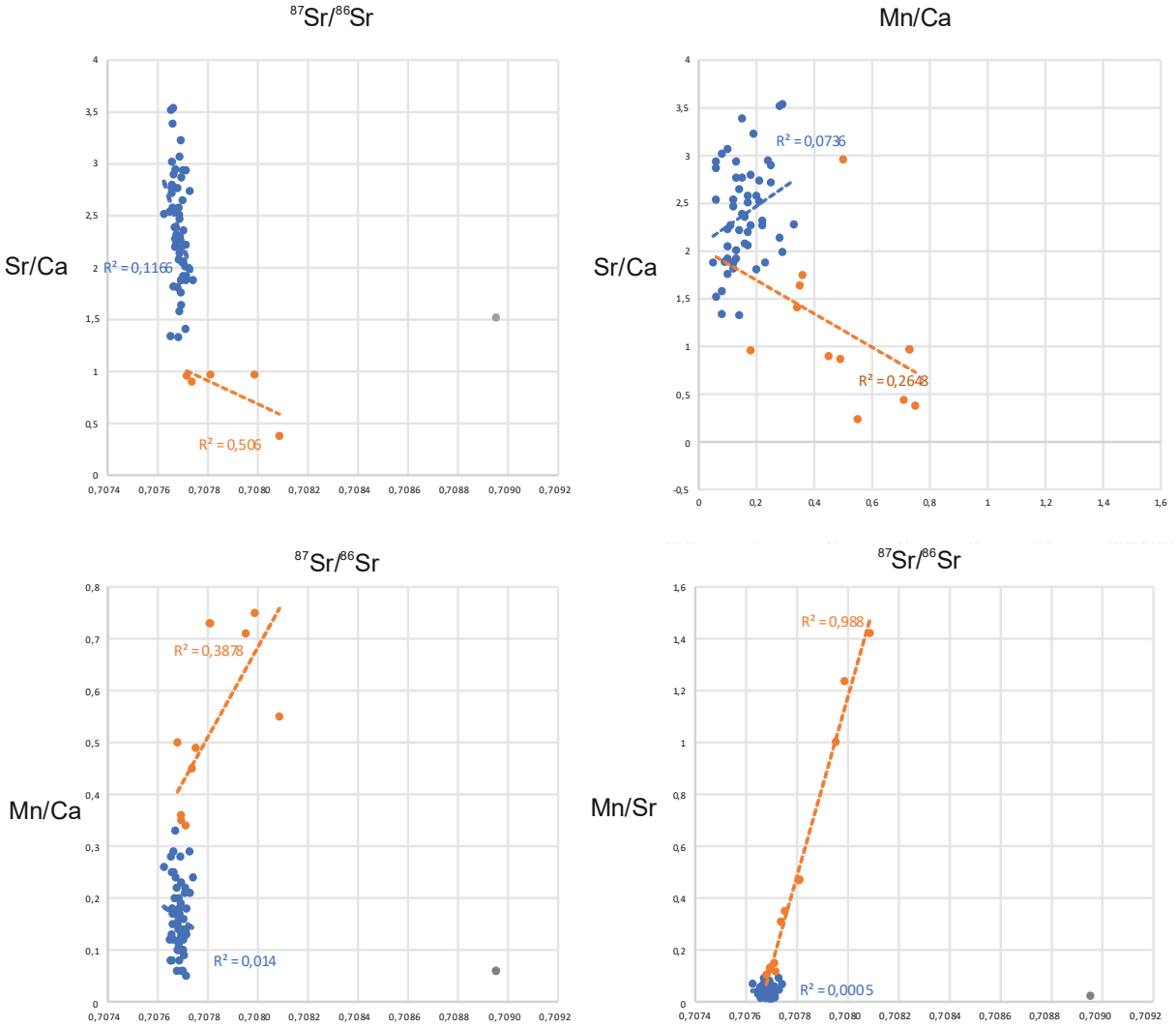

Fig. 16. Crossplots of elemental ratios and $^{87}Sr/^{86}Sr$ ratios. The well-preserved ones are shown in blue and the diagenetically altered ones are shown in orange. One sample with anomalously high $^{87}Sr/^{86}Sr$ ratio is also shown (in grey) but is not included in the linear trend calculation of the altered samples.

6.2 Characteristics of the high-resolution $^{87}Sr/^{86}Sr$ curve from the Csővár section

The $^{87}Sr/^{86}Sr$ profile of the Csővár section carbonate changes gradually with height, which is typical of sedimentary sequences without significant gaps in deposition. This is expected since Sr has a long residence time (> 1 Myr) in the ocean. Since the measured Vár-hegy section records 3 million years of sedimentation (Vallner et al. 2023), the continuous evolution of the global $^{87}Sr/^{86}Sr$ ratio is represented in the long-term subtle shifts in the section. Sudden changes, usually within 1 million years, may represent local weathering changes or the alteration of the original $^{87}Sr/^{86}Sr$ compositions. According to McArthur et al. (2008) and Richter & Turekian (1993), fluctuations in marine $^{87}Sr/^{86}Sr$ within timeframes shorter than 1 million years do not represent the global ocean change. Therefore, rapid short-term changes in the $^{87}Sr/^{86}Sr$ ratio at the Csővár section were caused by local or diagenetic effects.

The trend of the $\delta^{13}C_{carb}$ data from the new suite of samples for Sr analysis agrees well with the values reported in previous studies of the Csővár section. In particular, the new $\delta^{13}C_{carb}$ is comparable with the higher resolution $\delta^{13}C_{carb}$ data of Kovács et al. (2020a) (Fig. 17). The

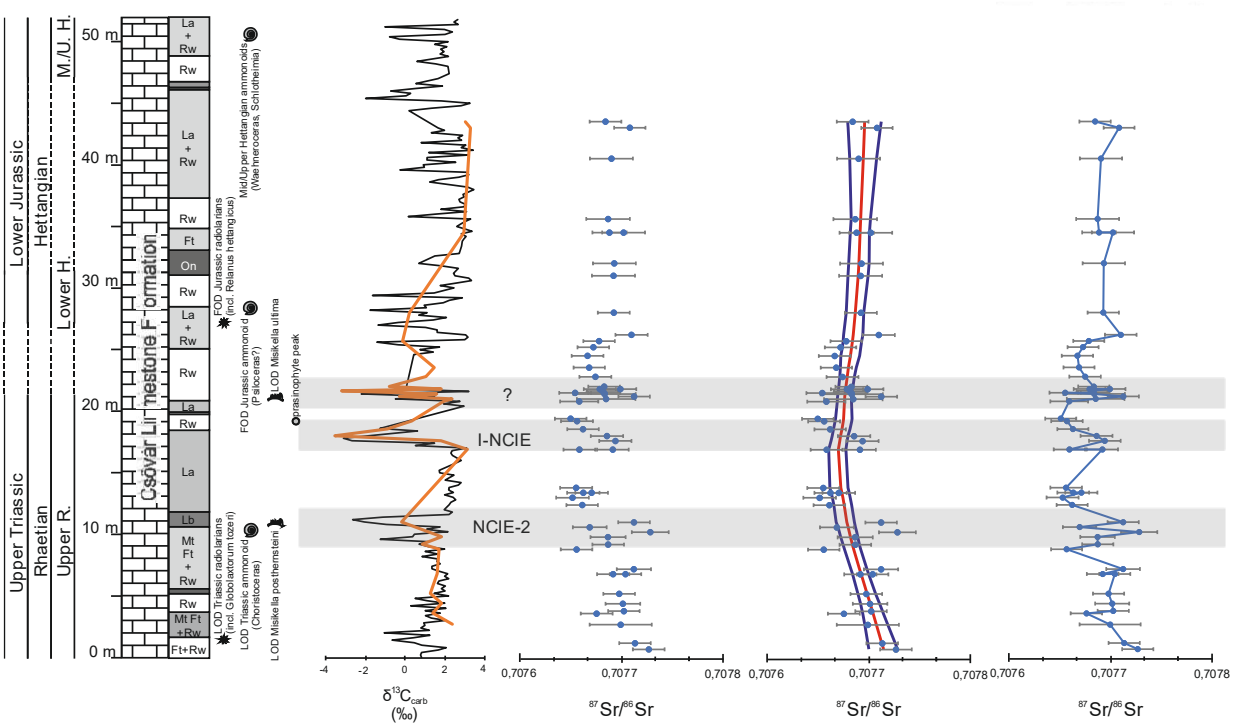

Fig. 17. Variations in $\delta^{13}C$ and $^{87}Sr/^{86}Sr$ ratios along the Vár-hegy section. The black line represent the former $\delta^{13}C_{carb}$ values (Kovács et al. 2020a), while the orange line shows values of this study. The $^{87}Sr/^{86}Sr$ values of well-preserved carbonates are presented in their raw form, as well as smoothed with LOESS (f=0.5) and depicted with a line.

$\delta^{13}C_{carb}$ curve displays major negative isotope anomalies that can be used for global chemostratigraphic correlations.

The base of the Vár-hegy section yields values starting from ~0.70773, which is in accordance with the continuation of the declining trend of Late Rhaetian values (Kovács et al. 2020b), around ~0.70775. A decreasing trend to ~0.70765 continues up to 13 m, which is the extension of the persistent unradiogenic trend from the Late Norian (McArthur et al. 2020). This is followed by a plateau between ~0.70765-0.70766 up to ~20 m. This plateau interval is characterized by the most unradiogenic values in the section and is believed to be a consequence of large volumes of mantle-derived Sr flux to the oceans, which is attributed to the first sign of CAMP activity that coincides with the precursor negative isotope anomaly (P-NCIE) (Heimdal et al. 2020). The supposed P-NCIE (NCIE-2) at the Vár-hegy section is proposed at ~11 m (Kovács et al. 2020a). However, based on cylostratigraphic investigations, the time between the I-NCIE and the alleged P-NCIE is 413 kyr, which compared to other sections, and the duration of CAMP activity is too long (Davies et al. 2017, Vallner et al. 2023). Therefore, I propose that the NCIE-2 cannot be identified as the P-NCIE for the Csővár section. The flattening of the long-term Sr isotope trend could be a response to the start of CAMP activity. The plateau transitions into an increasing trend toward more radiogenic values from ~21.5 m and reaches values around ~0.70769 at ~26 m. This value remains relatively constant for the remainder of the section. The turn to a rising trend in the $^{87}Sr/^{86}Sr$ ratios postdates the I-NCIE, which is believed to start at 17.8m (Kovács et al. 2020a). The rise in the $^{87}Sr/^{86}Sr$ ratios could be caused by the continental weathering increase in response to elevated atmospheric CO_2 levels triggered by the emplacement of CAMP. Therefore, the Csővár section shows that the change in Sr isotope trend is associated with the start of CAMP volcanism and the I-NCIE.

The $^{87}Sr/^{86}Sr$ record of the Vár-hegy section displays three distinct short positive anomalies (Fig. 17). All three anomalies coincide with NCIEs. The rate of change in these intervals is too high to reflect global changes in the ocean system. Considering that the diagenesis screening did not indicate alteration of these samples, the signal is believed to reflect changes in the local weathering regime. Onoue et al. (2022) reported an abrupt shift to radiogenic $^{87}Sr/^{86}Sr$ values from the Fatra Formation, in the Kardolína section, which represents ramp facies deposits along the southern margin of the Bohemian Massif in the NW Tethys region. The Fatra formation was deposited in a pull-apart, semi-closed shallow marine basin, the Zliechov Basin that was a part of the Austroalpine-West Carpathian shelf fragment (Michalík et al. 2007). The rapid shift in the $^{87}Sr/^{86}Sr$ ratio reported from the Kardolína section between the P-NCIE and I-NCIE is

interpreted as an increase in continental weathering in response to large-scale input of CO_2 from CAMP activity. Given that those Sr isotope data originate from a restricted basin in the NW Tethys they do not exhibit global changes in seawater Sr isotope ratios (Onoue et al. 2022). At the P-NCIE, the shift in the Kardolína section changes from ~0.7078 to ~0.7081, which is an increase of 0.0003. For the Csővár section, the concurrent positive Sr shift to the NCIE-2 is from ~0.70766 to ~0.70771, which is an increase of 0.000056. The amplitude of the positive shift in the Kardolína section is more than 5x that of the Csővár section. The differences in the $^{87}Sr/^{86}Sr$ records could be indicative of distinct depositional settings at the two sites. The Rhaetian limestone sequence in the Fatra Formation was deposited on the southern edge of the Bohemian Massif and reflects the increased weathering of the Massif. The Csővár basin, on the other hand, is believed to represent an intraplatform basin close to the distal margin of the Dachstein platform, which may explain why the short-term positive $^{87}Sr/^{86}Sr$ shifts are not as extensive. To understand the global changes occurring during the ETE interval as a response to

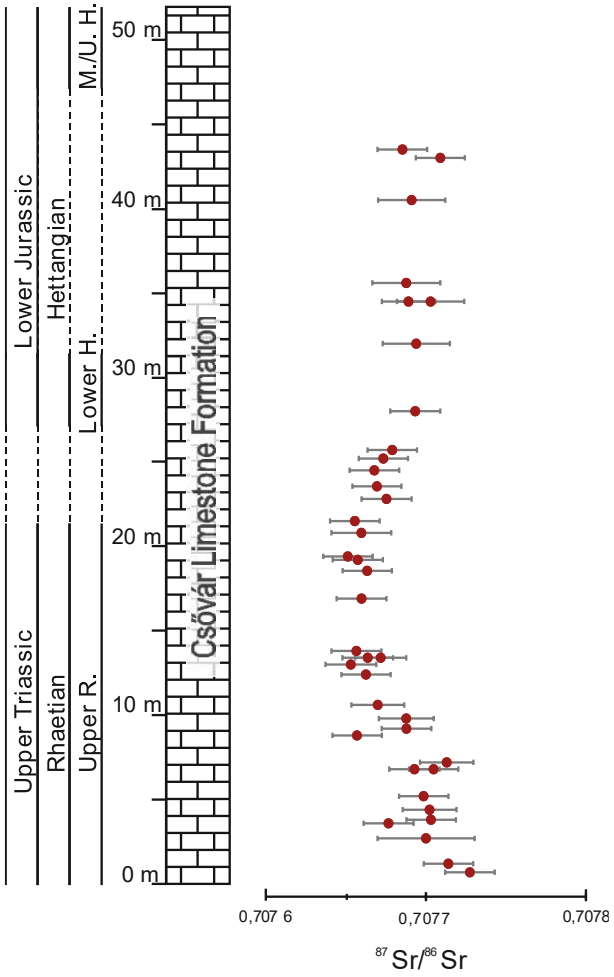

Fig. 18. $^{87}Sr/^{86}Sr$ ratio change across the Csővár section, excluding the values of the positive Sr isotope anomalies.

CAMP activity, elevated atmospheric CO_2 levels, and variations in continental weathering, the long-term $^{87}Sr/^{86}Sr$ values from the Csővár section may be used. For illustration of the global trends, the $^{87}Sr/^{86}Sr$ curve can be plotted after excluding the distinct short-term positive anomalies (Fig. 18.).

6.3 Integrating the new $^{87}Sr/^{86}Sr$ record with other geochemical proxies

The newly obtained data is consistent with previous geochemical studies conducted on the Vár-hegy section and expands our knowledge on the events and feedback mechanisms during the ETE. As previously shown, the carbon isotope trend aligns well with former studies (Pálfy et al. 2001, Pálfy et al. 2007, Kovács et al. 2020a). Kovács et al. (2020a) also presented high mercury anomalies coinciding with the I-NCIE, with Hg concentrations peaks at 18.8 m (668 ppb) and 19.4 m (972 ppb), which is believed to represent the initiation of the extrusive phase of CAMP volcanism (Fig. 19). Additionally, less pronounced Hg peaks were also observed in the Hettangian layers of the Vár-hegy section, which are likely associated with additional CAMP pulses. However, no significant change can be observed before the I-NCIE. Similarly, the $\delta^{238}U$ values display a relatively high average of -0.22‰, with no major shift before the I-NCIE, indicating no significant disruptions in the uranium cycle that could be attributed to the expansion of bottom-water anoxia (Fig. 19). A significant drop in $\delta^{238}U$ to -0.93‰ at 17.6 m indicates a major and abrupt increase in the global extent of bottom-water anoxia (Somlyay et al. 2023). This drop in the uranium isotope record corresponds with the I-NCIE at 17.8 m. The negative CIE is believed to be linked with thermogenic methane discharge (Davies et al. 2017), or the dissociation of methane hydrates (Pálfy et al. 2001), triggered by CAMP. The marked drop in $\delta^{238}U$ indicates a global perturbation of the uranium cycle, which corresponds with the disturbance of the carbon cycle and links CAMP activity and marine anoxia (Somlyay et al. 2023). The extended excursion of uranium isotopes suggests that there were long-lasting oxygen-depleted conditions even after the boundary interval. The radiogenic $^{87}Sr/^{86}Sr$ trend after the event supports this, as the rise in weathering intensity and hence the nutrient delivery possibly triggered an increase in primary productivity. As a result of the flux of less dense freshwater, the water column became stratified, which coupled with the increasing seawater temperatures, caused a decline in oxygen solubility and inefficient ventilation, ultimately leading to the formation and persistence of anoxic conditions.

In contrast, the changes in the $^{87}Sr/^{86}Sr$ ratio across the section appear to commence prior to the I-NCIE. After the NCIE-2 (Kovács et al. 2020a), the decreasing trend of the long-term $^{87}Sr/^{86}Sr$ ratio seems to slow down, resulting in a plateau in the trend between ~11 – 19 m. Prior to the eruptive activity of CAMP, intrusion of dike and sill systems could have resulted in the release of massive amounts of isotopically light carbon, as thermogenic methane from subsurface organic-rich strata (Ruhl & Kürschner 2011, Heimdal et al. 2020). High levels of atmospheric greenhouse gases could have led to intensified weathering. However, the extensive $^{87}Sr/^{86}Sr$ record from Csővár does not show an abrupt shift to radiogenic values before the TJB, this could be a result of the ongoing mantle-derived Sr input from CAMP activity counteracting a forcing towards radiogenic values of the $^{87}Sr/^{86}Sr$ ratios. Any increase in radiogenic Sr was compensated by the unradiogenic Sr input from CAMP volcanism, resulting in a relatively stable $^{87}Sr/^{86}Sr$ ratio in the seawater. Following the I-NCIE, there is a delayed increase in the radiogenic trend of $^{87}Sr/^{86}Sr$ ratio, which persists up to the end of the section. The I-NCIE represents the major volcanic phase of CAMP. During CAMP activity, large amounts of mantle-derived Sr were likely brought to system through volcanic activity, and the weathering

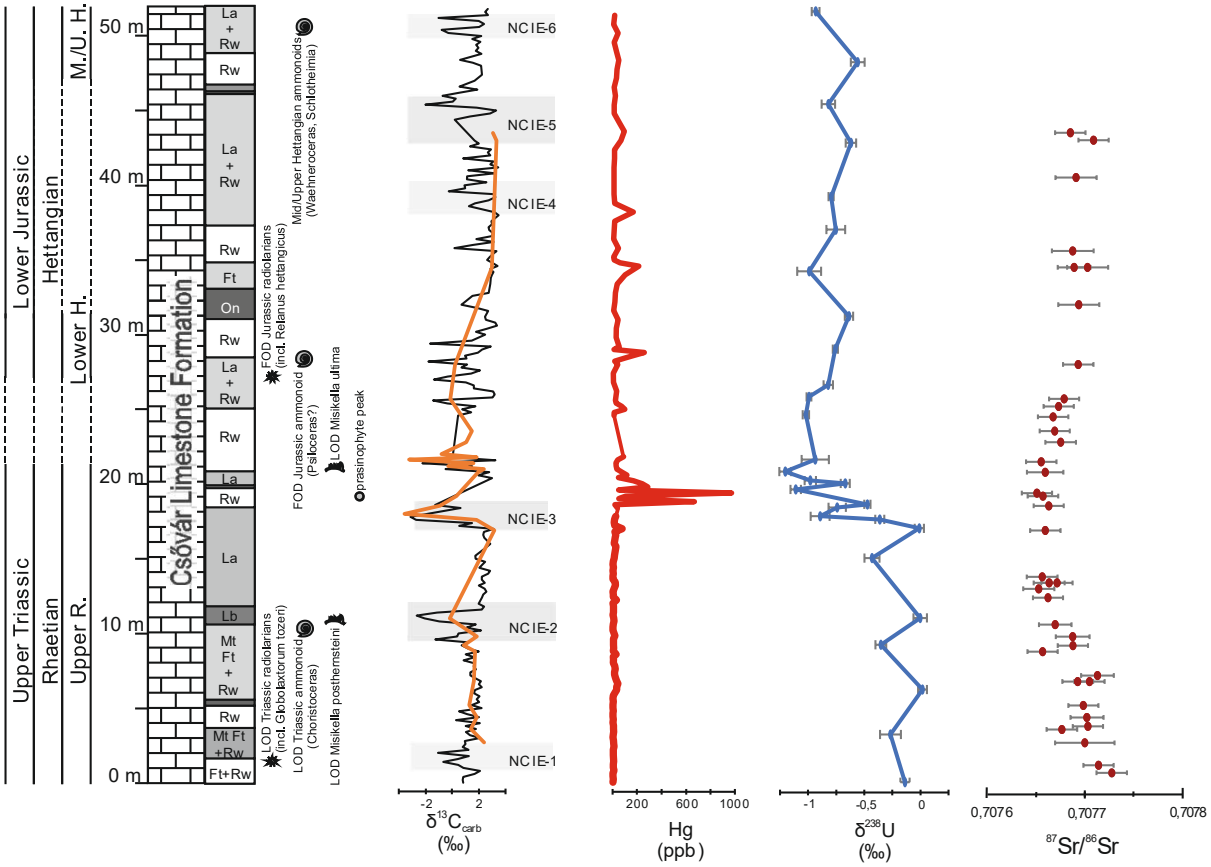

Fig. 19. Multiproxy record of the Vár-hegy section. δ13C from Kovács et al. (2020a) in black, and this study, in orange. Hg concentrations from Kovács et al. (2020a), $\delta^{238}U$ from (Somlyay et al. 2023), $^{87}Sr/^{86}Sr$ this study.

of basalts. Thus, the rise in radiogenic Sr was delayed due to direct unradiogenic influx- and weathering of CAMP, which initially counterbalanced the incoming Sr without significantly increasing the radiogenic Sr fraction. As a result, the amount of radiogenic Sr in the system remained low during the early stages of CAMP activity. Nevertheless, prolonged weathering of continental crust ultimately outpaced the unradiogenic Sr input from the weathering of CAMP-derived basalts. This led to a delayed but significant rise in radiogenic Sr in the system, which was observed after initial CAMP activity. This suggests that prolonged weathering played a crucial role in regulating the geochemical response of the Earth system to CAMP activity.

6.4 Comparison of $^{87}Sr/^{86}Sr$ records from Csővár and the Alpine sections

To establish a numerical age model and to ensure reliable and accurate correlation, we use a cyclostratigraphic framework. Cyclostratigraphy is a powerful tool used to develop a high-resolution geological time scale by identifying and analysing sedimentary cyclicity. This method allows for the correlation of sedimentary sequences between different locations because the time difference between correlation points can be compared, and therefore provides a framework for numerical age control. By analysing the periodic variations in sedimentary properties, such as grain size or geochemical composition, it is possible to reveal cyclical patterns that reflect variations in environmental conditions over time. These cyclical patterns can then be matched with known astronomical cycles, such as the Milankovitch cycles with high fidelity. The use of cyclostratigraphy has become increasingly important in recent years for developing a better understanding of the timing and duration of major geological events, such as mass extinctions and climate change. Therefore, we use recent cyclostratigraphy studies for correlation and to better understand the global changes and the timing of events (Galbrun et al. 2020, Vallner et al. 2023).

Vallner et al. (2023) developed a cyclostratigraphy for the Csővár section that can be used for correlation with Alpine sections. Galbrun et al. (2020) studied representative sections of the Northern Calcareous Alps to constrain the Late Triassic numeric time scale. Importantly, the strontium isotope analyses by Kovács et al. (2020b) were carried out on the same set of sections. Here, the aim was to provide numerical age constraints for the samples analysed for $^{87}Sr/^{86}Sr$ by Kovács et al. (2020b) allowing their direct comparison with the new data from the Csővár section. Because of uncertainties in the methods used by Galbrun et al. (2020), and for more precise correlation, Zsolt Vallner (pers. comm.) reanalysed the dataset from Galbrun et al. (2020), based on magnetic susceptibility variations. Galbrun et al. (2020) reported the results

of cyclostratigraphic analysis of a Rhaetian composite record assembled from four overlapping Austrian reference sections, the Steinbergkogel, Zlambach, Eiberg and the Kuhjoch section (i.e., the Hettangian GSSP). Galbrun et al. (2020) based the correlation of the sections mainly on biostratigraphy and litostratigraphy, however, analysing a composite section, especially if there is a lithological and possibly sedimentation rate change, has its pitfalls. Therefore, the sections were re-analysed for cyclostratigraphy separately. For correlation purposes, we studied sections that have a well-established and constrained carbon isotope record that include the initial carbon isotope anomaly. Here, only the Eiberg and Zlambach sections were studied, because of their reliable geochemical and biostratigraphical control (Fig. 20). Although analysis of the Kuhjoch section was also attempted, it could not be used for assigning numerical ages for the samples studied by Kovács et al. (2020b) for poor preservation of cyclicity. The Eiberg and Zlambach sections were correlated based on biostratigraphy (Galbrun et al. 2020), as the boundary separating the Rhaetian *Vandaites stuerzenbaumi* and *Choristoceras marshi* zones is identified in both sections. The correlation between the Eiberg and Kuhjoch sections is based on the presence of a regional black marly layer, referred to as the "T-bed", located at the top of the Eiberg section and near the base of the Kössen Formation. In these two sections, the T-bed is characterized by a rapid increase in MS intensity and a marked negative carbon isotope shift, the I-NCIE. Through chemostratigraphy, the Alpine sections can therefore be correlated to the Csővár section via the I-NCIE. The numerical age of

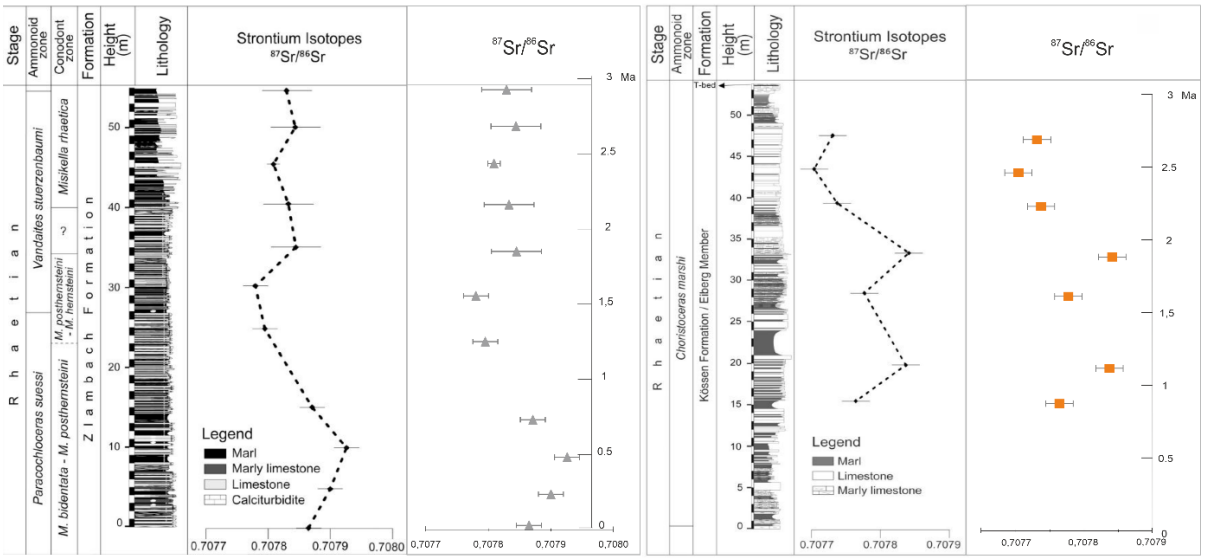

Fig. 20. Result of the astronomically tuned Sr samples on the numerical timescale for the Zlambach (left) and Eiberg (right) sections. The change in deposition rate within a section can slightly alter the samples position to one another on an even spaced numerical timescale. $^{87}Sr/^{86}Sr$ data and visualization from (Kovács et al. 2020b)

the I-NCIE is set to 201.564 (Blackburn et al. 2013, Davies et al. 2017), this is the basis of the correlation between the sections. The age of the TJB is 201.36 ± 0.17 Ma, based on the first occurrence of the ammonoid *Psiloceras spelae tirolicum* (Hillebrandt et al. 2013, Wotzlaw et al. 2014). The correlation between the Zlambach and Eiberg sections is based on the boundary of *Vandaites stuerzenbaumi* zone and the *Choristoceras marshi* zone. In the Zlambach section sampling by Galbrun et al. (2020) extends up to the base of the *Choristoceras marshi* zone. The Eiberg section comprises the entirety of the *C. marshi* zone up to the T-bed. The T-bed can be correlated to the Kuhjoch section and the Csővár section through chemostratigraphy. The numerical age of the top of the Zlambach section (top of the *Vandaites stuerzenbaumi* zone) is thus derived from the astronomically calculated duration of the *Choristoceras marshi* zone (2.96 Myr) extracted from the age of the TJB. This way, the Csővár section can be reliably correlated to the Alpine sections.

The trend aligns well with the long-term Late Triassic $^{87}Sr/^{86}Sr$ ratio decline (Kovács et al. 2020b) (Fig. 21). The astronomical tuning made it possible to build a numerically calibrated composite of the Alpine sections, the Csővár section, and the global seawater $^{87}Sr/^{86}Sr$ curve (McArthur et al. 2020) (Fig. 22). The Kuhjoch section could not be confidently astronomically calibrated, however, the values in close proximity to the T-bed (within 30 cm) have high values (~0.7078) (Kovács et al. 2020b). For the I-NCIE at the Csővár section, samples yield low values ~0.70765 (~0.7077 if positive $^{87}Sr/^{86}Sr$ anomalies are considered). This difference in the values for the two sections is significant, with the values from Csővár being more reliable considering its low values, and the better alignment with the global $^{87}Sr/^{86}Sr$ trend. As for the Hettangian, two samples from Kuhjoch show high values of 0.70784 and 0.70780, which are higher than any other Hettangian data (Jones et al. 1994, Kovács et al. 2020b). This questions the reliability of the samples from Kuhjoch and stresses the importance of more data from the Hettangian.

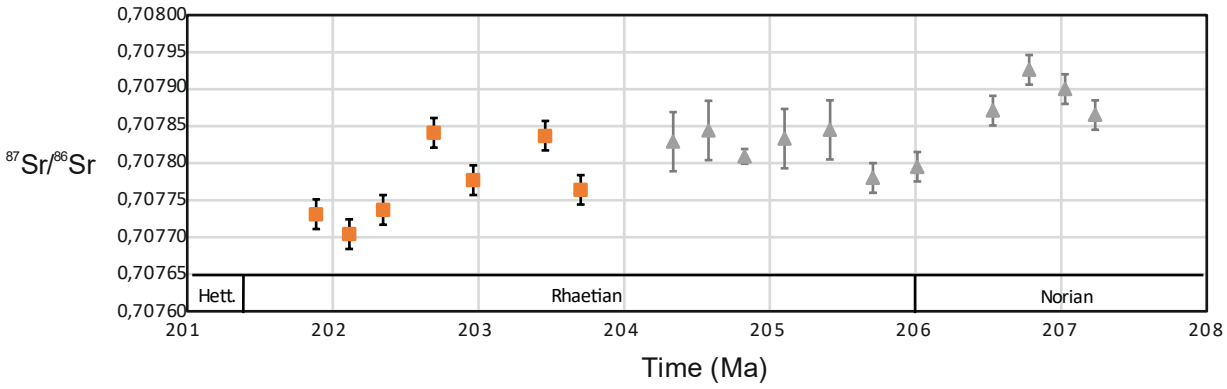

Fig. 21. $^{87}Sr/^{86}Sr$ trend from the Zlambach (grey) and Eiberg (orange) sections with numerical ages from cyclostratigraphy

6.5 Integration of the new $^{87}Sr/^{86}Sr$ record with global data for an improved reference curve

The time interval of the Triassic-Jurassic transition has not yet been studied in sufficient detail for Sr isotopes. The continuous Csővár section provides the first $^{87}Sr/^{86}Sr$ dataset for this interval, filling a crucial gap in the global $^{87}Sr/^{86}Sr$ record for interpreting the ETE interval and thus helping our understanding of the events associated with the TJB. To gain a comprehensive insight into the processes that led to changes in the $^{87}Sr/^{86}Sr$ ratio, it is important to investigate the fit of the data from Csővár to previously published data.

Here, the $^{87}Sr/^{86}Sr$ data of the Csővár section is aggregated with and compared to published data from Jones et al. (1994), Korte et al. (2003) and Kovács et al. (2020b) (Fig. 22). In addition, I also present a comparison with the reference curve of McArthur et al. (2020) (Fig. 24). No conodont data is used in this compilation, due to their sensitivity to alteration after burial, and thus showing significant offset in their $^{87}Sr/^{86}Sr$ values. The reference curve in GTS2020 (McArthur et al. 2020), uses the brachiopod data of Korte et al. (2003) for the Rhaetian, with recalculated numerical ages. For the Hettangian in the GTS2020, no data from Jones et al.

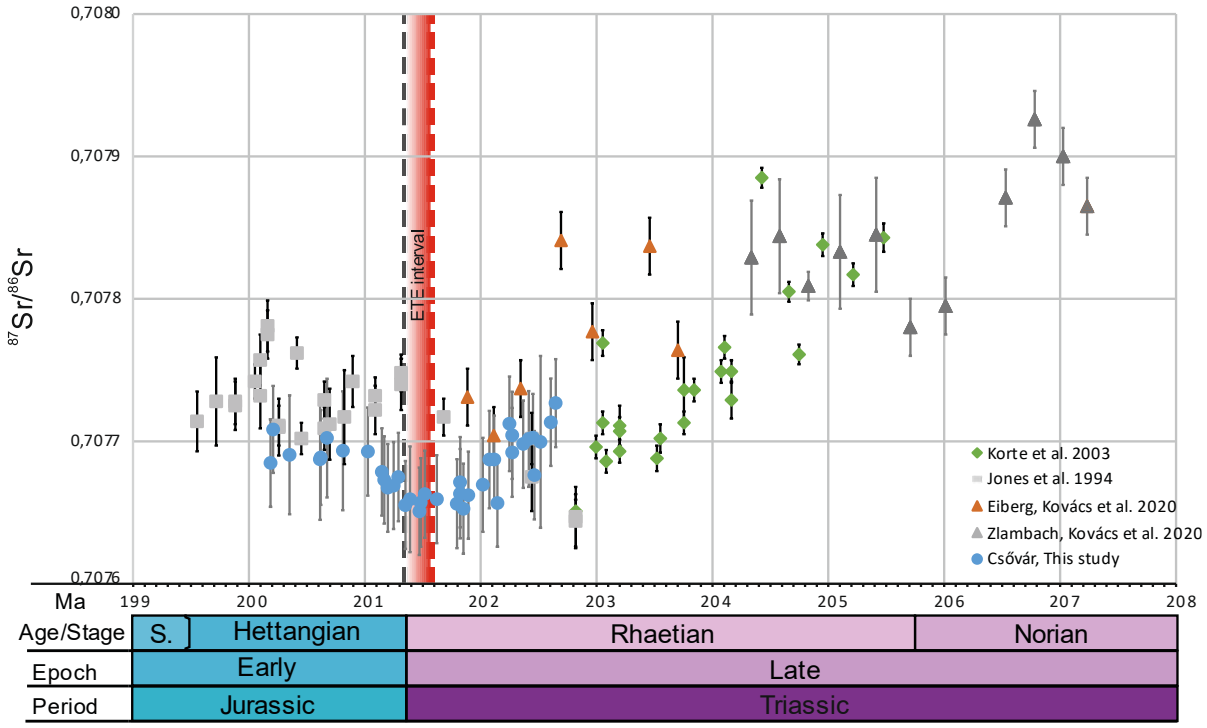

Fig. 22. Compilation of selected $^{87}Sr/^{86}Sr$ data for the TJB interval with error bars (2sd). Diamonds: brachiopods, squares: oysters, triangles: bulk carbonate (Kovács et al. 2020b), circles: bulk carbonate from Csővár. Red dotted line represents the I-NCIE at 201.564 Ma (Davies et al. 2017), black dotted line represents the Triassic-Jurassic boundary at 201.36 Ma (Hillebrandt et al. 2013). All data are recalculated to the Geologic Time Scale 2020 (Gradstein et al. 2020).

(1994) is used due to the proposed secondary alteration of the oyster samples (McArthur et al. 2007a). Here, however, I argue for their fidelity and therefore use the data from Jones et al. (1994) together with those of Korte et al. (2003), all recalculated to GTS2020. The $^{87}Sr/^{86}Sr$ values from Kovács et al. (2020b) and the Csővár section are astronomically calibrated and correlated using the I-NCIE at 201.564 Ma (Blackburn et al. 2013, Davies et al. 2017). For the Csővár samples, to understand the long-term and global changes, the dataset without the values of the positive $^{87}Sr/^{86}Sr$ anomalies is used. This way the ~ 3 Myr Csővár dataset is expanded, and the entire compilation covers ~ 8 Myr.

The published marine $^{87}Sr/^{86}Sr$ data for the latest Triassic and earliest Hettangian are plotted in Fig. 22, along with the data from Csővár. The plot illustrates a continuous decreasing trend from the Late Triassic until the ETE interval. The decreasing trend starts in the Norian, based on the samples from Korte et al. (2003). In a wider context the data of Kovács et al. (2020b) show some scatter, especially for the Eiberg section, however, the dataset displays the overall decrease in the Late Triassic. The long-term decreasing trend continues with the samples from Csővár, and fits well with the data from both Korte et al. (2003) and Kovács et al. (2020b). Based on the Csővár data, the persistent decline of the $^{87}Sr/^{86}Sr$ ratio continues until the ETE, where it turns into a short flat interval of no significant change or trend for ~300 kyr. The trough at the ETE interval is followed by an increasing trend in the earliest Hettangian. The Csővár data connects the decreasing Rhaetian values from Korte et al. (2003) supplemented by the data from Kovács et al. (2020b) to the increasing Hettangian values of Jones et al. (1994), supporting the possibility of the samples of Jones et al. (1994) to reflect the original seawater Sr signal.

Our data from Csővár provide the most detailed resolution for the boundary interval to date. In a global context, the trend, and average values of the Csővár data yield relatively low $^{87}Sr/^{86}Sr$ values, indicating a well-preserved and reliable data (Fig. 22). The trend exhibited by the Csővár samples aligns well with previously published $^{87}Sr/^{86}Sr$ ratios, displaying minimal variation and a distinct and easily comprehensible pattern.

Previously, the interval of the TJB could not be consistently used for SIS, because of the lack of reliable data. The inclusion of samples from the Csővár section significantly extends and enhances the robustness of the global $^{87}Sr/^{86}Sr$ dataset. Incorporating these samples broadens the coverage and increases the overall reliability of the data, thereby strengthening our understanding of strontium isotopic variations on a global scale. McArthur et al. (2007b) deemed the oyster samples of Jones et al. (1994) for the Hettangian altered, based on the high $^{87}Sr/^{86}Sr$ ratios. However, together with the Csővár $^{87}Sr/^{86}Sr$ ratios, they fit into the increasing pattern and thus breaking the extensive Late Triassic – Early Jurassic declining trend. This does not rule out the possibility of alteration of the samples of Jones et al. (1994) entirely, but rather points towards the prospect of reliability and usability of the samples for interpretation purposes. Nevertheless, more data is needed to understand the $^{87}Sr/^{86}Sr$ trend of the Hettangian, to whether accept or reject the samples of Jones et al. (1994). McArthur et al. (2020) only uses the brachiopod data of Korte et al. (2003) for the Rhaetian, for the Jurassic, the earliest datapoints are in the Sinemurian, which are the belemnite $^{87}Sr/^{86}Sr$ ratios of Jones et al. (1994). Hence, the reference curve of McArthur et al. (2020) shows a slight change in slope in the

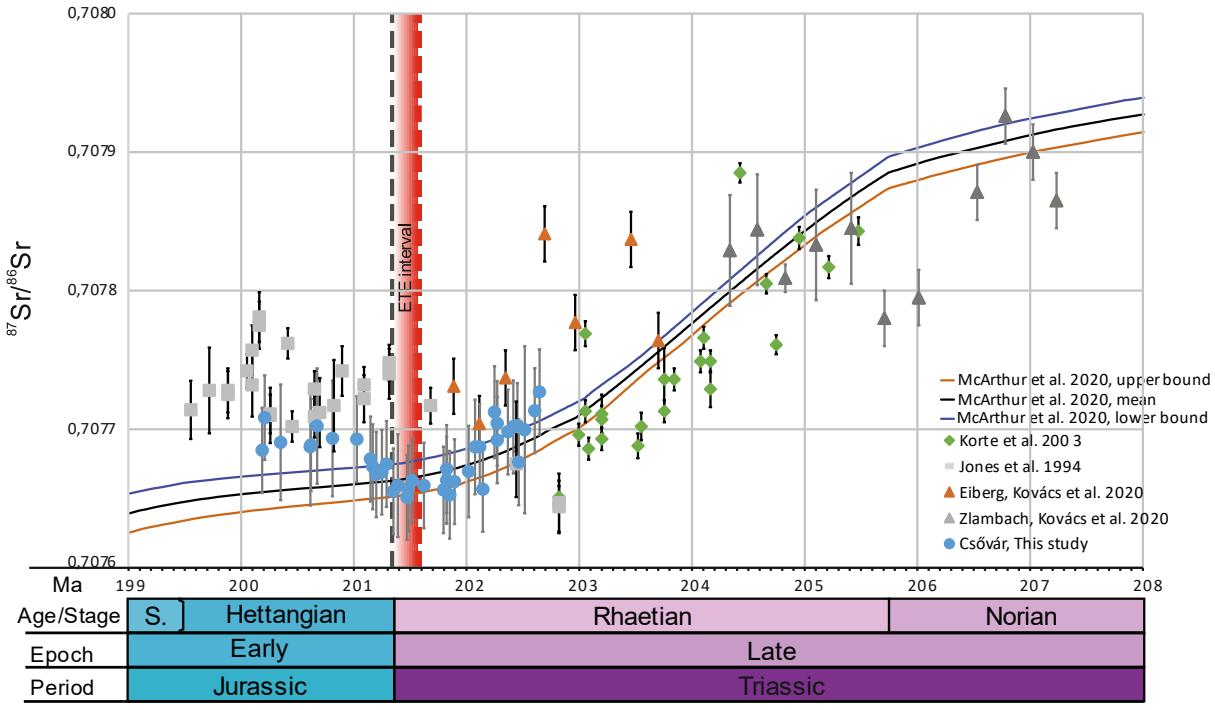

Fig. 23. Compilation of selected $^{87}Sr/^{86}Sr$ data for the TJB interval with LOESS fit (f=0.5, 95% confidence intervals) and the reference curve of McArthur et al. (2020). There is visible decoupling between the LOESS curve compared to the reference curve in the earliest Hettangian. Error bars in 2sd. Diamonds: brachiopods, squares: oysters, triangles: bulk carbonate (Kovács et al. 2020b), circles: bulk carbonate from Csővár. Red dotted line represents the I-NCIE at 201.564 Ma (Davies et al. 2017), black dotted line represents the Triassic-Jurassic boundary at 201.36 Ma (Hillebrandt et al. 2013). All data are recalculated to the Geologic Time Scale 2020 (Gradstein et al. 2020)

marine $^{87}Sr/^{86}Sr$ decrease, and causes uncertainty for SIS during the latest Rhaetian and the Hettangian (Fig. 24). The lack of reliable data in the critical time interval of the TJB limits the constraints on this slowdown, as it depends on the choice of fossil materials. The Csővár $^{87}Sr/^{86}Sr$ dataset fills the gap in the crucial interval and reveals a rise in the marine $^{87}Sr/^{86}Sr$ ratio after the TJB, instead of a decrease or a flattening of the curve. From the Sinemurian, the long gradual declining trend continues and terminates by a rebound to more radiogenic values in the earliest Toarcian after reaching a ratio close to 0.7070.

The injection of unradiogenic Sr into coeval seawater due to CAMP weathering is suggested by the Csővár $^{87}Sr/^{86}Sr$ ratios. However, the direct impact of CAMP on marine $^{87}Sr/^{86}Sr$ must have been overshadowed by more potent environmental changes resulting from CAMP emplacement and simultaneous changes in the Earth surface system. It is possible that enhanced hydrological cycling and increased weathering of more radiogenic continental rocks due to elevated CO_2 could have contributed to the delivery of relatively radiogenic Sr to the global ocean with higher $^{87}Sr/^{86}Sr$ ratios, resulting in a Hettangian plateau in seawater $^{87}Sr/^{86}Sr$. Overall, further studies are required to better understand the extent of CAMP's influence on the

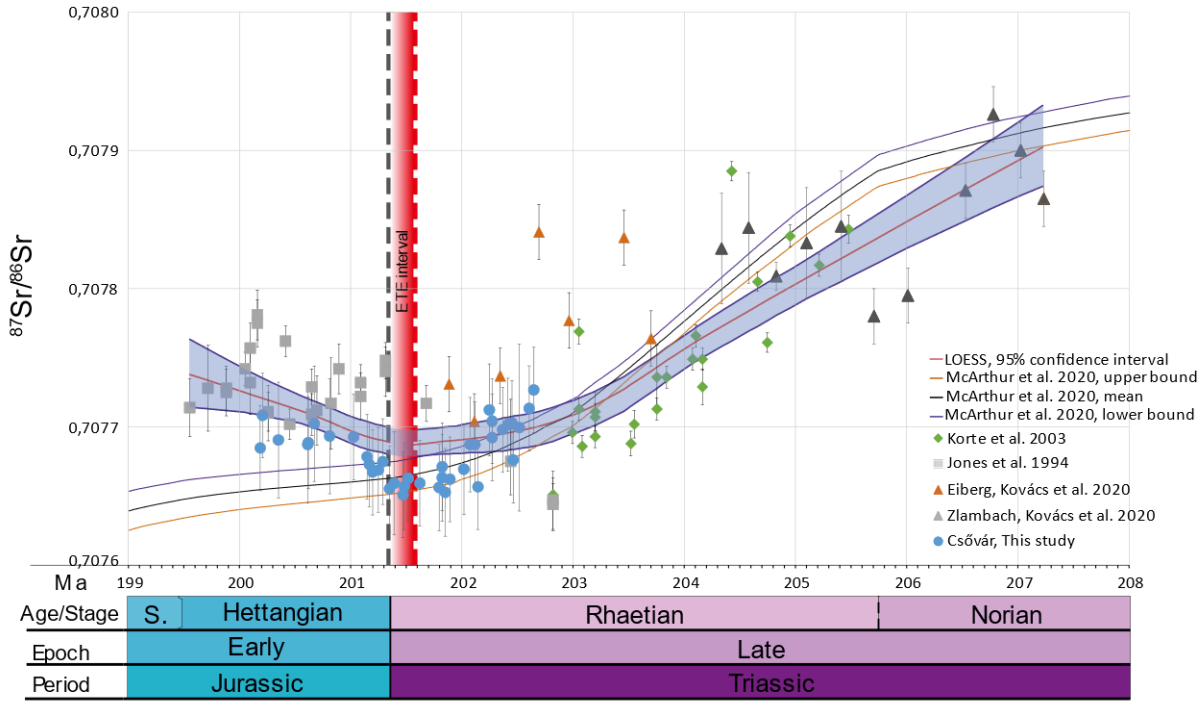

Fig. 24. Compilation of selected $^{87}Sr/^{86}Sr$ data for the TJB interval with the reference curve of McArthur et al. (2020). There is visible decoupling between the data from Csővár and Jones et al. (1994) compared to the reference curve. Error bars in 2sd. Diamonds: brachiopods, squares: oysters, triangles: bulk carbonate (Kovács et al. 2020b), circles: bulk carbonate from Csővár. Red dotted line represents the I-NCIE at 201.564 Ma (Davies et al. 2017), black dotted line represents the Triassic-Jurassic boundary at 201.36 Ma (Hillebrandt et al. 2013). All data are recalculated to the Geologic Time Scale 2020 (Gradstein et al. 2020).

marine $^{87}Sr/^{86}Sr$ ratio and its corresponding feedback mechanism. The new $^{87}Sr/^{86}Sr$ dataset fills the observational gap around the TJB and identifies the start of the $^{87}Sr/^{86}Sr$ increase at the base of the Jurassic. This agrees with the overall trend of Kovács et al. (2020b), it provides reliability to the data presented by Jones et al. (1994), however, the data does not confirm the high values reported by Callegaro et al. (2012) and the Kuhjoch section by Kovács et al. (2020b). Nonetheless, the Csővár $^{87}Sr/^{86}Sr$ data fills the gap in the global $^{87}Sr/^{86}Sr$ record, provides constraints to the SIS, crucial information, and opportunities in understanding the changes in the Earth system for the boundary interval.

6.6 Modeling Sr flux perturbations around the TJB

Strontium box modeling involves simulating the cycling of strontium within the Earth's oceans and can thus provide additional insight into interpreting the observational record. By incorporating knowledge of strontium isotopes, fluxes, and reservoirs, modeling allows the simulation of changes in seawater composition and therefore helps in identifying the underlying mechanisms that influenced the strontium cycle during the TJB interval. As a result, the Sr isotope system has been used as a tool to monitor variations in earth system processes. Here, a simple forward box model is used to estimate the impact of perturbations on the ocean Sr cycle that could explain the changes in seawater $^{87}Sr/^{86}Sr$ ratio observed during the TJB interval. Forward models of seawater $^{87}Sr/^{86}Sr$ changes during TJB interval are produced, resulting in estimates of the change in the continental weathering to hydrothermal input of Sr to the oceans. The model was used to understand the ocean Sr cycle by examining how continental weathering and hydrothermal inputs of Sr may have responded to extensive LIP volcanism. Here, the hydrothermal input is understood as the overall -derived Sr input and is not restricted to Sr input from MORB-related hydrothermal sources. The model is based on Yobo et al. (2021), where a coupled Sr mass and Sr-isotope mass balance approach was used. The model parameters are derived from modern values and are mantle adjusted for the end-Triassic based on the available constraints. The following Equation (1) was used to calculate changes in the inventory of oceanic Sr over time:

$$\frac{dN^{Sr}}{dt} = F_{riv} + F_H + F_{dia} - F_{ppt} \qquad (1)$$

Where N^{Sr} represents the number of moles of strontium present in the oceans, and the variables F_{riv}, F_H, F_{dia}, and F_{ppt} correspond to the fluxes of strontium from riverine sources (continental weathering), hydrothermal sources, diagenetic sources, and carbonate precipitation flux,

respectively. Changes in ocean $^{87}Sr/^{86}Sr$ over time were calculated using the following Equation (2):

$$\frac{dR_{SW}^{Sr}}{dt} = \frac{F_{riv}^{Sr}(R_{riv}^{Sr} - R_{SW}^{Sr}) + F_{H}^{Sr}(R_{H}^{Sr} - R_{SW}^{Sr}) + F_{dia}^{Sr}(R_{dia}^{Sr} - R_{SW}^{Sr})}{N_{Sr}} \quad (2)$$

Where R_{SW}^{Sr} represents the $^{87}Sr/^{86}Sr$ ratio of the ocean Sr reservoir, whereas R_{riv}^{Sr}, R_{H}^{Sr}, and R_{dia}^{Sr} are the $^{87}Sr/^{86}Sr$ ratios of the riverine, hydrothermal, and diagenetic Sr inputs, respectively.

Table 1. Strontium parameters used in the model. Strontium flux and isotopic estimates utilized in the box model adapted from Yobo et al. (2021) and references therein.

Symbol	Description	Modern Value	Model Value	Source
F_{riv}^{Sr}	Continental weathering flux	66.1 x 10^9 mol yr^{-1}	66.1 x 10^9 mol yr^{-1}	1
R_{riv}^{Sr}	Continental weathering isotopic composition	0.7104	0.7101	2
F_{HT}^{Sr}	Hydrothermal flux	8.4 x 10^9 mol yr^{-1}	14.1 x 10^9 mol yr^{-1}	1
R_{HT}^{Sr}	Hydrothermal isotopic composition	0.7035	0.7035	1
F_{dia}^{Sr}	Diagenetic flux	5.5 x 10^9 mol yr^{-1}	5.5 x 10^9 mol yr^{-1}	1
R_{dia}^{Sr}	Diagenetic isotopic composition	0.70849	0.70733	3
N^{Sr}	Amount of Sr in seawater	1.25 x 10^{17} mol	1.25 x 10^{17} mol	4

1. Peucker-Ehrenbrink et al. (2019)
2. Allègre et al. (2010)
3. Li & Elderfield (2013)
4. Palmer & Edmond (1989)

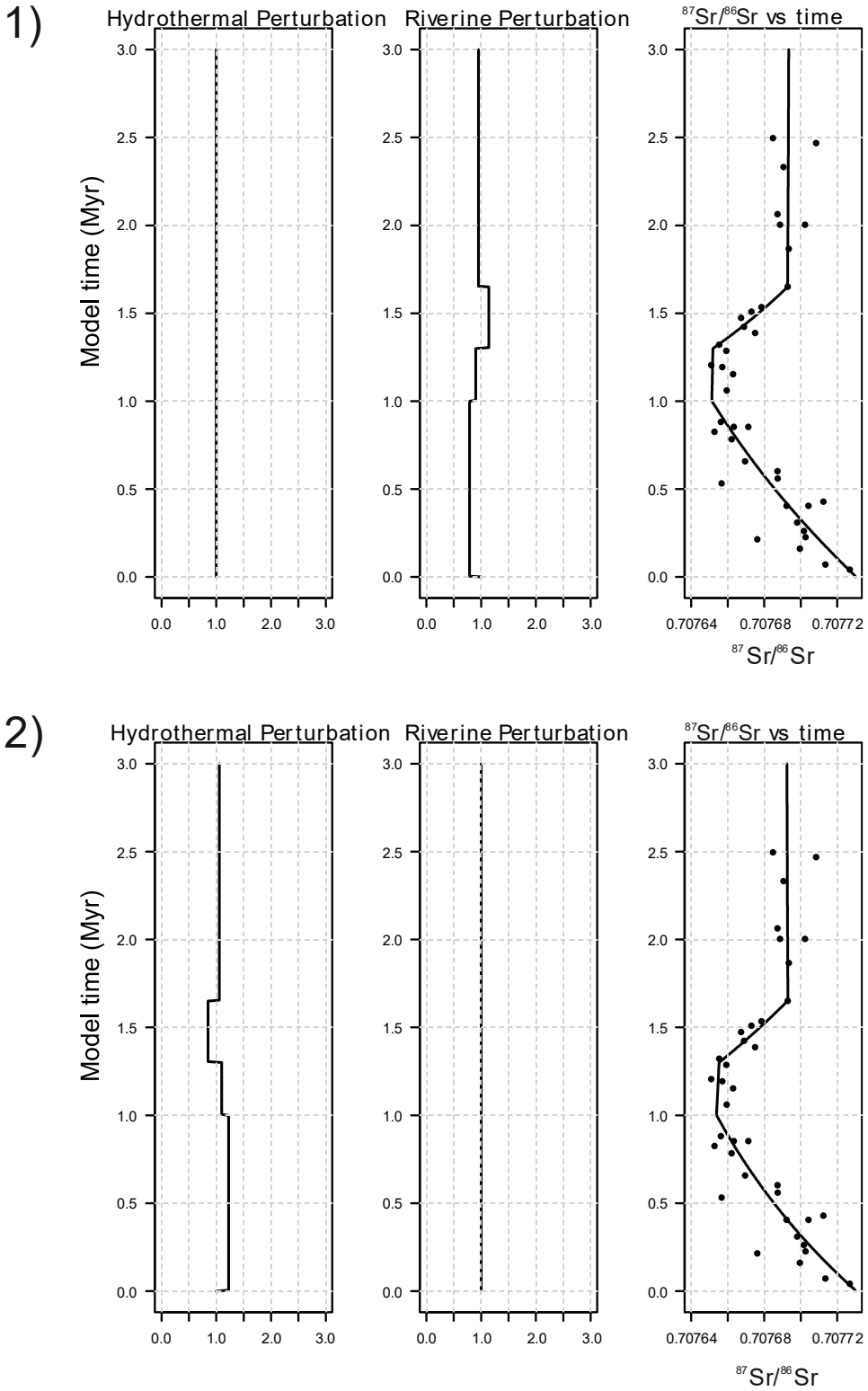

Fig. 25. Box model results of perturbations with either the hydrothermal or riverine Sr fluxes defined constant. The emplacement of CAMP and the contemporaneous carbon isotope excursion (I-NCIE) begin at 1 Myr model time. The perturbations are normalized to the assumed steady state at model time 0 Myr. 1) The hydrothermal flux is held constant. To reach the decreasing trend, the riverine flux is reduced to 0.79x, from 1 Myr it is set to 0.9x and to reach the increasing trend from 1.3 Myr, it is set to 1.14x. From 1.65 Myr it falls back to 0.95x till the end of the model. 2) The riverine flux is held constant. To achieve the decreasing trend, the hydrothermal flux is set to 1.225x, from 1 Myr it is set to 1.1x and to reach the increasing trend it is set to 0.85x between 1.3 Myr and 1.65 Myr, and back to 1.055 till the end of the model.

The Sr input fluxes and input $^{87}Sr/^{86}Sr$ ratios were obtained from present-day estimates (Table 1) or adjusted to end-Triassic values. The model was run for 3 million years, which is in broad agreement with the deposition time of the Csővár section (Vallner et al. 2023).

The initial Sr isotope mass balance is normalized to the contemporaneous seawater isotope value at the end-Triassic (~0.70773). Therefore, the initial $^{87}Sr/^{86}Sr$ ratio of all continental weathering sources of Sr (F_{riv}) was adjusted from the present-day ratio of 0.71040 down to 0.7086 to achieve a steady state $^{87}Sr/^{86}Sr$ ratio for end Triassic seawater of ~0.70773 based on values obtained from the base of the Csővár section. This adjustment does not reflect the true value of the continental weathering regime, it serves as an initial value that makes comparison available. Thus, the changes are compared to the steady-state conditions. The steady-state is an assumption needed for the modeling, even though no sedimentary evidence points toward a steady-state at this time interval. The primary input fluxes of Sr to the oceans, F_{riv} and F_H, drive changes in the ocean Sr cycle. Modifying one or both fluxes induce changes in the $^{87}Sr/^{86}Sr$ ratio of seawater, which gradually approaches the steady state $^{87}Sr/^{86}Sr$ ratio and slows down exponentially with time.

Determining a definitive solution for any alteration in the $^{87}Sr/^{86}Sr$ ratio of seawater poses a challenge. An elevation in the $^{87}Sr/^{86}Sr$ ratio of seawater can come from two factors: 1) increasing the Sr flux from continental weathering or 2) decreasing the Sr flux from mantle-derived sources (Fig. 25). Therefore, a change in the trend can be simulated by either increasing or decreasing one of the fluxes. Hence, there exist various ways to generate alterations in the long-term $^{87}Sr/^{86}Sr$ ratio, and these methods do not necessarily exclude one another. In order to accurately simulate past changes, incorporating geological constraints is essential for implementing the box model and achieving the most realistic scenario. This way, previous studies, models, and proxy data have to be considered when modeling the changes in Sr fluxes to the ocean. For instance, keeping the continental weathering flux constant is not in agreement with evidence for enhanced weathering for the TJB interval (Fig. 25 Scenario 2) (Shen et al. 2022b). Nor is keeping the mantle-derived Sr flux constant, as it contradicts the emplacement of large amounts of basalt from CAMP volcanism or the breakup of Pangea (Marzoli et al. 2018). The model scenarios, in which one of the fluxes remains constant, while the other is modified to correspond to the observed trend in the $^{87}Sr/^{86}Sr$ ratio in the Csővár data highlights the pattern of change required to reproduce the observed $^{87}Sr/^{86}Sr$ pattern of the Csővár section. It is important to note, these model scenarios reflect the change in Sr flux to the presumed initial state, they point out the stepwise nature of change, and the protracted rise in the $^{87}Sr/^{86}Sr$ ratio.

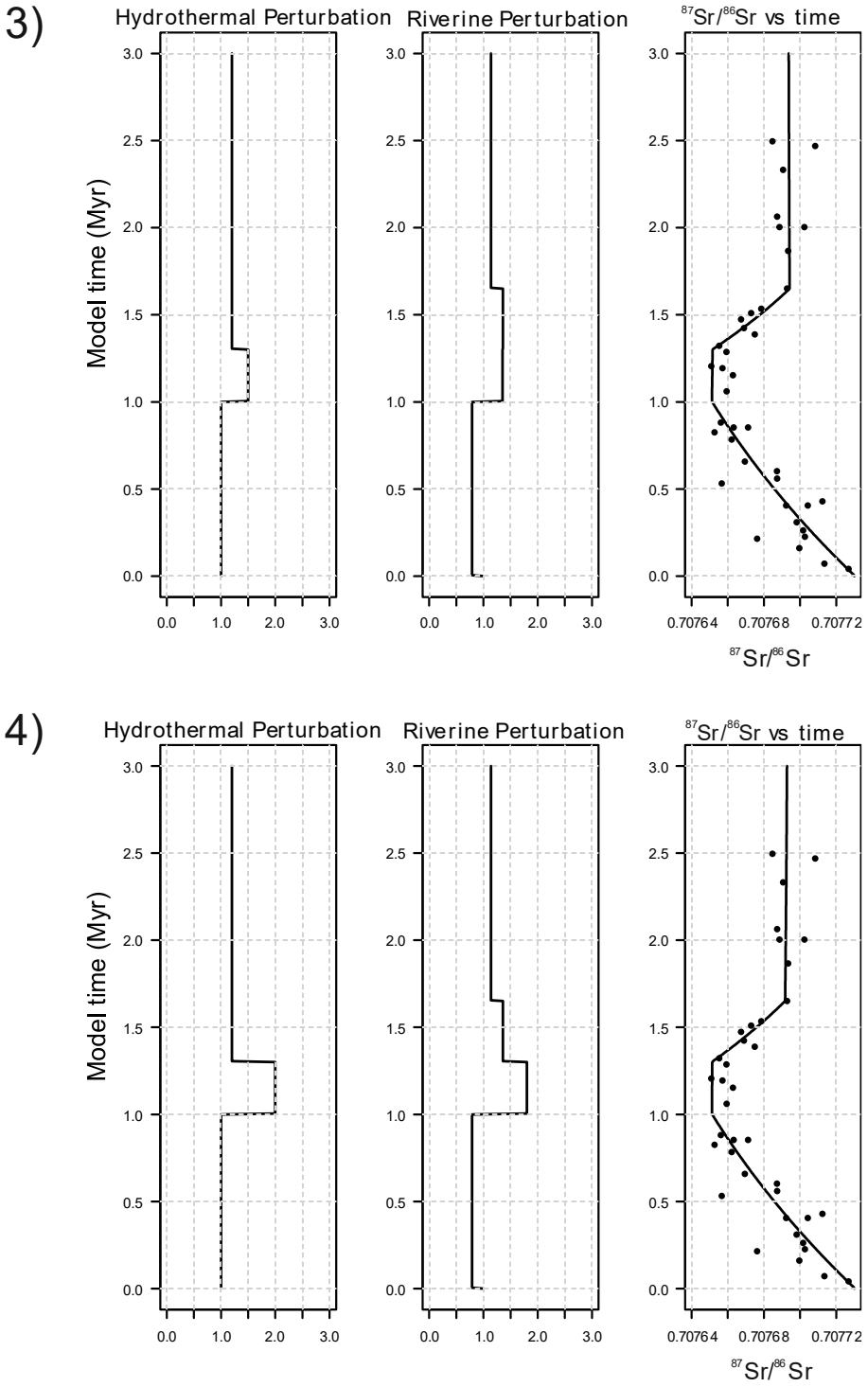

Fig. 26. Box model results of perturbations in both the hydrothermal and riverine Sr fluxes required to reproduce the change in seawater $^{87}Sr/^{86}Sr$ ratios during the Triassic-Jurassic boundary, based on the Csővár section. The emplacement of CAMP and the contemporaneous carbon isotope excursion (I-NCIE) begin at 1 Myr model time, with perturbations normalized to the assumed steady state at model time 0 Myr. Two scenarios are presented: 3) Hydrothermal flux increased by 1.5x with the onset of LIP eruptions. The hydrothermal flux falls back to 1.2x from 1.3 Myr model time but remains elevated throughout. To achieve the decreasing trend till 1 Myr, the riverine flux is reduced to 0.79x. The riverine flux in response to the onset of CAMP increases to 1.35x and stays escalated till 1.65 Myr, resulting in a radiogenic trend that is then reduced to 1.14x and stays elevated until the end of the model. 4) Hydrothermal flux increased by 2x with the onset of LIP eruptions. The hydrothermal perturbation falls back to 1.2x from 1.3 Myr. To balance the high hydrothermal flux, the riverine perturbation increases to 1.8x in response to CAMP and recovers stepwise to 1.36x at 1.3 Myr and 1.14x at 1.65 Myr. In both scenarios, the hydrothermal and weathering fluxes remain elevated, reflecting the ongoing volcanism of CAMP and opening of the Atlantic in the Early Jurassic.

To achieve more credible outcomes, two scenarios were run (Fig. 26), where the mantle-derived flux was set to 1.5x (Scenario 3) and 2x (Scenario 4) in response to CAMP volcanism, compared to the assumed steady state. The decreasing trend in the $^{87}Sr/^{86}Sr$ ratio is reproduced by reducing the weathering rates compared to the initial steady state. This is feasible, since multiple pieces of evidence point towards early hydrothermal activity in the Late Triassic (Callegaro et al. 2012, Kovács et al. 2020b). The trend flattens out in response to the onset of CAMP, which then turns into an increasing trend. The trough of the $^{87}Sr/^{86}Sr$ ratio lasts about ~300 kyr, which corresponds to the peak of CAMP volcanism. The trough then transitions to an upward trend towards more radiogenic values. The rise in $^{87}Sr/^{86}Sr$ ratios observed during the TJB interval may have been caused by an intensification in continental weathering or a rapid decrease in mantle-derived Sr flux. Several studies support the concept of intense weathering in response to the volcanism of CAMP (Cohen & Coe 2007, Shen et al. 2022b). The estimates of CO_2 related to the emplacement of CAMP support the rise in weathering intensity (Schaller et al. 2011). Nevertheless, the eruptions of large volume of equatorial CAMP basalts ($^{87}Sr/^{86}Sr$ ~ 0.7035-0.7050 (Merle et al. 2011, Heimdal et al. 2019), would have intensified volcanic weathering as well, leading to a shift in the $^{87}Sr/^{86}Sr$ ratio towards unradiogenic values. There is compelling geochemical evidence indicating that the erosion and weathering of the CAMP started shortly after its emplacement (Cohen & Coe 2002, 2007). Intense weathering of CAMP basalts, after the emplacement, aligns with the fluctuations in atmospheric CO_2 levels that responded to the cycles of CAMP eruption and weathering (Schaller et al. 2011). As a result, the trough in $^{87}Sr/^{86}Sr$ ratios was probably due to the counterbalancing of continental weathering in the first and peak phases of volcanic activity. The turn towards a radiogenic trend suggests the cessation of major unradiogenic input, and the increasing contribution from enhanced continental weathering. Here I propose a prolonged continental weathering scenario, which is supported by $^{87}Sr/^{86}Sr$ ratios from Csővár and the Sr flux modeling across the TJB interval.

The scenario 4) with a 2x increase in the mantle-derived Sr and the intensified continental weathering seems to be the most plausible outcome (Fig. 26 Scenario 4). Schaller et al. (2011) argued for the doubling of atmospheric pCO_2 in response to the first CAMP pulse, followed by a decrease to pre-eruptive concentrations over ~300 kyr. According to Schaller et al. (2012), after the first peak of pCO_2, there was a decline in pCO_2 to below background levels, which can be attributed to the prompt consumption of CO_2 resulting from an overall increase in continental weathering. This process was amplified by the rapid hydrolysis of the freshly erupted CAMP

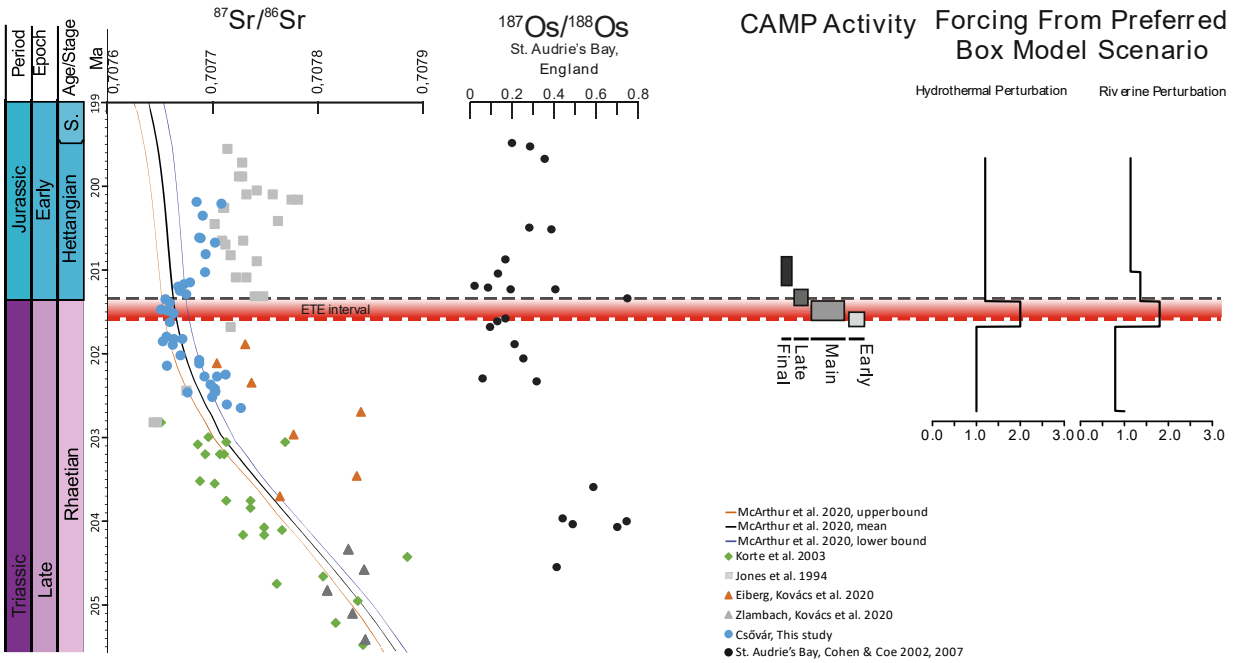

Fig. 27. Strontium-, and osmium isotopic changes across the Triassic-Jurassic boundary, together with distributions of CAMP rock ages, and the four main phases of CAMP activity (Heimdal et al. 2020). Box model results based on the scenario with the assumed 2x hydrothermal perturbation.

basalts. The findings are consistent with previous studies of CAMP activity, pCO_2 and $^{187}Os/^{188}Os$ changes (Cohen & Coe 2007, Kuroda et al. 2010, Schoene et al. 2010, Schaller et al. 2011) (Fig. 27). I propose that the $^{87}Sr/^{86}Sr$ ratio remained relatively low immediately following the initial CAMP eruptions. This suggests that a notable fraction of the weathering flux was composed of unradiogenic ^{86}Sr. As the highly weatherable CAMP basalts were largely consumed, the proportion of unradiogenic components progressively decreased, explaining the delayed increase in $^{87}Sr/^{86}Sr$.

6.7 Comparison with other LIP controlled events

Large Igneous Provinces (LIPs) have played a significant role in shaping the Earth's geological history and have been linked to various environmental and climatic changes. The question of whether LIP emplacements exert control over the $^{87}Sr/^{86}Sr$ ratios on a global scale has been the subject of debate for a long time.

One of the largest continental flood basalt volcanisms is tied to the emplacement of the Siberian Traps, which is considered to be the main driver of the most severe extinction in Earth history, the end-Permian extinction (Benton & Twitchett 2003). The $^{87}Sr/^{86}Sr$ record reached its Paleozoic minima in the Middle Permian (Capitanian), followed by a sharp increase towards

the Permo-Triassic boundary and into the Early Triassic (Korte & Ullmann 2018, McArthur et al. 2020). The time interval spanning the Permo-Triassic boundary is one with the most rapid increase in seawater $^{87}Sr/^{86}Sr$ in the Phanerozoic (McArthur et al. 2020). Studies have linked the steep increase of the $^{87}Sr/^{86}Sr$ ratio to the enhanced riverine flux in response to elevated atmospheric CO_2 (Martin & Macdougall 1995, Cohen & Coe 2007). However, the rise in the $^{87}Sr/^{86}Sr$ ratio begins significantly before (8–10 Ma) the Permo-Triassic boundary (McArthur 2008). Nevertheless, the accepted perspective is that the sharp rise reflects an increased flux of strontium with high $^{87}Sr/^{86}Sr$ ratios originating from continental weathering. (Ingram & DePaolo 2022) argued that the formation of the Ural Mountains, which was a significant continent–continent collision, could have resulted in increased continental weathering, however, it is unclear whether the timing is well constrained (Fig. 28). Korte & Ullmann (2018) argued that there is a temporal slowdown present in the Permian increase of the $^{87}Sr/^{86}Sr$ ratio at the Permo-Triassic boundary. It is short-lived, hence debated, but could represent the perturbation of the Earth system at this time interval. The change in the pace of the $^{87}Sr/^{86}Sr$ ratio increase could be attributed to a decrease in the $^{87}Sr/^{86}Sr$ ratio of continental runoff (Korte & Ullmann 2018), due to the weathering of basalts with low $^{87}Sr/^{86}Sr$ ratio. These processes, which drive the global continental runoff towards less radiogenic $^{87}Sr/^{86}Sr$ ratios, may align with the disruption of the seawater $^{87}Sr/^{86}Sr$ increase at the Permo-Triassic boundary, linked to the volcanism of the Siberian Traps. It has been proposed that the temporary disruption of the seawater $^{87}Sr/^{86}Sr$ rise predates the onset of volcanism (Korte & Kozur 2010). Thus, the direct link between volcanic forcing and the $^{87}Sr/^{86}Sr$ response remains ambiguous. In contrast, Song et al. (2015) reported a rapid increase in the $^{87}Sr/^{86}Sr$ ratios, which could be attributed to a substantial and swift increase (>2.8x) in the Sr flux from rivers, as a consequence of intensified continental weathering in response to the eruption of the Siberian Traps. In sum, the interpretations, and the drivers of the Sr system in response to the volcanism of the Siberian Traps remain controversial and require further validation.

Both the Siberian Traps and CAMP share the common characteristic of being emplaced on continents. This shared type of volcanism, suggests that the increased radiogenic Sr flux from continents, resulting from disturbances in the atmosphere and environment, has a more significant impact on the marine $^{87}Sr/^{86}Sr$ composition compared to the weathering of the newly exposed flood basalts (Kovács et al. 2020b). However, a difference between the two LIPs can be found in the paleogeographical positions of the provinces. While the Siberian Traps were located at higher latitudes, the CAMP was situated in the Equatorial belt, therefore, the

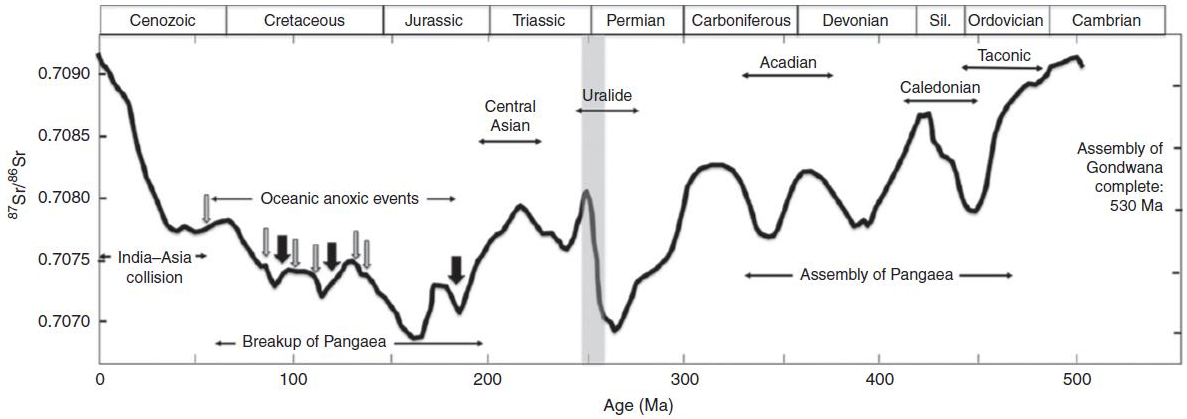

Fig. 28. Global seawater $^{87}Sr/^{86}Sr$ ratios through the Phanerozoic with major orogenic events. Black arrows show the main OAEs (Ingram & DePaolo 2022).

weathering of freshly erupted basalts may have had a stronger influence on the global $^{87}Sr/^{86}Sr$ curve. Nonetheless, in the case of CAMP, the continental weathering quickly overshadowed the unradiogenic trend and resulted in $^{87}Sr/^{86}Sr$ ratio increase in the Hettangian.

It seems as if LIP emplacements linked to Cretaceous Oceanic Anoxic Events (OAEs) have a stronger influence on the global $^{87}Sr/^{86}Sr$ ratios (Fig. 28) (Jones & Jenkyns 2001, Ingram & DePaolo 2022). In the Cretaceous, the combination of intensified volcanic eruption rates and a lack of continent–continent collisions contributed to substantially elevated atmospheric carbon dioxide levels and temperatures. Consequently, the reduced thermal gradients between the poles and equator resulted in weakened ocean circulation. These environmental conditions are believed to have triggered distinct intervals characterized by severe oxygen depletion in seawater, commonly referred to as OAEs, which are usually represented by the occurrence of black shales (Jenkyns 2010). Most of these events are associated with eruptions of LIPs. In the Cretaceous, major OAEs are marked by negative $^{87}Sr/^{86}Sr$ excursions. The observed declines in the $^{87}Sr/^{86}Sr$ ratios during these OAEs could have been caused by the increase in marine volcanism and hydrothermal activity. In the case of the Early Aptian OAE (OAE 1a; Selli Event) and the Cenomanian-Turonian OAE (OAE 2; Bonarelli Event), it is most likely that negative excursions in $^{87}Sr/^{86}Sr$ were driven by an increase in marine volcanism (Jones & Jenkyns 2001). The onset of the decline in $^{87}Sr/^{86}Sr$ values corresponds closely with the carbon isotope anomaly associated with the Selli event. In-depth profiles of $^{187}Os/^{188}Os$ reveal a distinct pulse of radiogenic osmium entering the oceans, causing an interruption in the downward trend of values. These are interpreted as a result of the submarine volcanic eruption accompanied by hydrothermal activity associated with the emplacement of a large oceanic plateau, the Ontong Java Plateau (Tejada et al. 2009, Jenkyns 2010). As for the Cenomanian-Turonian OAE, a

correlation between the event and the initiation of the $^{87}Sr/^{86}Sr$ ratio decline is present, indicating a potential rise in the mantle-derived strontium flux from hydrothermal sources. The OAE 2 has also been associated with submarine LIP volcanism. However, there is a relatively quick and sharp rise in the $^{87}Sr/^{86}Sr$ ratio coinciding with the onset of the positive carbon excursion, indicating the increase of the continental weathering flux as a reaction to elevated atmospheric CO_2 (Jenkyns 2010). The increase in the flux of continental weathering is not as significant as estimates had indicated, which implies that hydrothermal fluxes may have exceeded the impact of continental weathering on the $^{87}Sr/^{86}Sr$ ratio (Yobo et al. 2021).

Overall, LIP associated global events are not all alike in their geochemical response. The continental eruption of the Siberian Traps caused either a plateau in the sharp Permian $^{87}Sr/^{86}Sr$ ratio increase or further enhanced the radiogenic flux (Korte & Kozur 2010, Song et al. 2015). In the Cretaceous, the negative strontium isotope excursions indicate that submarine volcanism played a significant role in the occurrence of oceanic anoxic events. The major OAEs exhibit a brief radiogenic $^{87}Sr/^{86}Sr$ ratio trend coinciding with the onset of the representative carbon isotope excursions, which then turn into extensive negative excursions. The continental emplacement of CAMP slows down the decreasing $^{87}Sr/^{86}Sr$ trend of the Late Triassic, which even turns into an increasing trend in the Hettangian. This is a result of the prolonged weathering of the continental crust, in response to the mass amount of atmospheric CO_2 released from CAMP.

The changes in the global $^{87}Sr/^{86}Sr$ ratio associated with LIP controlled events are the result of complex processes, with each case exhibiting unique characteristics. By examining three LIP-related events, it becomes apparent that there are distinctions between the effects of continental and submarine emplacement on the $^{87}Sr/^{86}Sr$ ratio. When LIPs are emplaced on continental landmasses, the intensity of weathering experienced by freshly erupted basalts plays a more significant role in influencing the $^{87}Sr/^{86}Sr$ ratio, if the LIP was emplaced at lower latitudes. However, it is important to note that these factors are further complicated by ongoing changes in the background of the system, like climate change or orogenesis. These dynamic processes can influence the weathering rates, erosion patterns, and sediment transport, all of which can affect the isotopic composition of strontium (Sr) in the global system. Therefore, a case-by-case approach is needed for understanding the specific factors at play in each LIP event and their unique influence on the global $^{87}Sr/^{86}Sr$ ratio.

7 Conclusions and summary

Strontium isotope analyses of sedimentary bulk carbonates ($^{87}Sr/^{86}Sr$ ratios) in the biostratigraphically and chemostratigraphically well-constrained continuous marine Csővár section were undertaken. This method can be reliably used to interpret large-scale environmental changes at the Triassic-Jurassic boundary. The isotopic composition of strontium in seawater provides valuable information about the balance between continental weathering and mantle fluxes in the Earth system. This study aimed to obtain and present the first high-resolution $^{87}Sr/^{86}Sr$ ratios across the TJB interval while resolving uncertainties about the timing and magnitude of change in the mantle-derived-, and continental weathering fluxes of Sr to the oceans during the TJB. Hence, providing insights into the End-Triassic Extinction and gaining a deeper understanding of the causes and consequences and the potential feedback mechanisms connected to this event. The new $\delta^{13}C_{carb}$ data show major negative isotope anomalies, which can be used for global correlations, and support the previously published carbon isotope trends for the Csővár section. Based on 52 well-preserved samples within a 2.5-million-year duration, the $^{87}Sr/^{86}Sr$ ratio displays modest but important variations, which, for the first time, show a continuous decline till the boundary, and an increase in the $^{87}Sr/^{86}Sr$ ratios right after. The short-term fluctuations in the $^{87}Sr/^{86}Sr$ ratio are attributed to local weathering changes or alteration of the original $^{87}Sr/^{86}Sr$ compositions. The rise in the $^{87}Sr/^{86}Sr$ ratios is associated with the continental supply of ^{87}Sr via intensified weathering triggered by elevated atmospheric CO_2 levels. For a broader perspective, Alpine sections were correlated with the Csővár section using cyclostratigraphy and chemostratigraphy. The astronomical tuning made it possible to interpret the $^{87}Sr/^{86}Sr$ ratios of the sections on a numerical scale and compare them with the $^{87}Sr/^{86}Sr$ ratios of previous studies. The data from Csővár, together with formerly published data, displays a long-term decreasing trend from the Late Norian until the Triassic-Jurassic boundary, where it turns into an increasing trend in the Hettangian. The Csővár data also reveals flattening and a delayed rise in the marine $^{87}Sr/^{86}Sr$ ratio, suggesting the injection of unradiogenic Sr into coeval seawater due to CAMP emplacement and weathering, which caused a prolonged continental weathering response. A simple forward box model was used to estimate the impact of perturbations on the ocean Sr cycle during the TJB interval. The model showed that changes in the continental weathering to hydrothermal input of Sr to the oceans could explain the observed changes in seawater $^{87}Sr/^{86}Sr$ ratio. The model supported that the decreasing trend in the $^{87}Sr/^{86}Sr$ ratio during the TJB interval was reached by the early hydrothermal activity in the Late Triassic. The prolonged rise in $^{87}Sr/^{86}Sr$ ratios observed after

the TJB interval may have been caused by an escalation in continental weathering or a rapid decrease in mantle-derived Sr flux. The emplacement and weathering of freshly erupted basalts could have withheld the radiogenic trend, which turned to an increasing trend after the peak phases of CAMP and after large volumes of CAMP had been eroded. The subsequent shift towards a radiogenic trend indicates a decrease in unradiogenic input and an increase in continental weathering. The $^{87}Sr/^{86}Sr$ ratios from Csővár and Sr flux modeling during the TJB interval point towards a scenario of extended continental weathering. To verify this scenario, it is necessary to conduct more analyses of the strontium record in other TJB marine carbonate successions across the globe with a similar level of detail. The Csővár $^{87}Sr/^{86}Sr$ dataset provides important insights into the events associated with the TJB and contributes to a deeper understanding of the processes that led to changes in the global climate and environment at the time.

8 Összefoglalás

A triász-jura határ (TJB; 201,3 Ma) az élet fejlődéstörténetének egyik legsúlyosabb válságával, a triász végi kihalással (ETE) hozható összefüggésbe, amely egy, az "Öt Nagy" kihalási esemény közül. Elsődleges oka a Közép-Atlanti Magmás Provincia (CAMP) bazaltjainak magmatizmusához köthető. A vulkanizmus, a szénizotóp-anomáliák és a kontinentális mállás közötti összefüggések továbbra is nagyrészt következtetéseken alapulnak, és további igazolást igényelnek. A Csővár melletti vár-hegyi szelvény a triász-jura határ egyik legjobban feltárt és sokoldalúan tanulmányozott szelvénye. A szelvényt a Dachsteini-platform külső pereméhez közel található intraplatform medencében folytonosan ülepedő Csővári Mészkő Formáció építi fel. A diplomamunkám során a csővári szelvény karbonátján végeztem stronciumizotóp méréseket ($^{87}Sr/^{86}Sr$). Ez a módszer jól alkalmazható a triász-jura határ nagyléptékű környezet- és klímaváltozásainak értelmezésére. Az egykori tengervíz stronciumizotóp-összetétele értékes információt nyújt a kontinentális mállásból és a földköpenyből származó fluxus egyensúlyáról. A Sr izotóprendszer a kontinentális kéreg mállásából származó és folyóvízi beszállítás révén a tengerbe jutó ^{87}Sr, és a köpenyeredetű, főként az óceánközépi hátsági vulkanizmusból származó ^{86}Sr fluxusának arányát rögzíti. A diplomamunkám célja az első, nagy felbontású $^{87}Sr/^{86}Sr$ adatsor elkészítése volt a triász-jura határán. Ezáltal betekintést nyerhetünk a triász végén bekövetkezett kihalási eseménybe, mélyebben megérthetjük annak környezeti okait, következményeit és az eseményhez kapcsolódó visszacsatolási mechanizmusokat. További célom volt, hogy a TJB intervallumban hiányos globális Sr-izotóp referenciagörbét megbízhatóbbá tegyem új adatokkal, lehetőséget teremtve a rétegtani korrelációra. Az új $\delta^{13}C_{carb}$ adatok kimutatták az eseményre jellemző negatív szénizotóp-anomáliát, amelyet globális korrelációhoz használtam, és alátámasztotta a Csővár szelvényből korábban publikált szénizotóp-adatokat. Összesen 52 jól megőrződött minta alapján, a 2,5 millió éves időtartamot felölelő $^{87}Sr/^{86}Sr$ görbe mérsékelt, de fontos változásokat mutat. Első alkalommal figyelhető meg a $^{87}Sr/^{86}Sr$ arány folyamatos csökkenése a határig, majd növekedése közvetlenül utána. A rövid távú $^{87}Sr/^{86}Sr$ ingadozásokat a mállás lokális változásai okozhatták. A $^{87}Sr/^{86}Sr$ arány növekedése a kontinentális Sr többletét jelzi, amelyet a magas légköri CO_2 szint által kiváltott fokozott mállási intenzitás okozott. A tágabb értelmezés érdekében, ciklussztratigráfia és kemosztratigráfia segítségével, a csővári szelvényt alpi szelvényekkel korreláltam. A ciklussztratigráfia lehetővé tette az alpi szelvények $^{87}Sr/^{86}Sr$ arányainak tanulmányozását numerikus skálán, illetve összevetésüket korábbi tanulmányokkal. A csővári adatok ezekkel a korábban publikált adatokkal együtt, hosszú távú csökkenő trendet mutatnak a késő noritól a

triász-jura határig, ami a hettangiban növekvő tendenciába fordul. A csővári adatok kimutatták a $^{87}Sr/^{86}Sr$ görbe ellaposodását és az izotóparány késleltetett növekedését, ami köpenyeredetű ^{86}Sr injektálására utal az egykori tengervízbe. Ez a CAMP vulkanizmusához és a friss bazaltok mállásához köthető, amit az elhúzódó kontinentális mállás gyorsan ellensúlyozott. Egy egyszerű box modellt használtam a Sr ciklus fluxusaiban bekövetkező nagyságrendi változások becslésére a TJB időintervallum alatt. A modell szerint a csővári $^{87}Sr/^{86}Sr$ arány változásai a kontinentális mállás és a köpenyeredetű Sr-bemenet változásaiból számíthatók. A modell alátámasztotta, hogy a késő triász csökkenő $^{87}Sr/^{86}Sr$ arány trendje a megnövekedett hidrotermás tevékenységgel értelmezhető. A TJB intervallum után megfigyelt $^{87}Sr/^{86}Sr$ arányok növekedése a kontinentális mállás fokozódásával vagy a földköpenyből származó Sr fluxus gyors csökkenésével magyarázható. Az egyenlítői övben frissen kiömlött nagy mennyiségű bazaltok mállása visszatarthatta a radiogén trendet, ami a CAMP fő fázisát követően növekvő tendenciávába váltott. Az ezt követő radiogén trend a köpenyeredetű fluxus csökkenését és a kontinentális mállás fokozódását jelzi. A csővári szelvény $^{87}Sr/^{86}Sr$ adatai és a Sr fluxus modellezés egy elhúzódó kontinentális mállási szcenárióra utalnak. Ennek alátámasztására azonban további részletes stroncium mérésekre van szükség más tengeri TJB szelvényekből.

9 Acknowledgments

I would like to express my sincere gratitude to all those who have contributed to the completion of this thesis. Firstly, I extend my deepest appreciation to my supervisor, Dr. József Pálfy, for proposing such an intriguing topic and for his invaluable guidance, support, and unwavering belief in me throughout the process of preparing this thesis. I am grateful for his constructive advice and for always being available to address my inquiries regarding the content and structure of the thesis.

I would like to extend my gratitude to Joachim Katchinoff for his invaluable efforts in collecting and preparing the samples for measurement at Yale. His dedication and thorough work have been instrumental in ensuring the quality and reliability of the data used in this study.

I am deeply grateful to Dr. László Palcsu and Anikó Horváth for their remarkable contributions to developing the analytical background of the strontium isotope measurements at ATOMKI.

I would like to thank Zsolt Vallner for conducting the cyclostratigraphic analyses, which have been essential to the development of this thesis. Without his significant contributions, this thesis would not have reached its current form.

I would also like to thank Anna Somlyay for her valuable consultation regarding the modeling. I would like to express my gratitude to Lucien Nana Yobo for generously sharing the R code from their study, which served as the foundation for developing the model in my research.

I would like to express my appreciation to Emma Blanka Kovács, Zsófia Kovács, and Tamás Müller who greatly influenced the development of this thesis.

I would also like to acknowledge my family, especially Judit for her continuous encouragement. Furthermore, I would like to extend special thanks to Eszter for her heartfelt appreciation and willingness to lend an ear to all my monologues.

10 References

Allègre, C. J., Louvat, P., Gaillardet, J., Meynadier, L., Rad, S. & Capmas, F. 2010: The fundamental role of island arc weathering in the oceanic Sr isotope budget. — *Earth and Planetary Science Letters* **292/1-2,** 51-56.

Andersen, M., Romaniello, S., Vance, D., Little, S., Herdman, R. & Lyons, T. 2014: A modern framework for the interpretation of $^{238}U/^{235}U$ in studies of ancient ocean redox. — *Earth and Planetary Science Letters* **400,** 184-194.

Armstrong, H., Pearson, D. & Griselin, M. 2001: Thermal effects on rare earth element and strontium isotope chemistry in single conodont elements. — *Geochimica et Cosmochimica Acta* **65/3,** 435-441.

Bailey, T., Mcarthur, J., Prince, H. & Thirlwall, M. 2000: Dissolution methods for strontium isotope stratigraphy: whole rock analysis. — *Chemical Geology* **167/3-4,** 313-319.

Beerling, D. & Berner, R. 2002: Biogeochemical constraints on the Triassic-Jurassic boundary carbon cycle event. — *Global Biogeochemical Cycles* **16/3,** 10-1-10-13.

Benkő, K. & Fodor, L. 2002: Csővár környékének szerkezetföldtana (Structural geology near Csővár, Hungary). — *Földt. Közlöny* **132,** 223-246.

Benton, M. J. 1995: Diversification and extinction in the history of life. — *Science* **268/5207,** 52-58.

Benton, M. J. & Twitchett, R. J. 2003: How to kill (almost) all life: the end-Permian extinction event. — *Trends in Ecology & Evolution* **18/7,** 358-365.

Blackburn, T. J., Olsen, P. E., Bowring, S. A., Mclean, N. M., Kent, D. V., Puffer, J., Mchone, G., Rasbury, E. T. & Et-Touhami, M. 2013: Zircon U-Pb geochronology links the end-Triassic extinction with the Central Atlantic Magmatic Province. — *Science* **340/6135,** 941-945.

Bottrell, S. H. & Newton, R. J. 2006: Reconstruction of changes in global sulfur cycling from marine sulfate isotopes. — *Earth-Science Reviews* **75/1-4,** 59-83.

Brand, U. & Veizer, J. 1981: Chemical diagenesis of a multicomponent carbonate system; 2, Stable isotopes. — *Journal of Sedimentary Research* **51/3,** 987-997.

Brand, U., Azmy, K., Tazawa, J.-I., Sano, H. & Buhl, D. 2010: Hydrothermal diagenesis of Paleozoic seamount carbonate components. — *Chemical Geology* **278/3-4,** 173-185.

Burke, W., Denison, R., Hetherington, E., Koepnick, R., Nelson, H. & Otto, J. 1982: Variation of seawater $^{87}Sr/^{86}Sr$ throughout Phanerozoic time. — *Geology* **10/10,** 516-519.

Callegaro, S., Rigo, M., Chiaradia, M. & Marzoli, A. 2012: Latest Triassic marine Sr isotopic variations, possible causes and implications. — *Terra Nova* **24/2,** 130-135.

Chen, X., Zhou, Y. & Shields, G. A. 2022: Progress towards an improved Precambrian seawater $^{87}Sr/^{86}Sr$ curve. — *Earth-Science Reviews* **224,** 103869.

Cohen, A. S. & Coe, A. L. 2002: New geochemical evidence for the onset of volcanism in the Central Atlantic magmatic province and environmental change at the Triassic-Jurassic boundary. — *Geology* **30/3,** 267-270.

Cohen, A. S. & Coe, A. L. 2007: The impact of the Central Atlantic Magmatic Province on climate and on the Sr-and Os-isotope evolution of seawater. — *Palaeogeography, Palaeoclimatology, Palaeoecology* **244/1-4,** 374-390.

Corso, J. D., Marzoli, A., Tateo, F., Jenkyns, H. C., Bertrand, H., Youbi, N., Mahmoudi, A., Font, E., Buratti, N. & Cirilli, S. 2014: The dawn of CAMP volcanism and its bearing on the end-Triassic carbon cycle disruption. — *Journal of the Geological Society* **171/2,** 153-164.

Davies, J., Marzoli, A., Bertrand, H., Youbi, N., Ernesto, M. & Schaltegger, U. 2017: End-Triassic mass extinction started by intrusive CAMP activity. — *Nature communications* **8/1,** 15596.

De Laeter, J. R., Böhlke, J. K., De Bievre, P., Hidaka, H., Peiser, H., Rosman, K. & Taylor, P. 2003: Atomic weights of the elements. Review 2000 (IUPAC Technical Report). — *Pure and applied chemistry* **75/6,** 683-800.

Deenen, M. H., Ruhl, M., Bonis, N. R., Krijgsman, W., Kuerschner, W. M., Reitsma, M. & Van Bergen, M. 2010: A new chronology for the end-Triassic mass extinction. — *Earth and Planetary Science Letters* **291/1-4,** 113-125.

Du, Y., Chiari, M., Karádi, V., Nicora, A., Onoue, T., Pálfy, J., Roghi, G., Tomimatsu, Y. & Rigo, M. 2020: The asynchronous disappearance of conodonts: New constraints from Triassic-Jurassic boundary sections in the Tethys and Panthalassa. — *Earth-Science Reviews* **203,** 103176.

Ebneth, S., Diener, A., Buhl, D. & Veizer, J. 1997: Strontium isotope systematics of conodonts: middle Devonian, Eifel Mountains, Germany. — *Palaeogeography, Palaeoclimatology, Palaeoecology* **132/1-4,** 79-96.

Edwards, C. T., Saltzman, M. R., Leslie, S. A., Bergström, S. M., Sedlacek, A. R., Howard, A., Bauer, J. A., Sweet, W. C. & Young, S. A. 2015: Strontium isotope ($^{87}Sr/^{86}Sr$) stratigraphy of Ordovician bulk carbonate: Implications for preservation of primary seawater values. — *Bulletin* **127/9-10,** 1275-1289.

Elderfield, H. 1986: Strontium isotope stratigraphy. — *Palaeogeography, palaeoclimatology, palaeoecology* **57/1,** 71-90.

Fowell, S. & Olsen, P. 1993: Time calibration of Triassic/Jurassic microfloral turnover, eastern North America. — *Tectonophysics* **222/3-4,** 361-369.

Fujisaki, W., Matsui, Y., Asanuma, H., Sawaki, Y., Suzuki, K. & Maruyama, S. 2018: Global perturbations of carbon cycle during the Triassic–Jurassic transition recorded in the mid-Panthalassa. — *Earth and Planetary Science Letters* **500,** 105-116.

Galbrun, B., Boulila, S., Krystyn, L., Richoz, S., Gardin, S., Bartolini, A. & Maslo, M. 2020: " Short" or" long" Rhaetian? Astronomical calibration of Austrian key sections. — *Global and Planetary Change* **192,** 103253.

Götz, A., Ruckwied, K., Pálfy, J. & Haas, J. 2009: Palynological evidence of synchronous changes within the terrestrial and marine realm at the Triassic/Jurassic boundary (Csővár section, Hungary). — *Review of Palaeobotany and Palynology* **156/3-4,** 401-409.

Gradstein, F. M., Ogg, J. G., Schmitz, M. D. & Ogg, G. M. 2020: *Geologic time scale 2020*. — . Elsevier.

Grasby, S. E., Them Ii, T. R., Chen, Z., Yin, R. & Ardakani, O. H. 2019: Mercury as a proxy for volcanic emissions in the geologic record. — *Earth-Science Reviews* **196,** 102880.

Haas, J. 2002: Origin and evolution of Late Triassic backplatform and intraplatform basins in the Transdanubian Range, Hungary. — *Geologica Carpathica-Bratislava*- **53/3,** 159-178.

Haas, J. & Tardy-Filácz, E. 2004: Facies changes in the Triassic–Jurassic boundary interval in an intraplatform basin succession at Csővár (Transdanubian Range, Hungary). — *Sedimentary Geology* **168/1-2,** 19-48.

Haas, J., Götz, A. E. & Pálfy, J. 2010: Late Triassic to Early Jurassic palaeogeography and eustatic history in the NW Tethyan realm: New insights from sedimentary and organic facies of the Csővár Basin (Hungary). — *Palaeogeography, Palaeoclimatology, Palaeoecology* **291/3-4,** 456-468.

Haas, J., Tardi-Filácz, E., Oravecz-Scheffer, A., Góczán, F. & Dosztály, L. 1997: Stratigraphy and sedimentology of an Upper Triassic toe-of-slope and basin succession at Csővár, North Hungary. — *Acta Geologica Hungarica* **40/2,** 111-177.

Haas, J., Jovanović, D., Görög, Á., Sudar, M. N., Józsa, S., Ozsvárt, P. & Pelikán, P. 2019: Upper Triassic–Middle Jurassic resedimented toe-of-slope and hemipelagic basin deposits in the Dinaridic Ophiolite Belt, Zlatar Mountain, SW Serbia. — *Facies* **65,** 1-29.

Hallam, A. 2002: How catastrophic was the end-Triassic mass extinction? — *Lethaia* **35/2,** 147-157.

Halverson, G. P., Dudás, F. Ö., Maloof, A. C. & Bowring, S. A. 2007: Evolution of the 87Sr/86Sr composition of Neoproterozoic seawater. — *Palaeogeography, Palaeoclimatology, Palaeoecology* **256/3-4,** 103-129.

He, T., Dal Corso, J., Newton, R. J., Wignall, P. B., Mills, B. J., Todaro, S., Di Stefano, P., Turner, E. C., Jamieson, R. A. & Randazzo, V. 2020: An enormous sulfur isotope excursion indicates marine anoxia during the end-Triassic mass extinction. — *Science Advances* **6/37,** eabb6704.

Heimdal, T. H., Jones, M. T. & Svensen, H. H. 2020: Thermogenic carbon release from the Central Atlantic magmatic province caused major end-Triassic carbon cycle perturbations. — *Proceedings of the National Academy of Sciences* **117/22,** 11968-11974.

Heimdal, T. H., Callegaro, S., Svensen, H. H., Jones, M. T., Pereira, E. & Planke, S. 2019: Evidence for magma–evaporite interactions during the emplacement of the Central Atlantic Magmatic Province (CAMP) in Brazil. — *Earth and Planetary Science Letters* **506,** 476-492.

Hesselbo, S. P., Robinson, S. A., Surlyk, F. & Piasecki, S. 2002: Terrestrial and marine extinction at the Triassic-Jurassic boundary synchronized with major carbon-cycle perturbation: A link to initiation of massive volcanism? — *Geology* **30/3,** 251-254.

Hillebrandt, A., Krystyn, L., Kürschner, W., Bonis, N., Ruhl, M., Richoz, S., Schobben, M., Urlichs, M., Bown, P. & Kment, K. 2013: The global stratotype sections and point (GSSP) for the base of the Jurassic System at Kuhjoch (Karwendel Mountains, Northern Calcareous Alps, Tyrol, Austria). — *Episodes* **36/3,** 162-198.

Hodell, D. A., Mead, G. A. & Mueller, P. A. 1990: Variation in the strontium isotopic composition of seawater (8 Ma to present): Implications for chemical weathering rates and dissolved fluxes to the oceans. — *Chemical Geology: Isotope Geoscience section* **80/4,** 291-307.

Howarth, R. J. & Mcarthur, J. M. 1997: Statistics for strontium isotope stratigraphy: a robust LOWESS fit to the marine Sr-isotope curve for 0 to 206 Ma, with look-up table for derivation of numeric age. — *The Journal of Geology* **105/4,** 441-456.

Ingram, B. L. & Depaolo, D. J. 2022: Sr Isotopes in Seawater: Stratigraphy, Paleo-tectonics, Paleoclimate, and Paleoceanography. — *Elements in Geochemical Tracers in Earth System Science.*

Jenkyns, H. C. 2010: Geochemistry of oceanic anoxic events. — *Geochemistry, Geophysics, Geosystems* **11/3**.

Jones, C. E. & Jenkyns, H. C. 2001: Seawater strontium isotopes, oceanic anoxic events, and seafloor hydrothermal activity in the Jurassic and Cretaceous. — *American Journal of Science* **301/2,** 112-149.

Jones, C. E., Jenkyns, H. C., Coe, A. L. & Stephen, H. P. 1994: Strontium isotopic variations in Jurassic and Cretaceous seawater. — *Geochimica et Cosmochimica Acta* **58/14,** 3061-3074.

Jost, A. B., Bachan, A., Van De Schootbrugge, B., Lau, K. V., Weaver, K. L., Maher, K. & Payne, J. L. 2017: Uranium isotope evidence for an expansion of marine anoxia during the end-T riassic extinction. — *Geochemistry, Geophysics, Geosystems* **18/8,** 3093-3108.

Kaiho, K., Tanaka, D., Richoz, S., Jones, D. S., Saito, R., Kameyama, D., Ikeda, M., Takahashi, S., Aftabuzzaman, M. & Fujibayashi, M. 2022: Volcanic temperature changes modulated volatile release and climate fluctuations at the end-Triassic mass extinction. — *Earth and Planetary Science Letters* **579,** 117364.

Karádi, V., Kozur, H. W. & Görög, Á. 2013: Stratigraphically important Lower Norian conodonts from the Cs} ovar borehole (Csv-1), Hungary--comparison with the conodont succession of the Norian GSSP candidate Pizzo Mondello (Sicily, Italy). — *The Triassic System* **61,** 284-295.

Karádi, V., Cau, A., Mazza, M. & Rigo, M. 2019: The last phase of conodont evolution during the Late Triassic: Integrating biostratigraphic and phylogenetic approaches. — *Palaeogeography, Palaeoclimatology, Palaeoecology* **549,** 109144.

Kiessling, W. & Simpson, C. 2011: On the potential for ocean acidification to be a general cause of ancient reef crises. — *Global Change Biology* **17/1,** 56-67.

Koepnick, R., Denison, R., Burke, W., Hetherington, E. & Dahl, D. 1990: Construction of the Triassic and Jurassic portion of the Phanerozoic curve of seawater $^{87}Sr/^{86}Sr$. — *Chemical Geology: Isotope Geoscience section* **80/4,** 327-349.

Korte, C. & Kozur, H. W. 2010: Carbon-isotope stratigraphy across the Permian–Triassic boundary: a review. — *Journal of Asian Earth Sciences* **39/4,** 215-235.

Korte, C. & Ullmann, C. V. 2018: Permian strontium isotope stratigraphy. — *Geological Society, London, Special Publications* **450/1,** 105-118.

Korte, C., Kozur, H. W., Bruckschen, P. & Veizer, J. 2003: Strontium isotope evolution of Late Permian and Triassic seawater. — *Geochimica et Cosmochimica Acta* **67/1,** 47-62.

Korte, C., Ruhl, M., Pálfy, J., Ullmann, C. V. & Hesselbo, S. P. 2018: Chemostratigraphy across the Triassic–Jurassic boundary. — *Chemostratigraphy across major chronological boundaries,* 183-210.

Kovács, E. B., Ruhl, M., Demény, A., Fórizs, I., Hegyi, I., Horváth-Kostka, Z. R., Móricz, F., Vallner, Z. & Pálfy, J. 2020a: Mercury anomalies and carbon isotope excursions in the western Tethyan Csővár section support the link between CAMP volcanism and the end-Triassic extinction. — *Global and Planetary Change* **194,** 103291.

Kovács, Z., Demangel, I., Richoz, S., Hippler, D., Baldermann, A. & Krystyn, L. 2020b: New constraints on the evolution of 87Sr/86Sr of seawater during the Upper Triassic. — *Global and Planetary Change* **192,** 103255.

Kozur, H. 1991: New Middle Carnian and Rhaetian conodonts from Hungary and the Alps. Stratigraphic importance and tectonic implications for the Buda Mountains and adjacent areas. — *Jahrbuch der geologischen Bundesanstalt* **134/2,** 271-297.

Kozur, H. 1993: First evidence of Liassic in the vicinity of Csövár (Hungary), and its Paleogeographic and Paleotectonic significance. — *Jahrbuch der Geologischen Bundesanstalt* **136/1,** 89-98.

Kuerschner, W. M., Bonis, N. R. & Krystyn, L. 2007: Carbon-isotope stratigraphy and palynostratigraphy of the Triassic–Jurassic transition in the Tiefengraben section—Northern Calcareous Alps (Austria). — *Palaeogeography, Palaeoclimatology, Palaeoecology* **244/1-4,** 257-280.

Kump, L. R. & Arthur, M. A. 1999: Interpreting carbon-isotope excursions: carbonates and organic matter. — *Chemical Geology* **161/1-3,** 181-198.

Kuroda, J., Hori, R. S., Suzuki, K., Gröcke, D. R. & Ohkouchi, N. 2010: Marine osmium isotope record across the Triassic-Jurassic boundary from a Pacific pelagic site. — *Geology* **38/12,** 1095-1098.

Larina, E., Bottjer, D. J., Corsetti, F. A., Thibodeau, A. M., Berelson, W. M., West, A. J. & Yager, J. A. 2021: Ecosystem change and carbon cycle perturbation preceded the end-Triassic mass extinction. — *Earth and Planetary Science Letters* **576,** 117180.

Li, D., Shields-Zhou, G. A., Ling, H.-F. & Thirlwall, M. 2011: Dissolution methods for strontium isotope stratigraphy: Guidelines for the use of bulk carbonate and phosphorite rocks. — *Chemical Geology* **290/3-4,** 133-144.

Li, G. & Elderfield, H. 2013: Evolution of carbon cycle over the past 100 million years. — *Geochimica et Cosmochimica Acta* **103,** 11-25.

Lindström, S., Van De Schootbrugge, B., Hansen, K. H., Pedersen, G. K., Alsen, P., Thibault, N., Dybkjær, K., Bjerrum, C. J. & Nielsen, L. H. 2017: A new correlation of Triassic–Jurassic boundary successions in NW Europe, Nevada and Peru, and the Central Atlantic Magmatic Province: a time-line for the end-Triassic mass extinction. — *Palaeogeography, Palaeoclimatology, Palaeoecology* **478,** 80-102.

Lindström, S., Sanei, H., Van De Schootbrugge, B., Pedersen, G. K., Lesher, C. E., Tegner, C., Heunisch, C., Dybkjær, K. & Outridge, P. M. 2019: Volcanic mercury and mutagenesis in land plants during the end-Triassic mass extinction. — *Science advances* **5/10,** eaaw4018.

Lindström, S., Callegaro, S., Davies, J., Tegner, C., Van De Schootbrugge, B., Pedersen, G. K., Youbi, N., Sanei, H. & Marzoli, A. 2021: Tracing volcanic emissions from the Central Atlantic Magmatic Province in the sedimentary record. — *Earth-Science Reviews* **212,** 103444.

Martin, E. & Macdougall, J. 1995: Sr and Nd isotopes at the prmian/triassic boundary: A record of climate change. — *Chemical Geology* **125/1-2,** 73-99.

Martin, E. & Scher, H. 2004: Preservation of seawater Sr and Nd isotopes in fossil fish teeth: bad news and good news. — *Earth and Planetary Science Letters* **220/1-2,** 25-39.

Marzoli, A., Renne, P. R., Piccirillo, E. M., Ernesto, M., Bellieni, G. & Min, A. D. 1999: Extensive 200-million-year-old continental flood basalts of the Central Atlantic Magmatic Province. — *Science* **284/5414,** 616-618.

Marzoli, A., Callegaro, S., Dal Corso, J., Davies, J. H., Chiaradia, M., Youbi, N., Bertrand, H., Reisberg, L., Merle, R. & Jourdan, F. 2018: The Central Atlantic magmatic province (CAMP): A review. — *The Late Triassic World: Earth in a time of transition,* 91-125.

Mcarthur, J. M. 1994: Recent trends in strontium isotope stratigraphy. — *Terra nova* **6/4,** 331-358.

Mcarthur, J. M. 2008: Comment on "The impact of the Central Atlantic Magmatic Province on climate and on the Sr-and Os-isotope evolution of seawater" by Cohen AS and Coe AL 2007, Palaeogeography, Palaeoclimatology, Palaeoecology 244, 374–390. — *Palaeogeography, Palaeoclimatology, Palaeoecology* **263/3-4,** 146-149.

Mcarthur, J. M. 2010: Strontium isotope stratigraphy

Mcarthur, J. M. & Howarth, R. J. 2004: Strontium isotope stratigraphy. — *Cambridge University Press*.

Mcarthur, J. M., Howarth, R. & Bailey, T. 2001: Strontium isotope stratigraphy: LOWESS version 3: best fit to the marine Sr-isotope curve for 0–509 Ma and accompanying look-up table for deriving numerical age. — *The Journal of Geology* **109/2,** 155-170.

Mcarthur, J. M., Howarth, R. & Shields, G. 2012: Strontium isotope stratigraphy. — *Geologic Time Scale 2012*. Elsevier, pp. 127–144.

Mcarthur, J. M., Howarth, R., Shields, G. & Zhou, Y. 2020: Strontium isotope stratigraphy. — *Geologic Time Scale 2020*. Elsevier, pp. 211-238.

Mcarthur, J. M., Janssen, N., Reboulet, S., Leng, M., Thirlwall, M. & Van De Schootbrugge, B. 2007a: Palaeotemperatures, polar ice-volume, and isotope stratigraphy (Mg/Ca, $\delta^{18}O$, $\delta^{13}C$, $^{87}Sr/^{86}Sr$): the early cretaceous (Berriasian, Valanginian, Hauterivian). — *Palaeogeography, Palaeoclimatology, Palaeoecology* **248/3-4,** 391-430.

Mcarthur, J. M., Doyle, P., Leng, M., Reeves, K., Williams, C., Garcia-Sanchez, R. & Howarth, R. 2007b: Testing palaeo-environmental proxies in Jurassic belemnites: Mg/Ca, Sr/Ca, Na/Ca, $\delta^{18}O$ and $\delta^{13}C$. — *Palaeogeography, Palaeoclimatology, Palaeoecology* **252/3-4,** 464-480.

Merle, R., Marzoli, A., Bertrand, H., Reisberg, L., Verati, C., Zimmermann, C., Chiaradia, M., Bellieni, G. & Ernesto, M. 2011: $^{40}Ar/^{39}Ar$ ages and Sr–Nd–Pb–Os geochemistry of CAMP tholeiites from Western Maranhão basin (NE Brazil). — *Lithos* **122/3-4,** 137-151.

Michalík, J., Lintnerová, O., Gaździcki, A. & Soták, J. 2007: Record of environmental changes in the Triassic–Jurassic boundary interval in the Zliechov Basin, Western Carpathians. — *Palaeogeography, Palaeoclimatology, Palaeoecology* **244/1-4,** 71-88.

Newton, R., Pevitt, E., Wignall, P. & Bottrell, S. 2004: Large shifts in the isotopic composition of seawater sulphate across the Permo–Triassic boundary in northern Italy. — *Earth and Planetary Science Letters* **218/3-4,** 331-345.

Olsen, P. E., Kent, D. V., Sues, H.-D., Koeberl, C., Huber, H., Montanari, A., Rainforth, E., Fowell, S., Szajna, M. J. & Hartline, B. W. 2002: Ascent of dinosaurs linked to an iridium anomaly at the Triassic-Jurassic boundary. — *Science* **296/5571,** 1305-1307.

Onoue, T., Yamashita, K., Fukuda, C., Soda, K., Tomimatsu, Y., Abate, B. & Rigo, M. 2018: Sr isotope variations in the Upper Triassic succession at Pizzo Mondello, Sicily: Constraints on the timing of the Cimmerian Orogeny. — *Palaeogeography, Palaeoclimatology, Palaeoecology* **499,** 131-137.

Onoue, T., Michalík, J., Shirozu, H., Yamashita, M., Yamashita, K., Kusaka, S. & Soda, K. 2022: Extreme continental weathering in the northwestern Tethys during the end-Triassic mass extinction. — *Palaeogeography, Palaeoclimatology, Palaeoecology* **594,** 110934.

Pálfy, J. & Dosztály, L. 2000: A new marine Triassic-Jurassic boundary section in Hungary. — *GeoResearch Forum* **6,** 173-179.

Pálfy, J., Mortensen, J. K., Carter, E. S., Smith, P. L., Friedman, R. M. & Tipper, H. W. 2000: Timing the end-Triassic mass extinction: First on land, then in the sea? — *Geology* **28/1,** 39-42.

Pálfy, J., Demény, A., Haas, J., Hetényi, M., Orchard, M. J. & Veto, I. 2001: Carbon isotope anomaly and other geochemical changes at the Triassic-Jurassic boundary from a marine section in Hungary. — *Geology* **29/11,** 1047-1050.

Pálfy, J., Demény, A., Haas, J., Carter, E. S., Görög, Á., Halász, D., Oravecz-Scheffer, A., Hetényi, M., Márton, E. & Orchard, M. J. 2007: Triassic–Jurassic boundary events inferred from integrated stratigraphy of the Csővár section, Hungary. — *Palaeogeography, Palaeoclimatology, Palaeoecology* **244/1-4,** 11-33.

Palmer, M. & Edmond, J. 1989: The strontium isotope budget of the modern ocean. — *Earth and Planetary Science Letters* **92/1,** 11-26.

Paris, G., Donnadieu, Y., Beaumont, V., Fluteau, F. & Goddéris, Y. 2012: Modeling the consequences on late Triassic environment of intense pulse-like degassing during the Central Atlantic Magmatic Province using the GEOCLIM model. — *Climate of the Past Discussions* **8/3,** 2075-2110.

Pearce, C. R., Parkinson, I. J., Gaillardet, J., Charlier, B. L., Mokadem, F. & Burton, K. W. 2015: Reassessing the stable ($\delta^{88}/^{86}Sr$) and radiogenic ($^{87}Sr/^{86}Sr$) strontium isotopic composition of marine inputs. — *Geochimica et Cosmochimica Acta* **157,** 125-146.

Percival, L. M., Bergquist, B. A., Mather, T. A. & Sanei, H. 2021: Sedimentary mercury enrichments as a tracer of large igneous province volcanism. — *Large Igneous Provinces: A Driver of Global Environmental And Biotic Changes***,** 247-262.

Percival, L. M., Ruhl, M., Hesselbo, S. P., Jenkyns, H. C., Mather, T. A. & Whiteside, J. H. 2017: Mercury evidence for pulsed volcanism during the end-Triassic mass extinction. — *Proceedings of the National Academy of Sciences* **114/30,** 7929-7934.

Peterman, Z. E., Hedge, C. E. & Tourtelot, H. A. 1970: Isotopic composition of strontium in sea water throughout Phanerozoic time. — *Geochimica et Cosmochimica Acta* **34/1,** 105-120.

Peucker-Ehrenbrink, B. & Fiske, G. J. 2019: A continental perspective of the seawater $^{87}Sr/^{86}Sr$ record: a review. — *Chemical Geology* **510,** 140-165.

Peucker-Ehrenbrink, B. & Ravizza, G. 2020: Osmium isotope stratigraphy. — *Geologic Time Scale 2020*. Elsevier, pp. 239-257.

Ravizza, G. & Peucker-Ehrenbrink, B. 2003: Chemostratigraphic evidence of Deccan volcanism from the marine osmium isotope record. — *Science* **302/5649,** 1392-1395.

Richter, F. M. & Turekian, K. K. 1993: Simple models for the geochemical response of the ocean to climatic and tectonic forcing. — *Earth and Planetary Science Letters* **119/1-2,** 121-131.

Ruhl, M. & Kürschner, W. 2011: Multiple phases of carbon cycle disturbance from large igneous province formation at the Triassic-Jurassic transition. — *Geology* **39/5,** 431-434.

Ruhl, M., Hesselbo, S. P., Al-Suwaidi, A., Jenkyns, H., Damborenea, S. E., Manceñido, M. O., Storm, M., Mather, T. & Riccardi, A. C. 2020: On the onset of Central Atlantic Magmatic Province (CAMP) volcanism and environmental and carbon-cycle change at the Triassic–Jurassic transition (Neuquén Basin, Argentina). — *Earth-science reviews* **208,** 103229.

Saltzman, M. R. & Sedlacek, A. R. 2013: Chemostratigraphy indicates a relatively complete Late Permian to Early Triassic sequence in the western United States. — *Geology* **41/4,** 399-402.

Schaller, M. F., Wright, J. D. & Kent, D. V. 2011: Atmospheric p CO2 perturbations associated with the Central Atlantic Magmatic Province. — *Science* **331/6023,** 1404-1409.

Schaller, M. F., Wright, J. D., Kent, D. V. & Olsen, P. E. 2012: Rapid emplacement of the Central Atlantic Magmatic Province as a net sink for CO_2. — *Earth and Planetary Science Letters* **323,** 27-39.

Schoene, B., Guex, J., Bartolini, A., Schaltegger, U. & Blackburn, T. J. 2010: Correlating the end-Triassic mass extinction and flood basalt volcanism at the 100 ka level. — *Geology* **38/5,** 387-390.

Sepkoski, J. J. 1996: Patterns of Phanerozoic extinction: a perspective from global data bases. — *Global Events and Event Stratigraphy in the Phanerozoic: Results of the International Interdisciplinary Cooperation in the IGCP-Project 216 "Global Biological Events in Earth History"*. Springer, pp. 35-51.

Sepkoski, J. J., Silver, L. & Schultz, P. 1982: Mass extinctions in the Phanerozoic oceans: a review. — *Geological implications of impacts of large asteroids and comets on the earth* **190,** 283-9.

Shen, J., Yin, R., Algeo, T. J., Svensen, H. H. & Schoepfer, S. D. 2022a: Mercury evidence for combustion of organic-rich sediments during the end-Triassic crisis. — *Nature Communications* **13/1,** 1307.

Shen, J., Yin, R., Zhang, S., Algeo, T. J., Bottjer, D. J., Yu, J., Xu, G., Penman, D., Wang, Y. & Li, L. 2022b: Intensified continental chemical weathering and carbon-cycle

perturbations linked to volcanism during the Triassic–Jurassic transition. — *Nature Communications* **13/1,** 299.

Smalley, P., Higgins, A., Howarth, R., Nicholson, H., Jones, C., Swinburne, N. & Bessa, J. 1994: Seawater Sr isotope variations through time: a procedure for constructing a reference curve to date and correlate marine sedimentary rocks. — *Geology* **22/5,** 431-434.

Somlyay, A., Palcsu, L., Kiss, G. I., Clarkson, M. O., Kovács, E. B., Vallner, Z., Zajzon, N. & Pálfy, J. 2023: Uranium isotope evidence for extensive seafloor anoxia after the end-Triassic mass extinction. — *Earth and Planetary Science Letters* **614,** 118190.

Song, H., Wignall, P. B., Tong, J., Song, H., Chen, J., Chu, D., Tian, L., Luo, M., Zong, K. & Chen, Y. 2015: Integrated Sr isotope variations and global environmental changes through the Late Permian to early Late Triassic. — *Earth and Planetary Science Letters* **424,** 140-147.

Steuber, T. & Veizer, J. 2002: Phanerozoic record of plate tectonic control of seawater chemistry and carbonate sedimentation. — *Geology* **30/12,** 1123-1126.

Tackett, L. S., Kaufman, A. J., Corsetti, F. A. & Bottjer, D. J. 2014: Strontium isotope stratigraphy of the G abbs F ormation (N evada): implications for global N orian–R haetian correlations and faunal turnover. — *Lethaia* **47/4,** 500-511.

Tanner, L., Lucas, S. & Chapman, M. 2004: Assessing the record and causes of Late Triassic extinctions. — *Earth-Science Reviews* **65/1-2,** 103-139.

Tejada, M. L. G., Suzuki, K., Kuroda, J., Coccioni, R., Mahoney, J. J., Ohkouchi, N., Sakamoto, T. & Tatsumi, Y. 2009: Ontong Java Plateau eruption as a trigger for the early Aptian oceanic anoxic event. — *Geology* **37/9,** 855-858.

Thibodeau, A. M., Ritterbush, K., Yager, J. A., West, A. J., Ibarra, Y., Bottjer, D. J., Berelson, W. M., Bergquist, B. A. & Corsetti, F. A. 2016: Mercury anomalies and the timing of biotic recovery following the end-Triassic mass extinction. — *Nature Communications* **7/1,** 11147.

Ullmann, C. V. & Korte, C. 2015: Diagenetic alteration in low-Mg calcite from macrofossils: a review. — *Geological Quarterly* **59/1,** 3-20, doi: 10.7306/gq. 1217.

Vallner, Z., Kovács, E. B., Haas, J., Móricz, F., Ruhl, M., Zajzon, N. & Pálfy, J. 2023: Preservation of orbital forcing in intraplatform carbonates and an astronomical time frame for a multiproxy record of end-Triassic global change from a western Tethyan section (Csővár, Hungary). — *Palaeogeography, Palaeoclimatology, Palaeoecology***,** 111493.

Van De Schootbrugge, B., Quan, T., Lindström, S., Püttmann, W., Heunisch, C., Pross, J., Fiebig, J., Petschick, R., Röhling, H.-G. & Richoz, S. 2009: Floral changes across the Triassic/Jurassic boundary linked to flood basalt volcanism. — *Nature Geoscience* **2/8,** 589-594.

Van De Schootbrugge, B., Van Der Weijst, C., Hollaar, T., Vecoli, M., Strother, P., Kuhlmann, N., Thein, J., Visscher, H., Van Konijnenburg-Van Cittert, H. & Schobben, M. 2020: Catastrophic soil loss associated with end-Triassic deforestation. — *Earth-Science Reviews* **210,** 103332.

Vďačný, M. & Michalík, J. 2023: Provenance of quartz debris in the Central Western Carpathians at the end of the Triassic, as indicated by cathodoluminescence colours. — *Acta Geologica Polonica***,** 103-114-103-114.

Veizer, J. & Compston, W. 1974: $^{87}Sr/^{86}Sr$ composition of seawater during the Phanerozoic. — *Geochimica et Cosmochimica Acta* **38/9,** 1461-1484.

Veizer, J., Ala, D., Azmy, K., Bruckschen, P., Buhl, D., Bruhn, F., Carden, G. A., Diener, A., Ebneth, S. & Godderis, Y. 1999: $^{87}Sr/^{86}Sr$, $\delta^{13}C$ and $\delta^{18}O$ evolution of Phanerozoic seawater. — *Chemical geology* **161/1-3,** 59-88.

Ward, P., Haggart, J., Carter, E., Wilbur, D., Tipper, H. & Evans, T. 2001: Sudden productivity collapse associated with the Triassic-Jurassic boundary mass extinction. — *Science* **292/5519,** 1148-1151.

Whiteside, J. H., Olsen, P. E., Eglinton, T., Brookfield, M. E. & Sambrotto, R. N. 2010: Compound-specific carbon isotopes from Earth's largest flood basalt eruptions directly linked to the end-Triassic mass extinction. — *Proceedings of the National Academy of Sciences* **107/15,** 6721-6725.

Wierzbowski, H. 2015: Strontium isotope composition of sedimentary rocks and its application to chemostratigraphy and palaeoenvironmental reconstructions. — *Annales Universitatis Mariae Curie-Sklodowska, sectio AAA–Physica* **68,** 23.

Wignall, P. B. & Atkinson, J. W. 2020: A two-phase end-Triassic mass extinction. — *Earth-Science Reviews* **208,** 103282.

Wotzlaw, J.-F., Guex, J., Bartolini, A., Gallet, Y., Krystyn, L., Mcroberts, C. A., Taylor, D., Schoene, B. & Schaltegger, U. 2014: Towards accurate numerical calibration of the Late Triassic: High-precision U-Pb geochronology constraints on the duration of the Rhaetian. — *Geology* **42/7,** 571-574.

Yager, J. A., West, A. J., Thibodeau, A. M., Corsetti, F. A., Rigo, M., Berelson, W. M., Bottjer, D. J., Greene, S. E., Ibarra, Y. & Jadoul, F. 2021: Mercury contents and isotope ratios from diverse depositional environments across the Triassic–Jurassic Boundary: Towards a more robust mercury proxy for large igneous province magmatism. — *Earth-Science Reviews* **223,** 103775.

Yobo, L. N., Brandon, A. D., Holmden, C., Lau, K. V. & Eldrett, J. 2021: Changing inputs of continental and submarine weathering sources of Sr to the oceans during OAE 2. — *Geochimica et cosmochimica acta* **303,** 205-222.

Zaffani, M., Jadoul, F. & Rigo, M. 2018: A new Rhaetian δ13Corg record: carbon cycle disturbances, volcanism, End-Triassic mass Extinction (ETE). — *Earth-Science Reviews* **178,** 92-104.

Zhang, F., Lenton, T. M., Del Rey, Á., Romaniello, S. J., Chen, X., Planavsky, N. J., Clarkson, M. O., Dahl, T. W., Lau, K. V. & Wang, W. 2020: Uranium isotopes in marine carbonates as a global ocean paleoredox proxy: a critical review. — *Geochimica et Cosmochimica Acta* **287,** 27-49.

Zhou, Y., Pogge Von Strandmann, P. A., Zhu, M., Ling, H., Manning, C., Li, D., He, T. & Shields, G. A. 2020: Reconstructing Tonian seawater $^{87}Sr/^{86}Sr$ using calcite microspar. — *Geology* **48/5,** 462-467.

11 Appendix

Table A1. Elemental concentrations for the Csővár section.

Sample	Height (m)	Rock Li (ppm)	Rock Sr (ppm)	Rock Ca (ppm)	Rock Mg (ppm)	Rock Al (ppm)	Rock Rb (ppm)	Rock Mn (ppm)	Rock Ti (ppm)	Rock Pb (ppm)
JK0.7	0.7	0.13	996	228956	1415	22.7	0.35	92.12		
JK1.2mic	1.2	0.26	1124	266899	1725	75.86	0.44	48.8		
JK2.7	2.7	0.43	1694	262633	2887	18.4	0.1	22.5	1.6	0
JK3.6	3.6	0.39	4077	732150	4542	10	0.4	60	0	0
JK3.8	3.8	0.14	1315	253858	1571	9.23	0.27	56		
JK4.4	4.4	0.31	1086	258712	2462	0.9	0.1	36.6	0	0
JK5.2	5.2	0.31	1339	297940	2324	-0.01	0.11	40.26		
JK6.8A	6.8	0.29	996	240060	1749	43.07	0.57	30.98		
JK6.8B	6.8	0.3	1042	270034	2138	30.18	0.38	36.89		
JK7.2	7.2	0.25	1715	266251	1937	22.28	0.26	46.97		
JK8.8	8.8	0.23	1654	249679	2050	12.1	0.1	26	0	0
JK9.2MIC	9.2	0.21	1479	265335	1739	5	0.1	44.7	0	0
JK9.2GRAIN	9.2	0.28	1523	281849	1754	5.7	0.1	45.8	0	0
JK9.8	9.8	0.28	1907	283264	2278	0.66	0.09	40.04		
JK10.2	10.2	0.17	1588	264381	1453	10.5	0.2	74.7	0	0
JK10.6	10.6	0.14	1463	293351	1536	2.4	0.2	134.9	0	0
JK11	11	0.67	3848	935948	9045	10.6	0.1	64.9	0.4	0
JK12.4	12.4	0.35	1766	227770	2138	134	0.1	90.4	0	0.6
JK13	13	0.3	1977	256423	2460	70.9	0.2	97.7	0.3	0
JK13.4	13.4	0.29	1905	294377	2194	4.3	0.3	98.2	0	0.1
JK13.4DUP	13.4	0.32	1855	292525	2203	6.4	0.3	100	0.2	0
JK13.8	13.8	0.31	1613	270333	2161	7	0.2	93.8	0.3	0
JK16.9	16.9	0.3	1800	254303	1878	5.9	0.1	65.8	0	0
JK16.9DUP	16.9	0.7	4646	626004	4907	14.7	0.2	126.9	0.6	0
JK17.6	17.6	0.95	6892	1095892	8431	18.7	0.3	88.7	0.4	0.1
JK18m	18	0.15	991	286189	981	38.83	0.13	30.8		
JK18	18	0.33	2970	889935	3812	15.3	0.2	70.4	0	0
JK18.55	18.55	0.17	1047	263123	1389	10.5	0.1	44.5	0.2	0.1
JK18.8	18.8	0.07	620	294655	734	23.32	0.12	73.05		
JK19m	19	0.1	988	275427	916	12.43	0.17	130.98		
JK19.2	19.2	0.16	1548	252791	1281	9.1	0.1	61.5	0.2	0
JK19.4	19.4	0.07	719	244605	921	6.9	0.1	25.7	0.2	0
JK19.6	19.6	0.07	508	257123	682	16.3	0.2	157.3	0.6	0.1
JK19.8	19.8	0.02	149	280363	668	5.9	0.1	212.1	0.1	0
JK19.8vein	19.8	0.02	176	311862	1688	132.97	0.52	599.85		
JK20	20	0.09	738	238289	825	2.6	0.2	111.1	0	0
JK20.2	20.2	0.05	205	246823	771	6.5	0.2	253.7	0.1	0
JK20.4	20.4	0.1	539	254314	882	89.1	0.2	254.4	0.1	0.1
JK20.4DUP	20.4	0.1	552	258868	880	17.4	0.2	258.9	0.1	0
JK20.8	20.8	0.24	1644	291288	1379	7.24	0.26	69.48		
JK21m	21	0.26	1538	279699	1465	64.72	0.33	66.96		
JK21.2	21.2	0.17	1234	253308	1268	29	0.2	49.6	0.1	0.1
JK21.4	21.4	0.16	1512	267095	1256	15.87	0.21	72.29		
JK21.5	21.5	0.23	1756	289165	1460	57.42	0.24	52.06		
JK21.5vein	21.5	0.01	1507	302601	1017	14.31	0.01	44.21		
JK21.65	21.65	0.15	874	299371	949	22.55	0.15	56.57		
JK21.8A	21.8	0.22	1657	285644	1462	17.43	0.26	56.41		

JK21.8B	21.8	0.24	1848	304957	1551	25.36	0.33	62.53		
JK22m	22	0.12	1183	259054	956	35.85	0.22	58.43		
JK22.6	22.6	0.05	547	286832	838	20.35	0.36	192.01		
JK22.8	22.8	0.1	1518	298158	1306	14.98	0.28	89.05		
JK23.55	23.55	0.47	2618	542395	3131	28.1	0.5	129	0.5	0.2
JK23.7	23.7									
JK24.2	24.2	0.28	1937	299104	1854	15.26	0.25	204.02		
JK24.5	24.5	0.05	306	77062	328	33.26	0.13	20.79		
JK25.2	25.2	0.23	1314	250967	1433	11	0.2	51.9	0.3	0
JK25.7	25.7	0.19	1198	245162	1374	10.4	0.1	34.5	0.4	0
JK26.2	26.2	0.26	1337	268699	1461	84.99	0.38	80.11		
JK28	28	0.16	1118	254197	1338	8.6	0.1	43.7	0.2	0
JK31	31	0.27	980	254971	1616	18.7	0.3	127.2	0	0
JK31.4	31.4	0.19	250	258178	845	20.68	0.2	250.21		
JK32m	32	0.41	1311	319024	2002	182.61	0.98	99.96		
JK32	32	0.24	1245	258976	1810	14.9	0.3	86.2	0	0
JK34.5	34.5	0.23	1041	253281	1823	7.7	0	41	0.1	0
JK34.5DUP	34.5	0.26	1036	252085	1808	3.8	0	41	0	0
JK35.6	35.6	0.21	1153	255578	2037	9.5	0.2	58.3	0.3	0
JK40.5	40.5	0.2	1281	254343	1873	10.28	0.14	89.24		
JK40.5	40.5	0.2	1190	253821	1964	7.6	0.1	97.8	0.2	0
JK43	43	0.37	1425	257932	2959	19.4	0.1	74.9	0.1	0.2
JK43.5	43.5	0.36	1470	295026	3316	37.6	0.26	71.6		

Table A2. Elemental concentrations in molarity for the Csővár section

Sample	Height (m)	Li (umol)	Sr (mmol)	Ca (mol)	Mg (mol)	Al (mmol)	Rb (mmol)	Mn (mmol)
JK0.7	0.7	19.2	11.4	5.7	0.1	0.8	0	1.7
JK1.2mic	1.2	36.9	12.8	6.7	0.1	2.8	0	0.9
JK2.7	2.7	62.5	19.3	6.6	0.1	0.7	0	0.4
JK3.6	3.6	56.2	46.5	18.3	0.2	0.4	0	1.1
JK3.8	3.8	19.5	15	6.3	0.1	0.3	0	1
JK4.4	4.4	44.7	12.4	6.5	0.1	0	0	0.7
JK5.2	5.2	44.6	15.3	7.4	0.1	0	0	0.7
JK6.8A	6.8	42	11.4	6	0.1	1.6	0	0.6
JK6.8B	6.8	43.4	11.9	6.8	0.1	1.1	0	0.7
JK7.2	7.2	35.4	19.6	6.7	0.1	0.8	0	0.9
JK8.8	8.8	32.5	18.9	6.2	0.1	0.4	0	0.5
JK9.2MIC	9.2	30.6	16.9	6.6	0.1	0.2	0	0.8
JK9.2GRAIN	9.2	40.2	17.4	7	0.1	0.2	0	0.8
JK9.8	9.8	41	21.8	7.1	0.1	0	0	0.7
JK10.2	10.2	25	18.1	6.6	0.1	0.4	0	1.4
JK10.6	10.6	20.1	16.7	7.3	0.1	0.1	0	2.5
JK11	11	96.7	43.9	23.4	0.4	0.4	0	1.2
JK12.4	12.4	50	20.2	5.7	0.1	5	0	1.6
JK13	13	43.8	22.6	6.4	0.1	2.6	0	1.8
JK13.4	13.4	42	21.7	7.4	0.1	0.2	0	1.8
JK13.4DUP	13.4	45.6	21.2	7.3	0.1	0.2	0	1.8
JK13.8	13.8	45	18.4	6.8	0.1	0.3	0	1.7
JK16.9	16.9	43.1	20.5	6.4	0.1	0.2	0	1.2
JK16.9DUP	16.9	101.2	53	15.7	0.2	0.5	0	2.3
JK17.6	17.6	136.5	78.7	27.4	0.3	0.7	0	1.6
JK18m	18	21.5	11.3	7.2	0	1.4	0	0.6
JK18	18	47.9	33.9	22.2	0.2	0.6	0	1.3
JK18.55	18.55	24.8	12	6.6	0.1	0.4	0	0.8
JK18.8	18.8	9.7	7.1	7.4	0	0.9	0	1.3
JK19m	19	13.9	11.3	6.9	0	0.5	0	2.4
JK19.2	19.2	23.5	17.7	6.3	0.1	0.3	0	1.1
JK19.4	19.4	10.1	8.2	6.1	0	0.3	0	0.5
JK19.6	19.6	10	5.8	6.4	0	0.6	0	2.9
JK19.8	19.8	2.9	1.7	7	0	0.2	0	3.9
JK19.8vein	19.8	3.6	2	7.8	0.1	4.9	0	10.9
JK20	20	12.5	8.4	6	0	0.1	0	2
JK20.2	20.2	7.1	2.3	6.2	0	0.2	0	4.6
JK20.4	20.4	14.4	6.1	6.4	0	3.3	0	4.6
JK20.4DUP	20.4	13.7	6.3	6.5	0	0.6	0	4.7
JK20.8	20.8	34.7	18.8	7.3	0.1	0.3	0	1.3
JK21m	21	37.8	17.6	7	0.1	2.4	0	1.2
JK21.2	21.2	24.2	14.1	6.3	0.1	1.1	0	0.9
JK21.4	21.4	23.4	17.3	6.7	0.1	0.6	0	1.3
JK21.5	21.5	33.7	20	7.2	0.1	2.1	0	0.9
JK21.5vein	21.5	2.2	17.2	7.6	0	0.5	0	0.8
JK21.65	21.65	21.4	10	7.5	0	0.8	0	1
JK21.8A	21.8	31.4	18.9	7.1	0.1	0.6	0	1
JK21.8B	21.8	35.2	21.1	7.6	0.1	0.9	0	1.1

JK22m	22	17.3	13.5	6.5	0	1.3	0	1.1
JK22.6	22.6	7.4	6.2	7.2	0	0.8	0	3.5
JK22.8	22.8	15.1	17.3	7.5	0.1	0.6	0	1.6
JK23.55	23.55	68.3	29.9	13.6	0.1	1	0	2.3
JK23.7	23.7							
JK24.2	24.2	39.8	22.1	7.5	0.1	0.6	0	3.7
JK24.5	24.5	7.1	3.5	1.9	0	1.2	0	0.4
JK25.2	25.2	33	15	6.3	0.1	0.4	0	0.9
JK25.7	25.7	27.2	13.7	6.1	0.1	0.4	0	0.6
JK26.2	26.2	37.4	15.3	6.7	0.1	3.2	0	1.5
JK28	28	23.3	12.8	6.4	0.1	0.3	0	0.8
JK31	31	38.2	11.2	6.4	0.1	0.7	0	2.3
JK31.4	31.4	26.9	2.8	6.5	0	0.8	0	4.6
JK32m	32	58.4	15	8	0.1	6.8	0	1.8
JK32	32	34.7	14.2	6.5	0.1	0.6	0	1.6
JK34.5	34.5	33.2	11.9	6.3	0.1	0.3	0	0.7
JK34.5DUP	34.5	37.9	11.8	6.3	0.1	0.1	0	0.7
JK35.6	35.6	30.5	13.2	6.4	0.1	0.4	0	1.1
JK40.5	40.5	29	14.6	6.4	0.1	0.4	0	1.6
JK40.5	40.5	29.2	13.6	6.3	0.1	0.3	0	1.8
JK43	43	53.2	16.3	6.4	0.1	0.7	0	1.4
JK43.5	43.5	51.6	16.8	7.4	0.1	1.4	0	1.3

Table A3. Elemental ratios for the Csővár section

Sample	Height (m)	Li/Ca umol/mol	Al/Ca mmol/mol	Sr/Ca mmol/mol	Mn/Ca mmol/mol	Mn/Sr ppm/ppm	Mg/Ca ppm/ppm	Rb/Sr ppm/ppm
JK0.7	0.7	3.3	0.15	1.99	0.29	0.09252	0.00618	0.00035
JK1.2mic	1.2	5.5	0.42	1.92	0.13	0.04342	0.00646	0.00039
JK2.7	2.7	9.5	0.1	2.94	0.06	0.01328	0.01099	0.00006
JK3.6	3.6	3.1	0.02	2.54	0.06	0.01472	0.00620	0.00010
JK3.8	3.8	3.1	0.05	2.36	0.16	0.04259	0.00619	0.00021
JK4.4	4.4	6.9	0.01	1.92	0.1	0.03369	0.00951	0.00009
JK5.2	5.2	6	0	2.05	0.1	0.03007	0.00780	0.00008
JK6.8A	6.8	7	0.27	1.89	0.09	0.03111	0.00729	0.00057
JK6.8B	6.8	6.4	0.17	1.76	0.1	0.03540	0.00792	0.00036
JK7.2	7.2	5.3	0.12	2.94	0.13	0.02739	0.00727	0.00015
JK8.8	8.8	5.2	0.07	3.02	0.08	0.01572	0.00821	0.00006
JK9.2MIC	9.2	4.6	0.03	2.54	0.12	0.03023	0.00655	0.00007
JK9.2GRAIN	9.2	5.7	0.03	2.47	0.12	0.03007	0.00622	0.00007
JK9.8	9.8	5.8	0	3.07	0.1	0.02100	0.00804	0.00005
JK10.2	10.2	3.8	0.06	2.74	0.21	0.04704	0.00550	0.00013
JK10.6	10.6	2.7	0.01	2.28	0.33	0.09223	0.00523	0.00014
JK11	11	4.1	0.02	1.88	0.05	0.01687	0.00966	0.00003
JK12.4	12.4	8.8	0.87	3.54	0.29	0.05118	0.00939	0.00006
JK13	13	6.8	0.41	3.52	0.28	0.04942	0.00959	0.00010
JK13.4	13.4	5.7	0.02	2.95	0.24	0.05154	0.00745	0.00016
JK13.4DUP	13.4	6.2	0.03	2.9	0.25	0.05391	0.00753	0.00016
JK13.8	13.8	6.7	0.04	2.72	0.25	0.05814	0.00800	0.00012
JK16.9	16.9	6.8	0.03	3.23	0.19	0.03655	0.00739	0.00006
JK16.9DUP	16.9	6.5	0.03	3.39	0.15	0.02731	0.00784	0.00004
JK17.6	17.6	5	0.03	2.87	0.06	0.01287	0.00769	0.00004
JK18m	18	3	0.2	1.58	0.08	0.03109	0.00343	0.00013
JK18	18	2.2	0.03	1.52	0.06	0.02371	0.00428	0.00007
JK18.55	18.55	3.8	0.06	1.82	0.12	0.04249	0.00528	0.00010
JK18.8	18.8	1.3	0.12	0.96	0.18	0.11785	0.00249	0.00019
JK19m	19	2	0.07	1.64	0.35	0.13251	0.00333	0.00017
JK19.2	19.2	3.7	0.05	2.8	0.18	0.03973	0.00507	0.00006
JK19.4	19.4	1.6	0.04	1.34	0.08	0.03576	0.00377	0.00014
JK19.6	19.6	1.6	0.09	0.9	0.45	0.30989	0.00265	0.00039
JK19.8	19.8	0.4	0.03	0.24	0.55	1.42254	0.00238	0.00067
JK19.8vein	19.8	0.5	0.63	0.26	1.4	3.41425	0.00541	0.00296
JK20	20	2.1	0.02	1.41	0.34	0.15058	0.00346	0.00027
JK20.2	20.2	1.1	0.04	0.38	0.75	1.23696	0.00312	0.00098
JK20.4	20.4	2.3	0.52	0.97	0.73	0.47216	0.00347	0.00037
JK20.4DUP	20.4	2.1	0.1	0.97	0.73	0.46945	0.00340	0.00036
JK20.8	20.8	4.8	0.04	2.58	0.17	0.04226	0.00473	0.00016
JK21m	21	5.4	0.34	2.51	0.17	0.04353	0.00524	0.00021
JK21.2	21.2	3.8	0.17	2.22	0.14	0.04021	0.00501	0.00016
JK21.4	21.4	3.5	0.09	2.58	0.2	0.04781	0.00470	0.00014
JK21.5	21.5	4.7	0.29	2.77	0.13	0.02964	0.00505	0.00014
JK21.5vein	21.5	0.3	0.07	2.27	0.11	0.02933	0.00336	0.00001
JK21.65	21.65	2.9	0.11	1.33	0.14	0.06472	0.00317	0.00017
JK21.8A	21.8	4.4	0.09	2.65	0.14	0.03404	0.00512	0.00016
JK21.8B	21.8	4.6	0.12	2.77	0.15	0.03384	0.00509	0.00018

JK22m	22	2.7	0.21	2.08	0.16	0.04941	0.00369	0.00019
JK22.6	22.6	1	0.11	0.87	0.49	0.35071	0.00292	0.00066
JK22.8	22.8	2	0.07	2.32	0.22	0.05865	0.00438	0.00018
JK23.55	23.55	5	0.08	2.2	0.17	0.04927	0.00577	0.00019
JK23.7	23.7							
JK24.2	24.2	5.3	0.08	2.96	0.5	0.10532	0.00620	0.00013
JK24.5	24.5	3.7	0.64	1.81	0.2	0.06799	0.00425	0.00043
JK25.2	25.2	5.3	0.07	2.39	0.15	0.03949	0.00571	0.00015
JK25.7	25.7	4.4	0.06	2.23	0.1	0.02881	0.00560	0.00008
JK26.2	26.2	5.6	0.47	2.27	0.22	0.05991	0.00544	0.00028
JK28	28	3.7	0.05	2.01	0.13	0.03910	0.00526	0.00009
JK31	31	6	0.11	1.75	0.36	0.12986	0.00634	0.00031
JK31.4	31.4	4.2	0.12	0.44	0.71	1.00256	0.00327	0.00080
JK32m	32	7.3	0.85	1.88	0.23	0.07623	0.00627	0.00075
JK32	32	5.4	0.09	2.19	0.24	0.06925	0.00699	0.00024
JK34.5	34.5	5.2	0.04	1.88	0.12	0.03940	0.00720	0.00000
JK34.5DUP	34.5	6	0.02	1.88	0.12	0.03958	0.00717	0.00000
JK35.6	35.6	4.8	0.06	2.06	0.17	0.05057	0.00797	0.00017
JK40.5	40.5	4.6	0.06	2.3	0.26	0.06967	0.00737	0.00011
JK40.5	40.5	4.6	0.04	2.14	0.28	0.08221	0.00774	0.00008
JK43	43	8.2	0.11	2.52	0.21	0.05256	0.01147	0.00007
JK43.5	43.5	7	0.19	2.27	0.18	0.04872	0.01124	0.00018

Table A4. Stable isotope-. and $^{87}Sr/^{86}Sr$ isotope ratios for the Csővár section

Sample	Height (m)	$\delta^{13}C$	$\delta^{18}O$	$^{87}Sr/^{86}Sr$	±1σ
JK0.7	0.7			0.707727	0.000015
JK1.2mic	1.2			0.707713	0.000015
JK2.7	2.7	2.41	-0.62	0.707700	0.000030
JK3.6	3.6	1.42	-1.96	0.707676	0.000016
JK3.8	3.8			0.707703	0.000015
JK4.4	4.4	1.87	-1.08	0.707702	0.000017
JK5.2	5.2	1.3	-0.97	0.707698	0.000015
JK6.8A	6.8	1.64	-1.81	0.707704	0.000015
JK6.8B	6.8			0.707692	0.000016
JK7.2	7.2			0.707712	0.000017
JK8.8	8.8	1.74	-1.73	0.707657	0.000015
JK9.2MIC	9.2	0.63	-2.12	0.707647	0.000016
JK9.2GRAIN	9.2	0.9	-1.52	0.707687	0.000015
JK9.8	9.8	1.87	-1.54	0.707687	0.000017
JK10.2	10.2			0.707728	0.000018
JK10.6	10.6			0.707669	0.000016
JK11	11	-0.15	-1.77	0.707712	0.000015
JK12.4	12.4			0.707662	0.000015
JK13	13			0.707653	0.000016
JK13.4	13.4			0.707671	0.000016
JK13.4DUP	13.4			0.707663	0.000016
JK13.8	13.8			0.707656	0.000016
JK16.9	16.9	3.17	-3.06	0.707692	0.000015
JK16.9DUP	16.9			0.707659	0.000015
JK17.6	17.6	1.84	-1.8	0.707694	0.000016
JK18m	18	-3.51	-3.25	0.707686	0.000016
JK18	18			0.708952	0.000015
JK18.55	18.55	-0.86	-2.49	0.707663	0.000015
JK18.8	18.8	-3.6	-5.43	0.707715	0.000016
JK19m	19			0.707694	0.000016
JK19.2	19.2	0.36	-2.59	0.707657	0.000016
JK19.4	19.4			0.707651	0.000015
JK19.6	19.6			0.707736	0.000016
JK19.8	19.8			0.708086	0.000015
JK19.8vein	19.8				
JK20	20			0.707711	0.000015
JK20.2	20.2			0.707987	0.000015
JK20.4	20.4			0.707810	0.000030
JK20.4DUP	20.4			0.707807	0.000015
JK20.8	20.8	1.97	-1.73	0.707659	0.000019
JK21m	21	2.39	-1.89	0.707685	0.000028
JK21.2	21.2	-0.26	-3.13	0.707713	0.000015
JK21.4	21.4	1.62	-2.17	0.707684	0.000030
JK21.5	21.5			0.707655	0.000015
JK21.5vein	21.5			0.707683	0.000016
JK21.65	21.65	-3.17	-3.59	0.707682	0.000015
JK21.8A	21.8	1.85	-1.81	0.707699	0.000015
JK21.8B	21.8	1.85	-1.81	0.707679	0.000016

JK22m	22	-0.76	-2.97	0.707683	0.000015
JK22.6	22.6			0.707752	0.000016
JK22.8	22.8	1.08	-2.22	0.707675	0.000016
JK23.55	23.55	1.5	-2.75	0.707669	0.000015
JK23.7	23.7	1.34	-1.93	0.707690	0.000015
JK24.2	24.2			0.707679	0.000015
JK24.5	24.5			0.707667	0.000015
JK25.2	25.2			0.707673	0.000015
JK25.7	25.7	-0.1	-2.62	0.707678	0.000015
JK26.2	26.2			0.707710	0.000016
JK28	28	0.25	-2.45	0.707693	0.000016
JK31	31			0.707693	0.000021
JK31.4	31.4			0.707952	0.000033
JK32m	32			0.707693	0.000021
JK32	32			0.707741	0.000032
JK34.5	34.5	2.99	-2.48	0.707702	0.000021
JK34.5DUP	34.5			0.707689	0.000017
JK35.6	35.6			0.707687	0.000021
JK40.5	40.5			0.707625	0.000015
JK40.5	40.5			0.707691	0.000021
JK43	43	3.32	-2.25	0.707708	0.000015
JK43.5	43.5	3.06	-1.52	0.707685	0.000015

R script of Scenario 3 with hydrothermal perturbation set to 1.5x (Fig. 26)

```
# Sr box model for the 'Csővár' TJB after the model of Yobo et al. 2021
# Scenario with hydrothermal flux 2x in response to CAMP

library(deSolve)

#### MODEL equations ####
{Sr.box = function(t.y.p){
  with(as.list(c(p.y)).{

    #Perturbations
    F.hT = force.hT(t) # forcing to the hydrothermal flux
    F.wx = force.wx(t) # forcing to the continental flux

    # Calculate mass fluxes
    FrivSr = p['FrivSr.i']*F.wx # perturbed continental flux
    FhydSr = p['FhydSr.i']*F.hT # perturbed hydrothermal flux
    FbcarbSr = p['k.carb']*y['MSr'] # new carbonate burial flux

    # Differential equations
    dMSr = FrivSr + FhydSr  + p['FdiagSr'] - FbcarbSr #+ p['FpwSr']
    dRSr = (FrivSr*(p['RSrriv'] - y['RSr'])
            + FhydSr*(p['RSrhyd'] - y['RSr'])
            + p['FdiagSr']*(p['RSrdiag'] - y['RSr']))/y['MSr']

    res = c(dMSr. dRSr)
    list(res)
  })
}

#### MODEL TIME ####
duration <- 3e6 #3 million years
dt <- 5000 #5000 year time steps
t<- seq(0. duration. dt)

#### PERTURBATIONS ####
# Hydrothermal Flux
t.exc.start = 0e6 #start of perturbation 1
t.exc.end = 1e6 #end of perturbation 1
t.exc.pt2.start = 1e6 #start of perturbation 2
t.exc.pt2.end = 1.3e6 #end of perturbation 2
t.exc.pt3.start = 1.3e6 #start of perturbation 3
t.exc.pt3.end = 1.65e6 #end of perturbation 3
t.exc.pt4.start = 1.65e6 #start of perturbation 4
t.exc.pt4.end = 3e6 #end of perturbation 4

m = 1 #proportion that the hydrothermal flux is changed relative to ss; perturbation
1
m.2 = 1.5 #proportion that the hydrothermal flux is changed relative to ss;
perturbation 2
m.3 = 1.2 #proportion that the hydrothermal flux is changed relative to ss;
perturbation 3
m.4 = 1.2 #proportion that the hydrothermal flux is changed relative to ss;
perturbation 4

Finterp.hT = c(rep(1.(t.exc.start/dt+1)).
               rep(m.(t.exc.end - t.exc.start)/dt). #square wave for perturbation 1
               rep(1.(t.exc.pt2.start - t.exc.end)/dt).
               rep(m.2.(t.exc.pt2.end  -  t.exc.pt2.start)/dt).  #square  wave  for
perturbation 2
               rep(1.(t.exc.pt3.start - t.exc.pt2.end)/dt).
               rep(m.3.(t.exc.pt3.end  -  t.exc.pt3.start)/dt).  #square  wave  for
perturbation 3
               rep(1.(t.exc.pt4.start - t.exc.pt3.end)/dt).
```

```
               rep(m.4.(t.exc.pt4.end  -  t.exc.pt4.start)/dt).  #square  wave  for
perturbation 4
               rep(1.(duration-t.exc.pt4.end)/dt))
event = data.frame(t.Finterp.hT)
force.hT  =  approxfun(x=event[.1].y=event[.2].method="linear".rule=2)  #function  for
calculating F.hT in model

# Weathering Flux
t.exc.start = 0e6 #start of perturbation 1
t.exc.end = 1e6 #end of perturbation 1
t.exc.pt2.start = 1e6 #start of perturbation 2
t.exc.pt2.end = 1.3e6 #end of perturbation 2
t.exc.pt3.start = 1.3e6 #start of perturbation 3
t.exc.pt3.end = 1.65e6 #end of perturbation 3
t.exc.pt4.start = 1.65e6 #start of perturbation 4
t.exc.pt4.end = 3e6 #end of perturbation 4

m = 0.79 #proportion that the weathering flux is changed relative to ss; perturbation
1
m.2 = 1.35 #proportion that the weathering flux is changed relative to ss; perturbation
2
m.3 = 1.35 #proportion that the weathering flux is changed relative to ss; perturbation
2
m.4 = 1.14 #proportion that the weathering flux is changed relative to ss; perturbation
4

Finterp.wx = c(rep(1.(t.exc.start/dt+1)).
               rep(m.(t.exc.end - t.exc.start)/dt). #square wave for perturbation 1
               rep(1.(t.exc.pt2.start - t.exc.end)/dt).
               rep(m.2.(t.exc.pt2.end  -  t.exc.pt2.start)/dt).  #square  wave  for
perturbation 2
               rep(1.(t.exc.pt3.start - t.exc.pt2.end)/dt).
               rep(m.3.(t.exc.pt3.end  -  t.exc.pt3.start)/dt).  #square  wave  for
perturbation 3
               rep(1.(t.exc.pt4.start - t.exc.pt3.end)/dt).
               rep(m.4.(t.exc.pt4.end  -  t.exc.pt4.start)/dt).  #square  wave  for
perturbation 4
               rep(1.(duration-t.exc.pt4.end)/dt))
event = data.frame(t.Finterp.wx)
force.wx  =  approxfun(x=event[.1].y=event[.2].method="linear".rule=2)  #function  for
calculating F.wx in model


#### PARAMETERS ####
# Initial Sr Reservoir
MSr.i = 1.25e17 # moles; Palmer and Edmond (1989)

# Initial Fluxes. all in mol/yr unless specified otherwise
FrivSr.i = 66.1e9 # total continental flux; Peucker-Ehrenbrink and Fiske (2019)
FhydSr.i = 14.1e9 # Hydrothermal flux; from Peucker-Ehrenbrink and Fiske (2019)
FdiagSr.i = 5.5e9 # Diagenetic flux; Peucker-Ehrenbrink and Fiske (2019)
FbcarbSr.i = FrivSr.i + FhydSr.i + FdiagSr.i # calculated to reach steady state
k.carb = FbcarbSr.i/MSr.i # reaction rate for Sr removal via carbonate precipitation

# Initial Isotope Ratios
ssRSr = 0.70773 # initial seawater. adjusted for pre-TJB ss
RSrhyd = 0.7035 # from modern value; Peucker-Ehrenbrink and Fiske (2019)
RSrdiag = ssRSr # diagenetic 87/86; set to initial seawater
RSrriv = -(FhydSr.i*(RSrhyd - ssRSr) # continental sources value set to maintain
steady state
           + FdiagSr.i*(RSrdiag - ssRSr))/FrivSr.i + ssRSr

#### RUN MODEL ####
y0 = c(MSr=MSr.i. RSr=ssRSr) # pass initial conditions for ODE solver

p=c( # parameter vector
  FhydSr.i = FhydSr.i.
  FdiagSr = FdiagSr.i.
```

```
  FrivSr.i = FrivSr.i.
  k.carb = k.carb.
  RSrhyd = RSrhyd.
  RSrriv = RSrriv.
  RSrdiag = ssRSr
)

run.start = proc.time()
output = lsodes(y=y0. times=t. func=Sr.box. parms=p. rtol=1e-3)
run.end = proc.time()
elapsed.time = (run.end[3] - run.start[3])
print(elapsed.time)

output = as.data.frame(output)
names(output) = c('time'. 'MSr'. 'RSr')

}

###### PLOTS #######

# Set up the plotting parameters
par(mfrow=c(1.3). mar=c(4.4.1.1))

# Plot 1: Hydrothermal perturbation
plot(Finterp.hT. output$time/1e6. type='l'. lwd=2. las=1.
     ylab="Model time (Myr)". xlab="Hydrothermal Perturbation".
     xlim=c(0.3). ylim=c(0.max(output$time/1e6)).
     main="Hydrothermal Perturbation")
grid(lty="dotted")

# Plot 2: Riverine perturbation
plot(Finterp.wx. output$time/1e6. type='l'. lwd=2. las=1.
     ylab="Model time (Myr)". xlab="Riverine Perturbation".
     xlim=c(0.3). ylim=c(0.max(output$time/1e6)).
     main="Riverine Perturbation")
grid(lty="dotted")

# Plot 3: 87Sr/86Sr vs time
plot(output$RSr. output$time/1e6. type='l'. lwd=2. las=1.
     ylab="Model time (Myr)". xlab="87Sr/86Sr".
     xlim=c(0.70764.0.70773). ylim=c(0.max(output$time/1e6)).
     main="87Sr/86Sr vs time")
grid(lty="dotted")
```

NYILATKOZAT

Név: Heszler Bernát

ELTE Természettudományi Kar, szak: Geológus Msc

NEPTUN azonosító: M670HX

Diplomamunka címe:
High-resolution 87Sr/86Sr record from the Triassic-Jurassic boundary section at Csövár and its implications

A **diplomamunka** szerzőjeként fegyelmi felelősségem tudatában kijelentem, hogy a dolgozatom önálló szellemi alkotásom, abban a hivatkozások és idézések standard szabályait következetesen alkalmaztam, mások által írt részeket a megfelelő idézés nélkül nem használtam fel.

Budapest, 2023. 05. 30.

Heszler

a hallgató aláírása